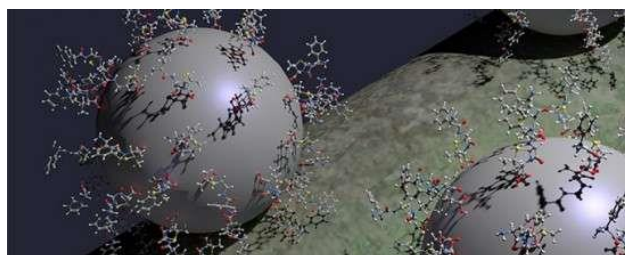


Carbohydrate coated Fluorescent Mesoporous Silica nanoparticles for Biomedical applications

By

Haritha Kirla



*A Thesis submitted in partial fulfillment
of the requirements for the degree of
Honours in Chemistry*

Under the supervision of A/Prof David J Henry



MURDOCH
UNIVERSITY
PERTH, WESTERN AUSTRALIA

Chemistry and Physics, College of Science, Health, Engineering and
Education

June 2019

Declaration

This thesis is composed of my original work, and contains no material previously published or written by another person except where due reference has been made in the text.

Haritha Kirla

Abstract

The human body and many living organisms are comprised of very complex biological system with distinct metabolism. In order to understand life activities, we need to monitor the individual chemical interactions happening in vivo. Bioimaging with naked organic dye molecules always suffers from drawbacks such as photobleaching and biocompatibility issues. Silica matrix protects the fluorophores from external environment and provides hydrophilic shell, which improves the photostability and biocompatibility of dye molecules. A nanocarrier, which is highly compatible with the target metabolic system, may be beneficial for therapeutic and diagnostic applications in living organisms. Mesoporous silica nanoparticles (MSNs) are highly biocompatible and safe for biological applications and may provide the solution.

Therefore, this project focused on the synthesis of dye-doped mesoporous silica nanoparticles, coupling them with various bioactive carbohydrate molecules, and investigation of these nanoparticles for their potential biological applications in microorganisms.

Rhodamine B, fluorescein, and methylene blue dyes were employed for doping into amine modified mesoporous silica matrix through covalent and non-covalent approaches. The results revealed that all dyes were successfully doped into the silica matrix and showed bright fluorescence. In the next stage, methylene blue encapsulated amine grafted mesoporous silica nanoparticles (MB AMSNs) were utilized for coupling with carbohydrates- glucose, maltose, ribose, and raffinose by employing N, N'-carbonyldiimidazole as a coupling agent. The chemical and physical characterization showed the successful conjugation of carbohydrates onto amine-modified silica surface.

Finally, glucose conjugated methylene blue doped mesoporous silica nanoparticles (Glu-MB MSN) were used in bioimaging and toxicity assessments. The as-synthesized nanoparticles were investigated in *E.Coli* and *B.Subtilis* bacterial samples. The characteristic results revealed bright fluorescence in bacteria like formations via confocal microscopy. Therefore, Glu-MB MSN may be useful for bioimaging purposes. SEM images showed bacterial aggregation after treatment with nanoparticles. This interaction is relatively higher in the case of *B.Subtilis*. Moreover, the bacterial cell structure appeared unaltered after incubation with the nanoparticles. This suggested that the nanoparticles were not toxic to these specific bacteria. However, more studies need to be performed to confirm these results.

Acknowledgments

I would like to express my sincere gratitude to my supervisor, Associate Professor David Henry for his guidance, continuous support, and motivation throughout my Honours study. His guidance helped me in all the time of research.

I would also like to thank Dr. Leonie Hughes for her invaluable suggestions in the final stage of my project and thesis writing.

Many thanks to Andrew Foreman, Dr. Marc Hampton, Dr. Juita, Saijel Jani, and Carolyn Tann for their technical assistance during the Honours project.

Table of content

Declaration.....	i
Abstract.....	ii
Acknowledgments.....	iii
Table of content.....	iv
List of Tables.....	vi
List of Figures.....	vi
List of Schemes.....	ix
Abbreviations.....	x
CHAPTER 1.....	1
INTRODUCTION.....	1
1.1 Significance of the work.....	1
1.2 Aim of the research.....	2
1.3 Structure of the thesis.....	3
CHAPTER 2.....	4
REVIEW OF THE LITERATURE.....	4
2.1 Background of Mesoporous silica nanoparticles (MSNs).....	5
2.2 Approaches for the synthesis of MSNs.....	7
2.3 Mechanism for the formation of MSNs.....	13
2.4 Effect of synthesis parameters on the characteristics of MSNs.....	17
2.5 MSNs in bioimaging and drug delivery.....	20
2.6 Glyconanoparticles.....	24
2.7 Conclusion.....	28
CHAPTER 3.....	29
SYNTHESIS AND CHARACTERIZATION OF DYE-DOPED MESOPOROUS SILICA NANOPARTICLES.....	29
3.1 Introduction.....	29
3.2 Experimental details.....	31
3.2.1 Details of the reagents.....	31
3.2.2 Characterization techniques.....	31

3.2.3 Experimental procedures.....	31
3.3 Results and discussion	34
3.3.1 Physiochemical characterization of MSNs and AMSNs.....	37
3.3.2 Physiochemical characterization of dye-doped AMSNs.....	42
3.3.3 Effect of synthesis parameters on MB doped AMSNs.....	48
3.4 Conclusion.....	49
CHAPTER 4.....	51
SYNTHESIS AND CHARACTERIZATION OF CARBOHYDRATE COATED FLUORESCENT MSNs	51
4.1 Introduction.....	51
4.2 Experimental details.....	52
4.2.1 Details of Reagents	52
4.2.2 Characterization techniques	52
4.2.3 Experimental procedures.....	53
4.3 Results and discussion	55
4.3.1 Physiochemical characterization of carbohydrate functionalized fluorescent MSNs.....	57
4.4 Conclusion.....	62
CHAPTER 5.....	63
INVESTIGATIONS OF GLU-MB MSN UPTAKE BY BACTERIAL CELLS.....	63
5.1 Introduction.....	63
5.2 Experimental details.....	64
5.2.1 Materials used.....	64
5.2.2 Instrumentation.....	64
5.2.3 Experimental setup	64
5.3 Results and discussion	69
5.4 Conclusion.....	73
CHAPTER 6.....	75
SUMMARY AND FUTURE OUTLOOK.....	75
6.1 Summary	75
6.2 Future outlook.....	76
BIBLIOGRAPHY.....	77

List of Tables

Table 2.1: List of structural characteristics and applications of some MSNs.....	7
Table 2.2: Carbohydrate functionalized silica nanoparticles and their respective bioapplications.	27
Table 3.1: Physical characteristics of MSNs and AMSNs synthesized at different CTAB concentrations.	39
Table 3.2: Effect of various reagent concentrations on the morphology of MB doped AMSNs .	48
Table 4.1: Elemental composition resulted from AMSN and Glu-AMSN.....	59
Table 4.2: Dye leakage studies on sugar-coated MB doped MSNs.....	61

List of Figures

Figure 2.1: Classification of porous materials (Reproduced from Malgras et al., 2015) [17]	4
Figure 2.2: Structure of mesoporous M41S materials (a) MCM-41 (2D hexagonal, space group p6mm), (b) MCM-48 (cubic, space group Ia-3d) and (c) MCM-50 (lamellar, space group p2) (Reproduced from Hoffmann et al., 2006)[25]	5
Figure 2.3: Various pore geometries (A) 2D hexagonal p6mm, (B) 3D cubic Pm3m, (C) Pm3n, (D) Im3m, (E) Fd3m, and (F) Fm3m (Reproduced from Lu et al., 2016)[19].....	6
Figure 2.4: A schematic diagram of soft templating and hard templating methods (Reproduced from Barbara et al., 2017) [61].....	10
Figure 2.5: Schematic illustration of cationic surfactant assisted selective etching (Reproduced from Fang et al., 2011) [72].....	12
Figure 2.6: Structure of CTAB surfactant	13
Figure 2.7: Formation of MCM-41 by Liquid Crystal Template (LCT) mechanism (Reproduced from Davis et al., 1994) [82].....	16
Figure 2.8: Structures of series of cationic surfactants (A) Dodecyltrimethylammonium bromide (DTAB), (B) Tetradecyltrimethylammonium bromide (TTAB), and (C) Hexadecyltrimethylammonium bromide (CTAB).	16
Figure 2.9: Graphical abstract of the effect of synthesis parameters on particle size (TEA-Triethanolamine (Base))(Reproduced from Lv et al., 2016) [94].....	18

Figure 2.10: SEM images of samples designed by the Taguchi method. The amount of TEOS added, pH, and reaction time represented respectively in each image (Reproduced from Ya0Dong et al., 2011) [97].	19
Figure 2.11: TEM images of <i>M. smegmatis</i> strain mc2 155 after incubating for 6 h with (a) Ara-FSNPs, (b) Glc-FSNPs, (c) Gal-FSNPs, (d) CD-FSNPs (Reproduced from Jayawardhana et al., 2015) [130]	25
Figure 3.1: Structure and absorption (solid line) and fluorescence (dotted line) spectra of rhodamine B, fluorescein, and methylene blue, respectively (Reproduced from google images).	30
Figure 3.2: Diagrammatic illustration of (A) covalently attached RB and (B) physically entrapped MB.	35
Figure 3.3: (A) Progress of reaction monitored by TLC after 1 hr and 2:30 hrs (under normal light and UV lamp), (B) FT-IR spectra of RB and RBS.	36
Figure 3.4: Diagrammatic representation of the co-condensation method (Reproduced from Bruhwiler et al., 2010) [157].	37
Figure 3.5: Nitrogen sorption isotherms and corresponding pore size distributions (inset) of MSNs synthesized at CTAB molar ratio of (A) 0.075, (B) 0.15, (C) 0.3, and (D) Amine modified MSN.	38
Figure 3.6: XRD diffractograms of (A) MCM-41 (reproduced from J.S.Beck et al., 1992), (B) MSN and (C) AMSNs.	40
Figure 3.7: FT-IR spectral patterns of (A) MSN and (B) AMSN.	41
Figure 3.8: Ninhydrin assay standard curve	42
Figure 3.9: SEM images of RB, fluorescein, and MB doped AMSNs, respectively.	43
Figure 3.10: X-ray diffractograms of (A) RB- AMNS, (B) Fluorescein AMSN, and (C) MB-AMSN respectively.	43
Figure 3.11: FT-IR spectra of (A) RB-AMSN, (B) Fluorescein AMSN, and (C) MB-AMSN.	44
Figure 3.12: The fluorescence of the RB, fluorescein, and MB doped AMSNs under normal light and UV lamp in solid and dispersion state respectively.	45
Figure 3.13: Solid-state UV-Vis spectra for RB, fluorescein, and MB doped AMSNs, respectively.	45
Figure 3.14: SEM of (left) covalently encapsulated RB doped AMSNs, (right) physical entrapped RB doped AMSNs.	46
Figure 3.15: (A) FT-IR spectrum and (B) XRD comparison of RB-AMSNs synthesized by covalent and non-covalent approaches.	47

Figure 3.16: Solid-state UV-Vis absorption spectra for RB AMSN doped by covalent and non-covalent approaches respectively (inset- compounds under UV lamp).....	47
Figure 3.17: SEM images obtained for MB AMSN samples at various reaction parameters (molar ratios indicated as TEOS: APTES: CTAB: NH ₄ OH: H ₂ O: EtOH).....	49
Figure 4.1: (A) Schematic illustration of the phenol-sulfuric acid method, (B) Coloured compounds obtained during colorimetric analysis.	57
Figure 4.2: Standard curve for the phenol-sulfuric acid method.....	58
Figure 4.3: Carbon calibration curve using sulfanilamide as standard.....	58
Figure 4.4: SEM images of (A) Glu-MB MSN, (B) Mal-MB MSNs, (C) Rib-MB MSN, and (D) Raffi- MB MSN.....	59
Figure 4.5: (left) N ₂ sorption isotherms of glucose conjugated MB MNS (inset – pore size distribution), (right) XRD diffractograms of (A) Glu-MB MSN, (B) Mal-MB MSN, (C) Rib-MB MSN, and (D) Raffi-MB MSN, respectively.....	60
Figure 4.6: (A) Glu-MB MSN dispersed in ethanol under normal light and UV light and (B) powdered Glu-MB MSN under normal light and UV light.....	61
Figure 4.7: (A) FT-IR spectra comparison between Glu- RB MSN and Glu- MB MSN, (B) Maltose, Ribose, and Raffinose conjugated MB MSNs, respectively.....	62
Figure 5.1: Exponential cell division (cell number increase explosively after n divisions resulted in 2 ⁿ cells) (Reproduced from Google images)	65
Figure 5.2: bacteria growth curve and mean generation time (MGT) curve respectively for (A) <i>E.Coli</i> and (B) <i>B. Subtilis</i>	66
Figure 5.3: Serial dilutions of (A) <i>E.Coli</i> and (B) <i>B.Subtilis</i>	68
Figure 5.4: Cell wall structures of a gram negative and gram positive bacteria, respectively (Reproduced from Online textbook of bacteriology).	70
Figure 5.5: (A) and (B), SEM images of pure <i>B.Subtilis</i> , <i>E.Coli</i> respectively. (C) and (D) <i>B.Subtilis</i> and <i>E.Coli</i> cultures after 3 hrs incubation with Glu-MB MSNs.....	71
Figure 5.6: Confocal microscopy images of <i>B.subtilis</i> and <i>E.coli</i> , respectively (after incubation with Glu-MB MSNs for 3 hrs).	72

List of Schemes

Scheme 2.1: Hydrolysis and condensation of tetra alkoxy silane precursor during the sol-gel process.....	8
Scheme 2.2: Acid catalyzed hydrolysis and condensation (A), Base catalyzed hydrolysis and condensation (B) (Reproduced from Danks et al., 2016)[59].....	9
Scheme 2.3: Construction of pH-Responsive HPSN–Salphdc–FA System: (A) Chemical reaction routes and (B) Drug-loaded HPSN–Salphdc–FA system for tumor therapy and bioimaging in vivo (Reproduced from Cai et al., 2015) [106]	22
Scheme 2.4: (a) Synthesis of FSNP and (b) Conjugation of arabinose on to FSNP by PFPA-Silane intermediate (Reproduced from Jayawardhana et al., 2015) [130].....	25
Scheme 3.1: Protocol for the synthesis of Rhodamine–APTES adduct (RBS)	35
Scheme 3.2: Schematic illustration of the synthesis of amine-modified MSNs (AMSN) by co-condensation method.....	37
Scheme 3.3: Formation of Ruhemann's purple by the reaction of amine-modified MSN with ninhydrin reagent (Reproduced from Hsu et al., 2013).....	41
Scheme 4.1: Schematic illustration of carbohydrate functionalization on dye-doped MSN.....	53
Scheme 4.2: General schematic illustration of CDI mediated coupling reaction between hydroxyl containing molecule and primary amine-containing molecule (Reproduced from Bioconjugate techniques., 2013) [175].	56
Scheme 5.1: MB redox reaction	73

Abbreviations

nm	Nanometer
°C	Degree centigrade
ml/min	Milliliters per minute
min	Minutes
hrs	Hours
w/v	Weight per volume
rpm	Rotations per minute
mmol	Millimoles
R.T	Room temperature
MSNs	Mesoporous silica nanoparticles
CDI	Carbonyl diimidazole
MCM	Mobil crystalline materials
SBA	Santa Barbara Amorphous type material
CTAB	Cetyltrimethylammonium bromide
LCT	Liquid Crystal Template
TEOS	Tetraethyl orthosilicate
APTES	Aminopropyl triethoxysilane
AMSN	Amine functionalized mesoporous silica nanoparticle
RB	Rhodamine B
MB	Methylene Blue
RITC	Rhodamine isothiocyanate
FITC	Fluorescein isothiocyanate
RBS	Rhodamine B-APTES adduct
HMSN	Hollow mesoporous silica nanoparticles
NIR	Near Infra Red

D.H ₂ O	De-ionized water
EDC	1-ethyl-3(3-dimethylaminopropyl)carbodiimide
NHS	N-hydroxy succinimide
Glu	Glucose monohydrate
Mal	Maltose
Rib	Ribose
Raffi	Raffinose pentahydrate
BET	Brunauer-Emmett-Teller
BJH	Barrett-Joyner-Halanda
SEM	Scanning electron microscopy
XRD	X-ray diffraction spectroscopy
FT-IR	Fourier transform infrared
<i>E.Coli</i>	Escherichia coli
<i>B.Subtilis</i>	Bacillus subtilis
CFU/ml	Colony forming units per milliliter
OD	Optical density
NB	Nutirent broth

Chapter 1

Introduction

1.1 Significance of the work

Over the past two decades, mesoporous silica nanoparticles (MSNs) have attracted extensive attention from the scientific community because of their intrinsic characteristics such as high surface area, well-ordered porosity, and tunable geometry. These features put forward MSNs as an excellent platform for many biomedical applications including bioimaging and drug delivery [[1], [2]]. Biomarkers with high biocompatibility, low toxicity, and dispersibility are essential for understanding the biological processes impact and the activity of therapeutic compounds inside biological systems [3]. Fluorescent MSNs shows excellent biocompatibility with low toxicity, high hydrophilicity, optical transparency, and the silica surface can be functionalized with various biomolecules. So far, a wide variety of fluorescent silica nanoparticles have been used as bioimaging probes.

Use of naked organic dye molecules in imaging and detection of biomolecules can suffer from several disadvantages such as photobleaching, aggregate formation, blinking, bio-incompatibility, and low quantum yield. Fluorescent dyes protected by polymer coatings also have drawbacks such as dye quenching and are highly unsuitable under physiological conditions. These limitations can be overcome by encapsulating the dye molecules, which protects them from chemical reaction [4]. Among various kinds of nanomaterials, fluorescent silica nanoparticles have been extensively used for imaging biological cells *in vitro* as well as *in vivo* [5]. Firstly, this is because silica nanoparticles doped with fluorescent molecules are capable of carrying thousands of dye molecules in each silica matrix [2]. For example, the emission and excitation wavelengths of each Rubpy dye-doped nanoparticle are equivalent to thousands of naked dye molecules [[6], [7]]. Secondly, the incorporation of fluorescent molecules into the silica matrix protects the dye molecules from external quenching and degradation in biological solutions while improving the chemical stability

and biocompatibility of the dye molecule. Therefore, the encapsulation of the dye molecule in a silica matrix improves its photostability and meets the need for extended time tracking *in vivo*.

Furthermore, the rich silane chemistry of the silica nanoparticle surface facilitates a range of biological applications, as the surface can be further functionalized with bioactive molecules such as DNA, antibodies and therapeutic drugs [[8], [9], [10]]. In addition to this, the dye-doped MSNs are capable of carrying a huge load of therapeutic drug molecules inside the pores, which makes them useful as theranostics. Since 2001, MSNs have been conjugated with various bioactive molecules, glycans (free carbohydrates, glycoproteins, and glycolipids) which are important for many biological events [[11], [12]]. Carbohydrates and their conjugates play a crucial role in the detection of bacterial infections and various complex biological processes such as cell communication and trafficking, tumor genesis and progression, immune response, fertilization, and cell apoptosis [[13], [14]]. Therefore, carbohydrate conjugated nanoparticles can go close to the cells and have applications ranging from bio-labeling, *in vivo* bioimaging, and glycan-protein interactions [[15], [16]]. Despite many applications, there are few reports on the synthesis of sugar-coated MSNs, and no reports are available on maltose, ribose, and raffinose coated MSNs.

1.2 Aim of the research

The main aim of this research is to develop novel carbohydrate-conjugated dye incorporated mesoporous silica nanoparticles and to investigate their uptake by bacterial cells for further applications as theranostic agents. During this research work, a single pot synthesis method has been developed for simultaneous incorporation of rhodamine B through covalent attachment into the silica matrix and amine functionality on the surface of MSNs by slightly modifying the co-condensation process. A brief outline of this project is described below.

1. Synthesis of dye encapsulated mesoporous silica nanoparticles with the dye molecule incorporated into the silica matrix by covalent and non-covalent attachment approaches. The effect of reagent concentrations on the surface properties of methylene blue doped amine modified MSNs (MB AMSNs).
2. Synthesis of carbohydrate conjugated fluorescent mesoporous silica nanoparticles. The carbohydrates conjugated to the amine grafted fluorescent MSNs by using carbonyl diimidazole (CDI) as linker agent.
3. Investigation of the cell uptake of glucose conjugated methylene blue doped MSNs into *E.Coli* and *B.Subtilis* by SEM and confocal microscopy.

1.3 Structure of the thesis

This thesis is written according to the guidelines of Murdoch University.

Chapter 1- Introduction: This chapter gives a brief introduction and significance of the present work, followed by the aim of the research and structure of the thesis.

Chapter 2- Review of the literature: This chapter reviews the literature regarding the invention of MSNs, strategies, and mechanisms that have been described in the literature for the formation of MSNs, the effect of synthesis parameters on the morphology, surface conjugation techniques, and medical applications in the field of bioimaging and drug delivery. Finally, it will examine the applications of glyconanoparticles in biomedicine.

Chapter 3- Synthesis and characterization of Dye-doped AMSNs: This chapter gives information about the methods that were employed for the synthesis of the dye-doped AMSNs by covalent and non-covalent approaches and discusses the characterization studies. It also discussed the effect of reagent concentrations on the surface properties of non-covalently incorporated MB AMSNs.

Chapter 4- Synthesis and characterization of carbohydrate coated dye-doped MSNs: This chapter presents the synthesis method of the glyconanoparticles by using zero crosslinking agents. In brief, it deals with the conjugation of carbohydrates glucose (monosaccharide), maltose, ribose (di-saccharide), and raffinose pentahydrate (trisaccharide) on to the methylene blue-doped MSNs and presents the characterization of the glucose conjugated methylene blue doped MSNs.

Chapter 5- Nanoparticle uptake by bacterial cells: This section of the thesis focuses on the investigation of the uptake of as-synthesized glucose coated MB doped MSNs by *E.Coli* and *B.Subtilis* bacterial cultures.

Chapter 2

Review of the Literature

This chapter reviews the existing studies on fluorescent mesoporous silica nanoparticles for biomedical applications. It begins with a brief introduction to the synthesis of various types of mesoporous silica nanoparticles (MSNs) that have been used in imaging and targeted drug delivery.

Porous materials

Porous materials are mainly classified into three categories according to their pore size (Fig 2.1)[17].

Microporous - pore diameter of < 2 nm.

Mesoporous - pore diameter of 2-50 nm.

Macroporous - pore diameter of > 50 nm.

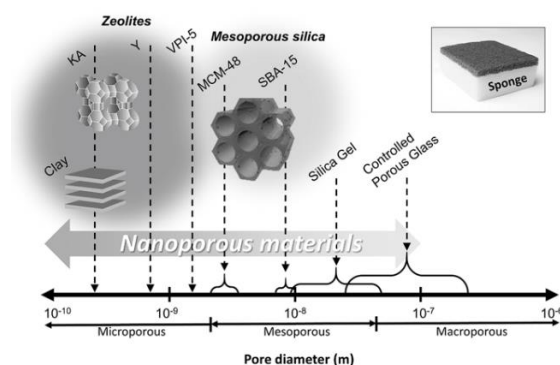


Figure 2.1: Classification of porous materials (Reproduced from Malgras et al., 2015) [17]

Mesoporous materials are of great interest because of their intrinsic characteristics such as narrow pore size, uniform pore structure, large pore volume, high surface area, and easy surface functionalization. These unique features make mesoporous materials potential candidates in biomedicine, energy storage, and catalysis [[18],[19]].

Since the first discovery of M41S family of nanostructured mesoporous material in 1992[20], various types of mesoporous materials have been synthesized with many different compositions including metal oxides[21], metal sulfides[22], polymers [23] and carbon[24] under a wide range of pore geometries such as 2D hexagonal, cubic, and lamellar (Fig 2.2)[25].

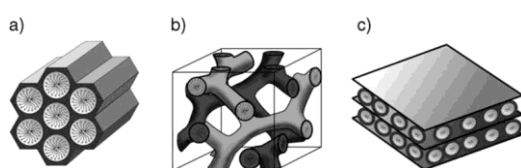


Figure 2.2: Structure of mesoporous M41S materials (a) MCM-41 (2D hexagonal, space group $p6mm$), (b) MCM-48 (cubic, space group $Ia-3d$) and (c) MCM-50 (lamellar, space group $p2$) (Reproduced from Hoffmann et al., 2006)[25]

2.1 Background of Mesoporous silica nanoparticles (MSNs)

In 1971, V.Chiola et al. [26] reported the synthesis of “low bulk density silica” by hydrolyzing and condensing tetraethylorthosilicate in the presence of a cationic surfactant. This was patented by Sylvania Electric Products Inc., in the same year. However, the patent concerned only the bulk density property of the precipitated product. It did not mention anything about the characteristic properties such as geometry and porosity of the obtained material. Subsequently, the synthesis of mesoporous silica nanoparticles from aluminosilicate gels, using a liquid crystal template mechanism was reported by Mobil Research and Development Corporation in 1992 [20]. They named the synthesized material as Mobil Crystalline Material or Mobil Composition of Materials (MCM-41).

The invention of MCM-41 led to the synthesis of a wide variety of mesoporous silica materials with various pore geometries and diameters (Fig 2.3)[19]. The change in the mesoporous nature and their structural arrangement is due to the change in the metal precursor, reaction parameters

and the type of structural directing agents that were used as a template. Moreover, the pore structure and the order of the pores could be altered through the choice of the surfactant.

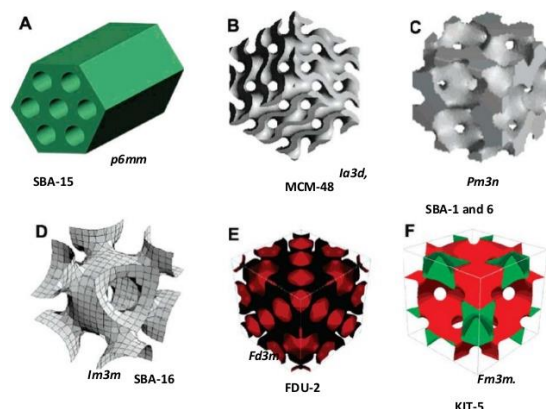


Figure 2.3: Various pore geometries (A) 2D hexagonal $p6mm$, (B) 3D cubic $Pm3m$, (C) $Pm3n$, (D) $Im3m$, (E) $Fd3m$, and (F) $Fm3m$ (Reproduced from Lu et al., 2016)[19]

MCM-41 is hexagonal with a pore diameter of 2.5 to 6 nm. The cationic surfactants used in the synthesis act as structural directing agents. This type of mesoporous silica has been widely investigated for biomedical applications. The other widely explored materials are MCM-48, which has a cubic arrangement and MCM-50 that has a lamellar-like arrangement (Fig 2.2).

Subsequently, Zhao et al. from the University of California, Santa Barbara, synthesized a family of highly ordered amorphous type mesoporous silicas with pore range 2-30 nm by the use of commercially available non-ionic triblock copolymers such as alkyl poly(ethylene oxide) (PEO), oligomeric surfactant and poly(alkylene oxide) block copolymer as the templates in the acidic media. They named these as Santa Barbara Amorphous type materials (SBA) [27]. They obtained a wide variety of mesoporous silica materials including SBA-11 (cubic), SBA-12 (3D hexagonal), SBA-15 (hexagonal), and SBA-16 (cubic cage structure) with various geometries and pore symmetries, by varying the ratio of ethylene oxide to propylene oxide (Fig 3). SBA-15 has been widely used in biomedicine [28].

Some other widely studied mesoporous silica materials in the literature are FSM-16 [29], which have a folded sheet type geometry synthesized by using quaternary ammonium surfactant as template and layered polysilicate kanemite as silica source, TDU-1 (Technical Delft University) [30], HMM-33 (Hiroshima Mesoporous Material-33) [31], COK-12 (Centrunvoor Oppervlaktechemieen Katalyse), KIT-5 (Korea Advanced Institute of Science and Technology)

[32], FDU-1 (Fundan University)[33]. The structural characteristics and applications of some MSNs are listed in Table 2.1.

Table 2.1: List of structural characteristics and applications of some MSNs.

MSN type	Pore geometry	Pore size (nm)	Pore volume(cm ³ /g)	Applications	Reference
MCM-41	2D hexagonal $P6mm$	2-8	>1.0	Biomedicine, catalysis	[34]
MCM-48	3D cubic $Ia3d$	2-5	>1.0	Biomedicine, catalysis	[35]
MCM-50	Lamellar $p2$	2-5	>1.0	Adsorbent in catalysis	[36]
SBA-11	3D cubic $Pm3m$	2-4	0.68	Adsorbent in catalysis	[37]
SBA-12	3D hexagonal, $p63/mmc$	3.1	0.83	Adsorbent in catalysis	[38]
SBA-15	2D hexagonal $p6mm$	6	1.17	Biomedicine, catalysis	[39], [40]
SBA-16	Cubic $Im3m$	5-15	0.91	Biomedicine, catalysis	[41], [42]
FSM-16	Hexagonal	1.6-4.5	-	Catalysis, adsorbent	[43, 44]
KIT-5	Cubic $Fm3m$	9.3	0.45	Catalysis	[45]
COK-12	Hexagonal $P6m$	5.8	0.45	Catalysis	[46]
FDU-12	Cubic $Fm3m$	10-12.3	0.66-0.78	Catalysis	[47]

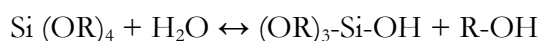
2.2 Approaches for the synthesis of MSNs

Various synthesis methods have been reported in the literature [[25],[48] , [49], [50]] to produce mesoporous silica materials with high surface areas, large pore volumes, different particle sizes, high thermal stability, and biocompatibility. The synthesis of MSNs is mainly based on using surfactants as a structural directing agent with the most popular methods including the sol-gel [[49], [51]], template-assisted [[52], [25]], microwave-assisted [[53], [54], [55]], and chemical etching [[56], [57]] techniques.

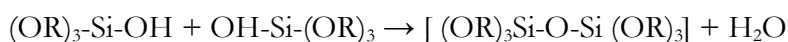
2.2.1 Sol-gel technique

The sol-gel process is a wet chemical technique which is widely used in ceramic engineering. In 1968, Werner Stober developed a bottom-up method for producing nearly monodispersed silica nanoparticles with a narrow range of sizes based on the sol-gel technique in basic media [58]. From then on, the process was known as the Stober method and it became widely employed for producing silica nanoparticles. A colloidal suspension, which is called a 'sol' is prepared for the growth of the inorganic network, and then a gelation process of the sol is carried out to form a continuous inorganic network in a liquid phase known as 'gel'. The chemical reaction for the synthesis of silica nanoparticles can be seen in Scheme 2.1.

Hydrolysis of tetraalkoxysilane (silica precursor)

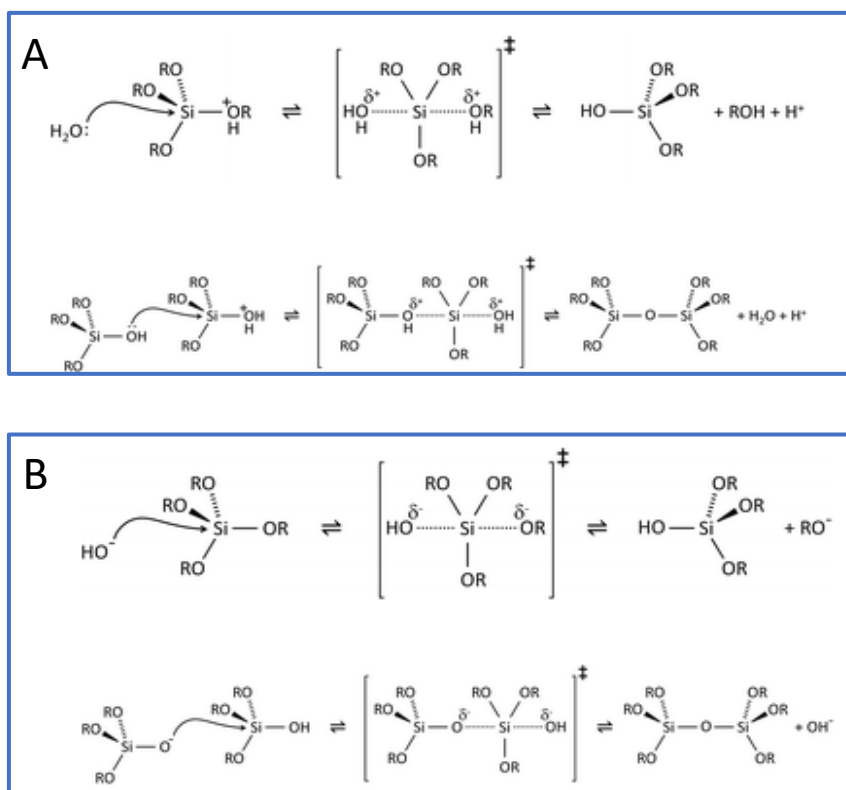


Condensation of hydrolyzed silicate precursor



Scheme 2.1: Hydrolysis and condensation of tetra alkoxy silane precursor during the sol-gel process

Usually, the hydrolysis and condensation procedures take place in the presence of an acid or base catalyst. The mechanisms under acid and base-catalyzed reactions can be seen in Scheme 2.2. However, the rate of hydrolysis is faster in the presence of a base catalyst. Furthermore, the rate of condensation depends upon the degree of hydrolysis [59]. The sol-gel technique is simple, effective and operates at ambient temperatures. Therefore, the control over the particle morphology is relatively high when compared with other techniques. In addition to this, surface functionalization of MSNs can take place in a single step.



Scheme 2.2: Acid-catalyzed hydrolysis and condensation (A), base-catalyzed hydrolysis and condensation (B) (Reproduced from Danks et al., 2016)[59]

2.2.2 Template assisted technique

The template-assisted technique is very easy and relatively cheap way of producing ordered mesoporous materials. In this technique, the morphology of the nanocrystals can be changed by controlling the nucleation and growth of the nanoparticle during the synthesis. This technique can be divided into two categories. The first one is a hard-templating method, also known as an exo-template method in which a solid is used as a structure directing agent. The other one is a soft-templating method or endo-template method, in which a soft matter is used for the synthesis of ordered mesoporous materials [[60], [52]]. For both approaches, there are three common steps.

Step 1: Preparation of the template

Step 2: Synthesis of targeted nanoparticles in the presence of the template by common synthetic approaches (sol-gel, hydrothermal, or microwave-assisted).

Step 3: Careful removal of the template by extraction or calcination.

Hard template method:

A hard and rigid substance determines the pore size, particle size, and morphology of the synthesized particle in the hard template (exo-template) method. A wide variety of hard templates are reported in the literature[52]. In the typical procedure, the void spaces in the hard template are filled with the silica precursor in the presence of a catalyst, which is then polymerized into silica (Fig 2.4). The template is then removed by a physical or chemical process, which results in a negative replica of the framework. Therefore, mesoporous nanoparticles with rigid pore size and morphology can be obtained. Even though this method provides good control over particle morphology, the resulting rigid sizes and geometries can be a limitation. In addition to this, the removal of the template is difficult and may cause damage to the structure of the nanoparticles.

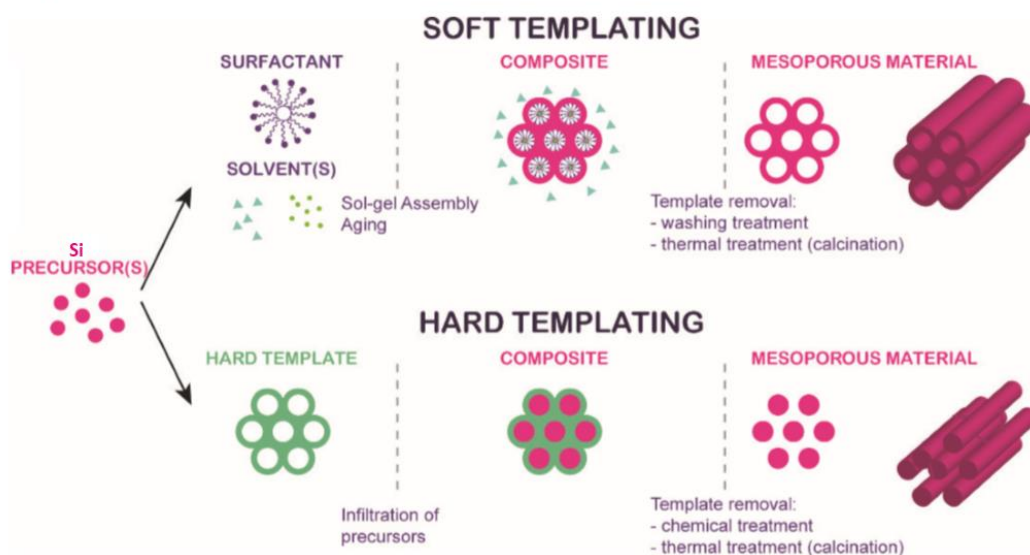


Figure 2.4: A schematic diagram of soft templating and hard templating methods (Reproduced from Barbara et al., 2017) [61]

Soft template method:

Various types of surfactants, including cationic, anionic, and neutral, are reported in the literature for use in the soft template method. The surfactant is used to form micelles that act as templates, and the silica precursors are condensed around the micelles. Therefore, the structure of the mesoporous material depends upon the structure of the aggregated micelles (Fig 2.4). This type of template method is particularly important because of the reproducibility and simplicity of the

process. Moreover, the removal of surfactant is simple (extraction or calcination), and it does not cause any damage to the morphology of the obtained nanoparticle [[62], [63]].

2.2.3 Microwave assisted (MW) technique

Microwave-assisted (MW) synthesis of MSNs is a relatively new technique that has many advantages over other methods. In particular, the process is quick, and the temperature distribution is uniform throughout the reaction mixture. Hydrothermal synthesis of inorganic materials using MW heating promotes the nucleation and hence reduces the synthesis time as well as the particle size[64]. The synthesis of MCM-41 and SBA-15 type of MSNs via MW heating and CTAB surfactant have been reported [[53], [54]]. Nur et al. [65] synthesized MSNs via the MW method for drug delivery applications. They found that the crystal growth was enhanced if the power of the MW increased from 100 – 450 W

Furthermore, the MW technique can be used in conjugation with other techniques [[66], [67]]. For example, Shan et al. [67] used MW assisted aerosol technique for the fabrication of silica hollow spheres (SHS). They stated that this was an efficient way for the fabrication of SHS and the morphology of the SHS could be easily tuned by varying the ratio of precursors. Although the MW technique has advantages, the control over the particle size and morphology is poor and the reaction monitoring is difficult. In addition to this, the equipment for this process is quite expensive and is not suitable for scale-up[68].

2.2.4 Chemical etching

In the chemical etching approach, nanoparticles can initially be synthesized by any of the previously mentioned techniques such as sol-gel or microwave methods. The resultant particles are then chemically etched to remove specific chemical structure or elements using chemical or physical treatments. This method is widely employed for producing hollow mesoporous silica nanoparticles (HMSNs).

Liu et al. [69] synthesized rattle-like MSNs (RMSNs) with a pure silica core, a hollow cavity, and mesoporous shell via a “surface-assisted selective etching” strategy. The obtained RMSNs had an average diameter of 290 nm, shell thickness 35 nm, and solid core size about 90 nm. They found that using a surfactant with different length of alkyl chain C_n TAB in the outer shell plays an important role in the formation of rattle-like structure. Wu et al. [70] proposed a salt-assisted acid etching (SAAE) strategy for the construction of RMSNs. They named them as hollow mesoporous

organosilica nano-vehicles (HMOVs). They found that SAAE overcomes the drawbacks of the traditional silica etching methods such as alkaline etching, HF (hydrofluoric acid) etching, and avoids by-products. HMOVs were suitable for high drug loading capacity and pH-responsive drug releasing behavior.

Recently, Xu et al. [71] prepared multifunctional yolk-shell structured mesoporous silica nanoparticles (YMSNs) suitable for fluorescence imaging, photothermal therapy (PTT), and drug delivery. In the actual process, a fluorescein isothiocyanate dye-doped silica nanoparticle partially covered by patchy gold as the core. The used “alkali etching strategy” selectively occurred in the CTAB/silica hybrid layer, which creates void space in YMSNs. The obtained YMSNs showed good biocompatibility, high drug loading capacity (8.04 wt %) and could be used for chemo- and photothermic combination therapy as well as optical imaging. YMSNs can also be prepared by cationic surfactant assisted selective etching. Fang et al. [72] have developed this strategy for the synthesis of high-quality HMSNs with either wormhole-like or oriented mesoporous shell (Fig 2.5). They proposed the mechanism, which involves the etching of solid silica accelerated by cationic surfactant followed by the redeposition of dissolved silica species directed by the cationic surfactant. This method of approach can be a general strategy to produce yolk-like structures from silica coated materials.

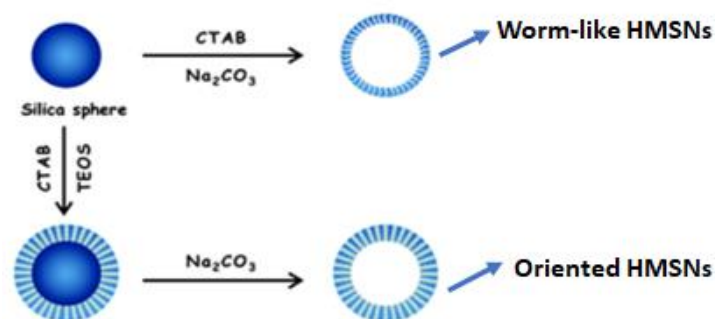


Figure 2.5: Schematic illustration of cationic surfactant assisted selective etching (Reproduced from Fang et al., 2011) [72]

Very recently, Tao et al. [73] also used a mild alkaline solution such as sodium carbonate solution as the etching agent for the synthesis of yolk-shell structured mesoporous organo-silica nanoparticles. The obtained particles had monodispersed diameter (320 nm), large pore volume (1.0 cm³/g), high surface area (1327 m²/g), and mesopores (2.4 nm). Additionally, the material showed a high drug loading capacity up to 181 µg/mg. Adapting the above-mentioned strategies

for the synthesis of HMSNs has benefits over soft-templating methods particularly in the field of biomedicine because the micelles formed in the soft-templating method are very sensitive to the liquid environment [56].

In addition to the above-mentioned techniques, micro-emulsion, aerosol, and vapor deposition methods [74] are also reported in the literature for the synthesis of MSNs.

2.3 Mechanism for the formation of MSNs

For MSNs to be ideal candidates for the biomedical applications, the particles should be monodispersed with uniform pore size and large pore volume, which enables loading of a large number of drug molecules into the pores. These attributes can be attained by controlling the synthesis parameters such as pH, temperature, concentrations of reagents, and surfactant. The type of surfactant used in the synthesis of MSNs plays an important role in directing the pore geometry, size, and volume[49].

Grun et al. [75] reported the synthesis of spherical shaped MCM-41 rather than the standard hexagonal shape by using a cationic surfactant as a structure directing agent. They observed that the spherical-shaped MCM-41 particles showed similar properties to the hexagonal ones. Usually, the formation of MSNs occurs by a 'crystal template mechanism' in which, hydrolysis and condensation of silica take place on the surface of the surfactant micelles. [[76], [77], [78]]. Therefore, the type of surfactant will determine both the pore size and structure of the MSNs.

Surfactants have two main components; one end of the molecule is hydrophilic in nature and the other end is hydrophobic (Fig 2.6). Owing to this amphiphilic character, surfactants can lower the interfacial tension between the two phases.

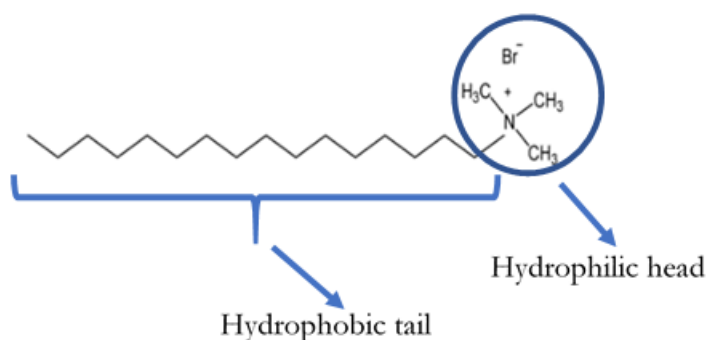


Figure 2.6: Structure of CTAB surfactant

Based on the charge on the polar head, surfactants can be divided into four types.

- (1) Cationic surfactants: These types of surfactants have a positively charged hydrophilic head (polar group) and a large alkyl chain as the hydrophobic tail (non-polar group). A large variety of this class of surfactants is based on nitrogen compounds such as quaternary ammonium salts with a long alkyl chain. Some examples of cationic surfactants are CTAB, CPC (Cetylpyridinium chloride), BZC (Benzalkonium Chloride), DODAB (Dioctadecyldimethyl ammonium bromide).
- (2) Anionic Surfactants: These types of surfactants have a negatively charged polar head and long hydrocarbon tail which serves as a non-polar end. Mostly carboxylates, sulphates, and sulfonates serve as the polar head. Anionic surfactants are usually cheaper than cationic surfactants.
- (3) Non-ionic surfactants: These types of surfactants do not ionize in aqueous solutions as their hydrophilic head is of a non-dissociable type such as phenol, ether, or amide. These surfactants are made hydrophilic by the presence of a polyethylene glycol chain. Poly (propylene oxide) is the most commonly found non-polar group in this type of surfactants. Low molar mass block copolymers composed of blocks of different polymerized monomers are also members in this family of surfactants.
- (4) Amphoteric or zwitterionic surfactants: These types of surfactant molecules can dissociate into both anionic and cationic groups. In general, the positive charge is given by an ammonium group and negative charge obtained by a carboxylate group.

Some surfactants can be soluble in water as a single molecule and others occur in the interface between two phases (liquid-air or liquid-solid). Once a surfactant reaches saturation state, the surfactant forms clusters called micelles. The point where the first micelle is formed is called the Critical Micelle Concentration (CMC). The chemical structure and the length of the hydrophobic tail, determine the CMC. CMC is inversely proportional to the length of the hydrophobic chain. Many different mechanisms have been proposed in the literature to explain the formation of MSNs, such as liquid crystal template mechanism (LCT) [77], cooperative self-assembly mechanism [79], and synergistic mechanism [80],[81]. The common characteristic among these mechanisms is that the surfactant activates the solvated silica precursor to form a mesoporous structure. Time-resolved small-angle neutron scattering (SANS) was used to study the formation of MSNs by the LCT mechanism [80]. This method helped to predict the changes occurring simultaneously during the formation process. In the early hydrolysis, silicate ions adsorb around the surfactant micelles during the nucleation. In the process of hydrolysis and condensation of the

silica precursor, the charge around the surfactant micelles reduces and the inter-micellar repulsions, allowing the further formation of small aggregates of silica

The synthesis of MSNs by CTAB surfactant via the liquid crystal template mechanism was first proposed by Davis et al. [82] (Fig 2.7). According to this mechanism, the micelles formed in aqueous conditions are further evolved into rod-like (2D hexagonal shape) micelles. The core of the hexagonal micelles consists of hydrophobic tails and the surface consists of hydrophilic heads. The silica precursor begins to hydrolyze and condense between these hexagonal micelles and is deposited on the surface of the micelles. This is because the negatively charged silanolate ions (Si-O^-) can electrostatically link to the positively charged CTAB- $\text{N}^+(\text{CH}_3)_3$. Finally, the removal of the surfactant template by calcination or acidic ethanol extraction leaves the pores. These pores mimic exactly the structure of the mesoscale soft template. This mechanism is simple and widely accepted by many researchers.

Another mechanism known as the 'synergistic mechanism' was put forward by the MCM group [21]. The main difference is that the synergistic mechanism considers the liquid crystal to be produced after the addition of the silica precursor. Moreover, this mechanism can explain how low surfactant concentrations could lead to the formation of MSN with different pore structures and order. The 'swelling-shrinking mechanism' was recently proposed by Zhifeng Yi et al., [81] for MSNs formation. This mechanism was studied by time-resolved synchrotron small-angle X-ray scattering (SAXS). This mechanism is highly acceptable when tetraethyl orthosilicate (TEOS) is used as the metal precursor in the absence of ethanol because TEOS is an oily like substance that forms an emulsion-like system under vigorous stirring. When TEOS is added to the formed CTAB micelles in an aqueous solution, it interacts with the hydrophobic end, which results in the transformation of the ellipsoidal shape into spherical. During subsequent hydrolysis, the TEOS becomes hydrophilic and released into the aqueous solution whereas the negatively charged hydrolyzed monomers of TEOS adsorb onto CTAB micelles due to electrostatic attractions. The micelles become small and shrink once TEOS is consumed completely. The process of getting small continues until all the TEOS gets hydrolyzed which forms silica shell around the micelles.

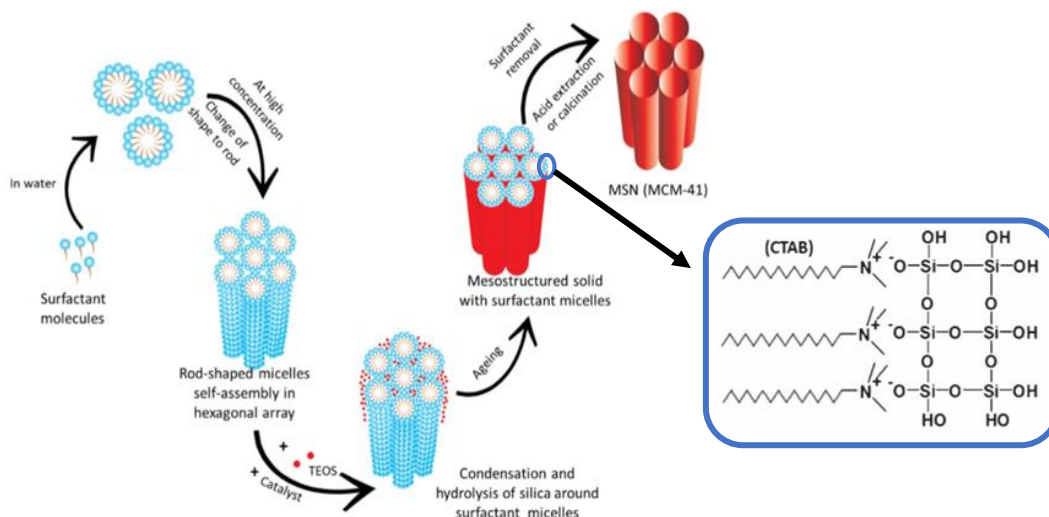


Figure 2.7: Formation of MCM-41 by Liquid Crystal Template (LCT) mechanism (Reproduced from Davis et al., 1994) [82]

CTAB is a cationic surfactant and quaternary ammonium compound with bromide as the counterion. Cationic surfactants with different hydrophobic chain lengths are available (Fig 2.8). Usually, the particle size decreases as the chain length of the surfactant increases [83]. CTAB is highly investigated for the synthesis of MSNs.

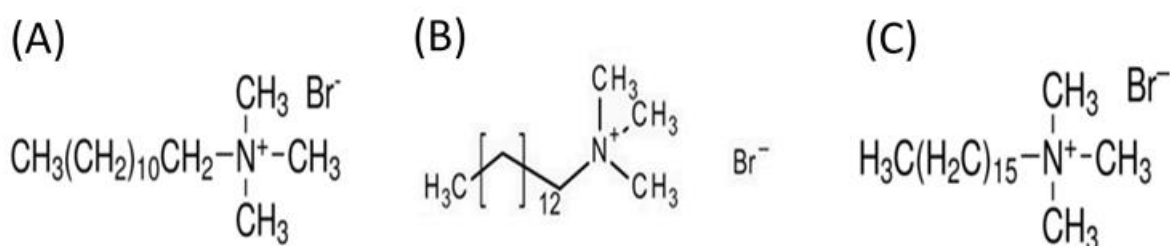


Figure 2.8: Structures of series of cationic surfactants (A) Dodecyltrimethylammonium bromide (DTAB), (B) Tetradecyltrimethylammonium bromide (TTAB), and (C) Hexadecyltrimethylammonium bromide (CTAB).

2.4 Effect of synthesis parameters on the characteristics of MSNs

For the efficient application of MSNs in biomedicine, it is crucial to control the particle morphology and pore geometry. Because several *in vivo* and *in vitro* applications of particles depend on their size. The desired particulate diameter for the biomedical applications is less than 400 nm. The size of the particle is highly correlated with their ease of uptake into the human vascular system and ease of excretion out of the body [84]. Therefore, the precise control over particle size and porosity is of great interest for high therapeutic efficacy. In addition to this, smaller size is highly desired for usage at subcellular locations after crossing several physiological barriers such as BBB (blood brain barrier)[85].

Tetraethyl orthosilicate (TEOS) is widely used as the metal precursor in the synthesis of MSNs. Tetramethyl orthosilicate (TMOS) [86], tetramethoxy vinylsilane (TMVS) [87], sodium metasilicate (Na_2SiO_3) [88], tetrakis (2-hydroxyethyl) orthosilicate (THEOS) [89], and some natural sources such as renewable biomass (42), pumice rock, and rice husk [90] have also been explored for synthesis of MSNs. The present review focuses on the MSNs synthesized from TEOS. TEOS is the preferred silica precursor rather than TMOS and Na_2SiO_3 because the pores obtained from TEOS based aerogels show a narrow size and the particles have high hydrothermal stability, which is highly regarded in biomedicine. Additionally, TMOS is more reactive than TEOS. Therefore, the control over the particle morphology is much lower [91].

According to literature, the geometry of the pores is largely decided by the surfactant's properties[83]. Additionally, customizing the synthesis parameters including the rate of hydrolysis, the ratio of surfactant to silica source, pH of the reaction media, and the type of catalyst (acid or base) significantly affect the nanoparticle morphology.

2.4.1 Control of Particle Size

Careful tuning of the particle size is highly regarded because the size of the nanoparticle significantly affects its applications in biomedicine, such as the efficacy of endocytosis, biosensing, and drug loading and release. For example, MSNs with a particle size of 50 nm exhibited more cellular uptake than other particles in the range 30-280 nm [92]. He et al., [93] reported that MSNs with particle sizes in the range 190-420 nm, exhibited high cytotoxicity (at concentrations above 25 $\mu\text{g}/\text{ml}$) compared with the particles 1220 nm (at a concentration range of 10-480 $\mu\text{g}/\text{ml}$).

Extensive research has been performed by varying synthesis parameters to get the desired particle size.

Lv et al. [94] have studied systematically the effect of the reaction parameters (stirring rate, base concentration, and reaction temperature) on the particle size. They found that increasing the temperature (from 40 to 95^o C) increased the particle size (from 21 nm to 38 nm). Conversely, a slight increase in the base concentration and a significant increase in the stirring rate resulted in a decrease in the particle size (Fig 2.9). They found that the concentration of the surfactant micelles also plays an important role in size reduction because a low reaction temperature and rapid stirring rate will give a low concentration of silica-surfactant micelles. This minimizes the growth of particle size, which results in MSNs with small diameters.

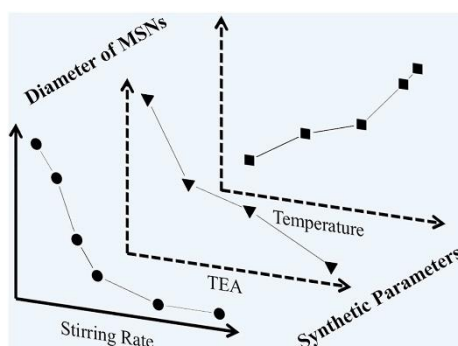


Figure 2.9: Graphical abstract of the effect of synthesis parameters on particle size (TEA-Triethanolamine (Base))(Reproduced from Lv et al., 2016) [94]

Moreover, replacing base catalysts such as sodium hydroxide (NaOH) and ammonium hydroxide (NH₄OH) with TEA (triethanolamine) also resulted in smaller particles as TEA can act as a surface capping ligand and suppress the particle growth and prevent particle agglomeration [95]. Use of L-lysine as a base-catalyst could also result in a decrease in particle size because of the delayed condensation due to the electrostatic interaction between the protonated amine group of L-lysine and deprotonated hydroxyl groups on the silica surface [96]. Ya-Dong et al. [97] studied the effect of reaction parameters on the size of the nanoparticles by Taguchi method. They found that the pH of the reaction medium had great influence (57%) on the particle size followed by the amount of precursor (13%) and reaction time (29%). Additionally, they found that the pH significantly affected the mesopores structural order. In addition to this, longer reaction times in basic medium caused erosion of the MSNs silica frame.

2.4.2 Control of pore size, pore volume, and meso-structural ordering

Control over pore size and pore volume is crucial for drug loading and drug release. The pore size depends on the type of surfactant. Surfactants with long chain lengths result in MSNs with large pores [98]. Gu et al. [99] have synthesized well-ordered MSNs with a large pore size (diameter up to 4.6 nm) by using CTAB surfactant, N, N-dimethylhexadecylamine (DMHA) as a pore size mediator and tri-block copolymer of F₁₂₇ (EO₁₀₆PO₇₀EO₁₀₆) as a particle growth inhibitor. The concentration of the surfactant also has a significant impact on the order of mesopores. A higher concentration of CTAB surfactant leads to disordered pores, whereas lower concentrations fail to form micelles which result in template deficiency in the reaction medium. The concentration of TEOS also shows the same influence on mesoporous order [97]. A higher concentration of TEOS leads to disordered pores whereas lower amounts are insufficient to form mesoporous orders. Effect of different reaction parameters on the particle size can be seen in Fig 2.10. Therefore, an optimal balance must be maintained between the reagents.

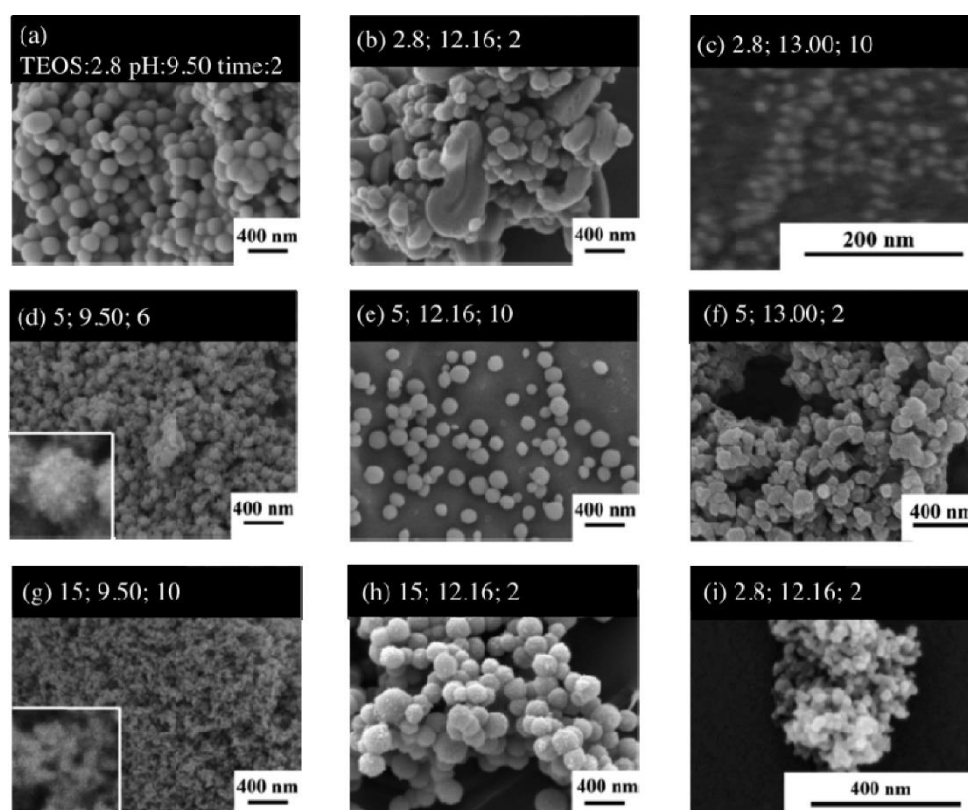


Figure 2.10: SEM images of samples designed by the Taguchi method. The amount of TEOS added, pH, and reaction time represented respectively in each image (Reproduced from Yao Dong et al., 2011) [97].

2.5 MSNs in bioimaging and drug delivery

Bioimaging is an effective method to reveal many biological processes, including enzymatic reactions and disease progression that occur in the biological state. Recent developments in the synthesis of various fluorescent compounds for bioimaging improve our understanding of the complex biological systems at the molecular level.

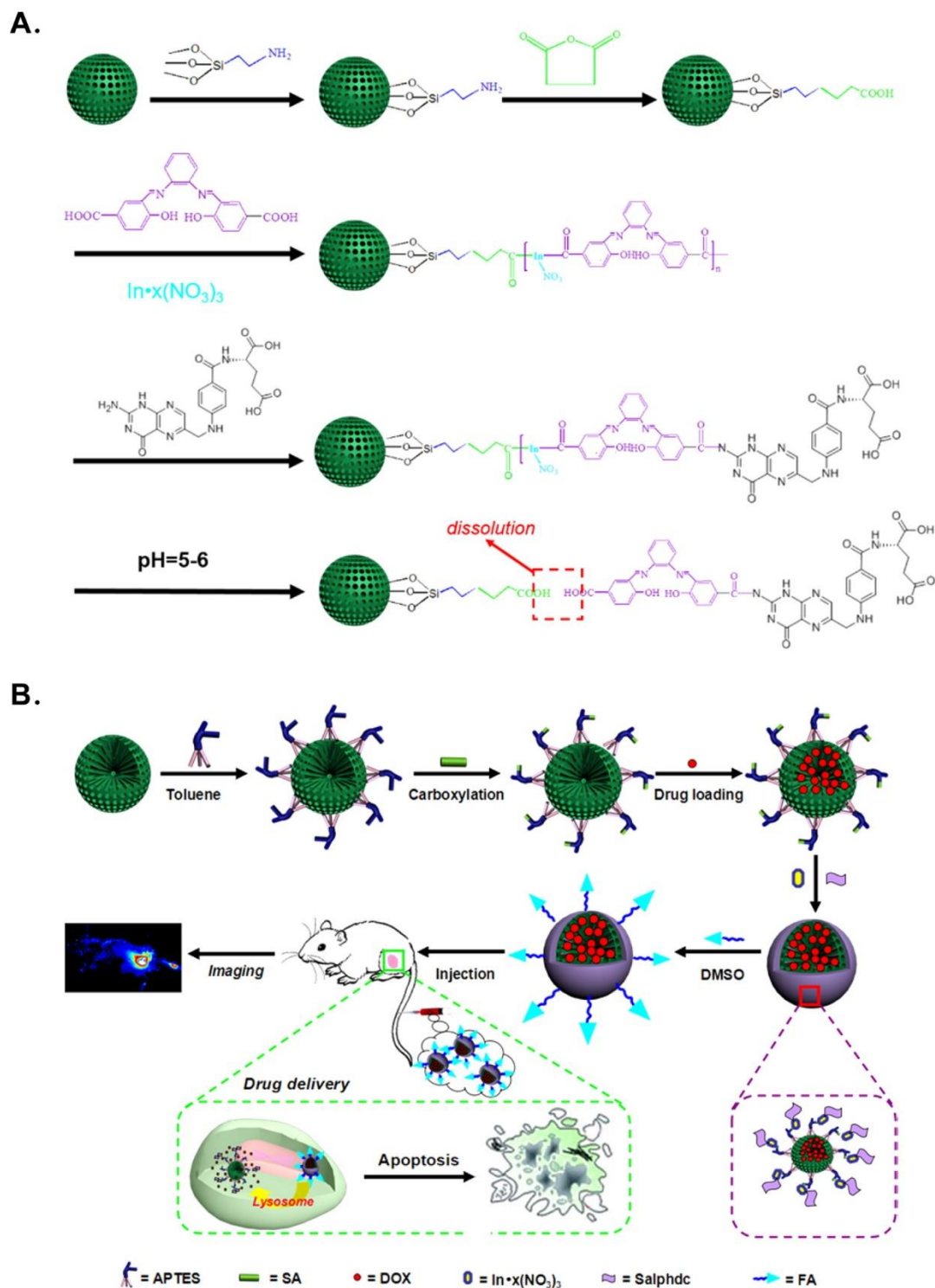
Fluorescent dyes, also known as fluorophores, have been widely used in bioimaging for decades, but their applicability is still limited. This is because of aqueous insolubility, aggregate formation, high reactivity in physiological conditions which result in rapid photobleaching, and small Stokes shifts, which may result in excitation and scattered light interferences. In some cases, the large molecular weight of the dye molecule may interfere with the biomolecules and cause precipitation, which can cause severe side-effects. To overcome these limitations, the surface of the fluorophore must be covered to protect it from the external environment and photobleaching. Out of many kinds of dye encapsulation approaches, doping of dye molecules inside nanoparticles has many benefits. Silica nanoparticles have become an attractive choice for this application.

Firstly, silica nanoparticles show high biocompatibility and low cytotoxicity [100]. Secondly, control over the particle size and surface modification is relatively simple [101]. Thirdly, the silica matrix is transparent. In addition to this, the silica surface is chemically stable and easily water dispersible. Therefore, the chemical stability and biocompatibility of the dye molecule can be significantly enhanced without affecting its fluorescence properties.

Traditional fluorescent dye molecules such as fluorescein and rhodamine as well as their amine derivatives FITC and RITC have been encapsulated into the silica matrices. Van et al. [102] have synthesized colloidal silica spheres with a covalently incorporated fluorophore, FITC by using the sol-gel method. Later, many researchers tried to enhance the fluorescence of dye-doped silica nanoparticles. Metal-enhanced fluorescence (MEF) is a simple method which improves the brightness and photo-stability. The basic phenomenon of MEF arises from the intensification of the incident light caused by exciting surface plasmons of metal nanoparticles or from an increase of the radiative rates of the dye molecule [103]. The plasmonic effect caused by metal nanostructures is mainly dependent on the surface distance between dye and metal [104]. Recently, Luigi et al. [105] investigated the fluorescence behavior of two dyes (Rhodamine B and 9-aminoacridine), which have different spectral properties in the presence of gold nanoparticles with diameters of 2 or 26 nm. First, they encapsulated the covalent dye adduct into the silica matrix by a modified Stöber method to produce the two types of dye-doped silica nanoparticles. Then they

further grew another layer of the silica shell. After that, the silica surface was amine functionalized by APTES. Then the gold colloids were adsorbed on the amine-coated silica surface. Using steady-state and time-resolved fluorescence measurements, they found that despite the distance of metal and dye, a drastic quenching of the dye emission was observed in the presence of 2 nm gold nanoparticles.

Very recently, Ricco et al. [58] synthesized ultra-small fluorescent silica nanoparticles with particle diameter as low as 10 nm by using the classical Stöber method. They have obtained dye-doped silica nanoparticles in size range from 10-70 nm by modifying reaction parameters and molar ratios. Porosity is not a key factor in biosensing, but a porous nature is highly significant for theranostic applications. Cai et al. [106] synthesized dendrimer-like MSNs with hierarchical pores (HPSNs) for imaging as well as pH-responsive nanocarriers for targeted drug delivery using N, N-phenylene bis(salicylideneimine)dicarboxylic acid (Salphdc) as gatekeeper, -COOH of Salphdc and In^{3+} ions as a fluorescence imaging agent, and folic acid (FA) as the targeting unit. Since the HPSN has gradually decreasing pore sizes from the surface to the center of the particle, it facilitates easy drug loading when compared to MSNs. The detailed schematic analysis is represented in Scheme 2.3. The synthesized HPSNs were modified by using amino and carboxyl groups. Then in the presence of dimethylformamide (DMF), Salphdc and $\text{In}(\text{NO}_3)_3 \cdot x\text{H}_2\text{O}$ were added. The formed coordination molecules were deposited onto the HPSN-COOH. The bond between Salphdc and HPSN was sensitive to acid, which made the complex pH-responsive. Finally, FA was grafted to the Salphdc for targeting tumor cells. Generally, FA receptors are overexpressed in many cancer tumors, while healthy body cells have no FA receptors [107].



Scheme 2.3: Construction of pH-Responsive HPSN–Salphdc–FA System: (A) Chemical reaction routes and (B) Drug-loaded HPSN–Salphdc–FA system for tumor therapy and bioimaging *in vivo* (Reproduced from Cai et al., 2015) [106]

Recently, aptamers have been widely used in the detection of cancer cells. Aptamers (peptides or oligonucleic acid molecules) have various benefits such as easy modification, high stability at high

temperatures and low pH values, and economical production over antibodies [108]. Jo et al., [109] developed dual aptamer-modified silica nanoparticles to target two types of breast cancer cells, MUC-1(+) and HER-2(+) cell lines simultaneously. They first synthesized the Ru(BPY)₃ encapsulated silica nanoparticles by reverse microemulsion method. The surface was then grafted by PEG (polyethylene glycol). Further, the PEG-coated silica nanoparticles (PEG-SNPs) were modified by avidin (Avi-PEG-SNP) by cyanogen bromide activation method [110]. Finally, the two aptamers were conjugated to Avi-PEG-SNP by using bovine serum albumin (BSA). The resultant particles showed a robust fluorescent signal, but the study was limited to *in vitro* diagnosis only.

Application of silica nanoparticles in photodynamic therapy (PDT) has increased tremendously [[111], [112]]. Photosensitizers (PS) loaded into nanoparticles can reduce nonspecific damage to healthy cells over free photosensitizers [113]. Recently, scientists tried to incorporate fluorescent contrast agents or magnetic resonance imaging (MRI) contrast agents along with photosensitizers for simultaneous imaging and therapy [114]. Based on this, Wang et al. [115] developed phosphonate terminated methylene blue incorporated silica nanoparticles (MB-PSiNPs) for simultaneous *in vivo* imaging and PDT. They first synthesized the methylene blue (MB) encapsulated silica nanoparticles with the use of TEOS and trihydroxysilylpropyl methyl phosphonate (THPMP) by employing W/O microemulsion method. They found that the MB-PSiNPs can effectively induce HeLa cancer cell death in *in vitro* studies. MB-PSiNPs can also be used for *in vivo* optical imaging due to induced fluorescence to accurate site-directed irradiation and effective PDT. The efficiency of PDT mainly depends on the photosensitizer (PS) efficiency, oxygen concentration, and light characteristic. Recently, Li et al. [116] loaded MB as PS in the silica nanoparticles and the surface was covered by coordination complexes tannic acid (TA) and Fe(III) ions, which formed a core-shell structure. This type of encapsulation helped to delay the thermal degradation of MB and modulated the release behavior of MB when compared with uncovered MB-silica. The efficacy of singlet oxygen (¹O₂) generation by MB released from the silica-MB@TA was higher than that from uncovered silica-MB.

Interestingly, most of the dye-doped mesoporous silica nanoparticles in the literature are based on using reactive dyes such as fluorescein isothiocyanate (FITC) and rhodamine isothiocyanate (RITC) which are expensive. No significant literature is available on methylene blue (MB) doped MSNs, which is widely used in many biological applications for imaging purpose and relatively cheap among the commercially existing Near Infra-Red (NIR) fluorescent dyes [117].

2.6 Glyconanoparticles

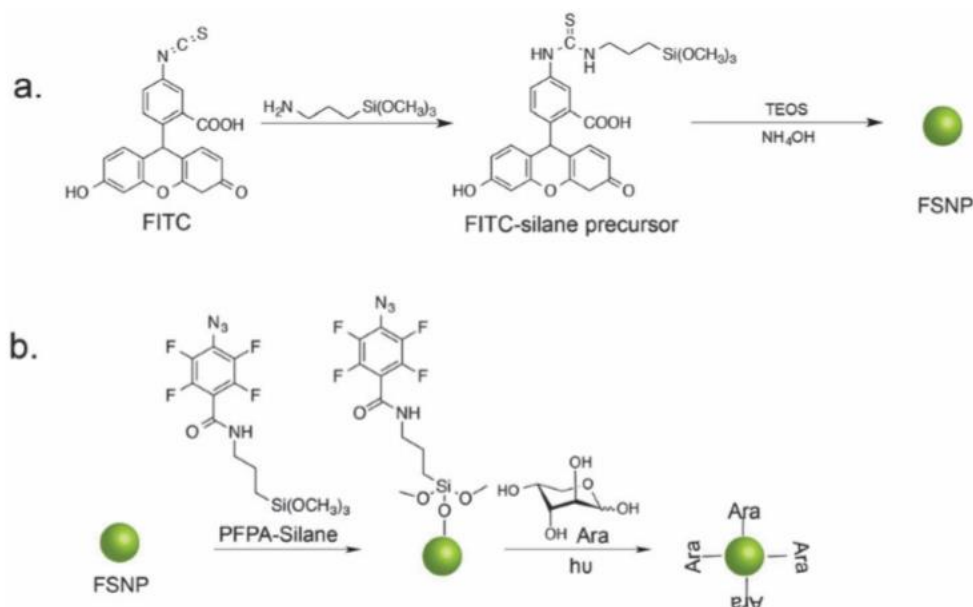
Carbohydrates are crucial in many biological applications, such as new therapeutic drugs and vaccines to treat human diseases [13]. Many viral infections, immune system, and disease progressions such as cancer metastasis are because of carbohydrate-protein interactions occurring at the cell surface. The presence of carbohydrate molecules on the surface of the nanoparticles provides wide scope to reach into biological cells.

Glyconanoparticles (GNPs) have their reduced end attached to an inorganic nanoparticle core by a linker molecule. The first synthesis of GNPs occurred in 2001 by Penades and co-workers [118]. They synthesized the carbohydrate linked to gold nanoparticles to investigate the influence of the carbohydrate on interactions with specific receptors. From then, GNPs became quite significant in biological research. The main types of nanoparticles functionalized with carbohydrates are gold and silver GNPs [[118],[119] , [120], [121]] magnetic GNP [122], and semiconductor GNPs [123]. Nonetheless, the advantage of silica nanoparticles high biocompatibility and low cytotoxicity make them also suitable for GNPs.

Mesoporous silica nanoparticles with carbohydrates as targeting ligands can be used as efficient drug delivery systems. Molecules such as mannose [124], arginine-glycine-aspartate (RGD)[125], hyaluronic acid [126] and lactobionic acid [127], have been used to conjugate MSNs to enhance the antitumor efficiency. Wu et al. have synthesized lactose covered MSNs (Lac-MSNs) with an average particle diameter of 100 nm [128]. The obtained particles possessed highly ordered hexagonal symmetry with an average pore size of 3.7 nm. The results showed that Lac-MSNs could be used as an efficient carrier system for targeted intracellular anti-cancer drug delivery. They have loaded the drug docetaxel (DTX) into the mesopores using the wetness impregnation method. The DTX transported by Lac-MSNs has effectively inhibited the growth of HepG2 and SMMC7721 cancer cells.

Carbohydrate-protein interactions at a cell surface play a crucial role in some biological events such as bacterial and viral infections [129]. Arabinose is the main compound that is present in the walls of mycobacteria, Jayawardhana and group [130] have developed D-arabinose functionalized fluorescein doped silica nanoparticles (Ara@FSNP) for the detection of *Mycobacterium smegmatis* bacteria which is widely found in the sputum of tuberculosis patients. Firstly, they have synthesized the fluorescent nanoparticles by using FITC-silane adduct in the co-condensation method. Then the FSNP was functionalized with perfluorophenyl azide silane (PFPA-silane). Finally, arabinose (Ara) was conjugated on the surface by photocoupling chemistry. The density of arabinose on the

nanoparticle surface was determined by thermogravimetric analysis (TGA) as $3.8 \times 10^{-16} \mu\text{g}/\text{nm}$. An illustration of this synthesis can be found in Scheme 2.4.



Scheme 2.4: (a) Synthesis of FSNP and (b) Conjugation of arabinose on to FSNP by PFPA-Silane intermediate (Reproduced from Jayawardhana et al., 2015) [130]

Also found that nanoparticles conjugated with Ara had higher interactions with the bacteria than the nanoparticles functionalized with glucose, galactose or cyclodextrin. TEM of this observation can be seen in Fig 2.11.

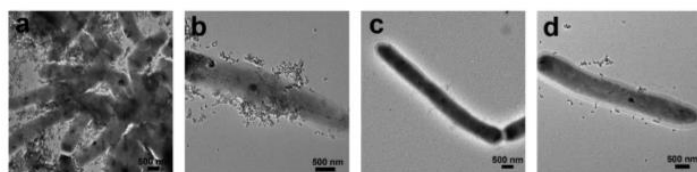


Figure 2.11: TEM images of *M. smegmatis* strain mc2 155 after incubating for 6 h with (a) Ara-FSNPs, (b) Glc-FSNPs, (c) Gal-FSNPs, (d) CD-FSNPs (Reproduced from Jayawardhana et al., 2015) [130]

In another experiment, the same group found that MSNs functionalized with α , α -trehalose and loaded with antitubercular drug isoniazid had higher antimicrobial activity than the free drug [131].

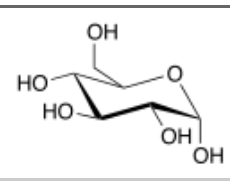
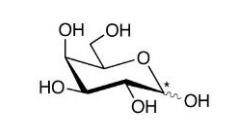
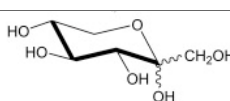
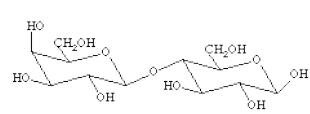
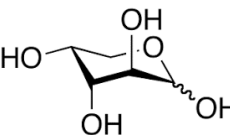
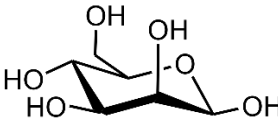
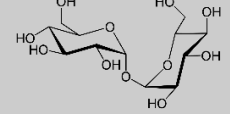
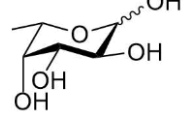
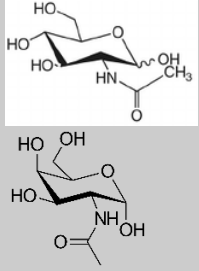
Specific carbohydrate-protein interactions are highly useful in detecting cancer cells and tumor progression. For example, lactose conjugated fluorescent silica nanoparticles have shown higher affinity than cellulose conjugated nanoparticles in binding to galectin-1, an overexpressed galactose-selective lectin at prostate cancer cell surfaces [132]. The presence of carbohydrate is crucial in targeted drug delivery as well. Veronika et al. [133] used the glucose functionalized MSNs loaded with a γ -secretase inhibitor in the mesopores for inhibiting notch activity in breast cancer stem cells. Cancer stem cells (CSCs), which are also known as tumor-initiating cells are also linked to metastasis. The glucose functionalized MSNs specifically deliver the notch signaling inhibitors to CSCs because the breast CSCs show enhanced glucose uptake as compared to normal breast cancer cells. *In vitro* and *in vivo* trials on chick embryo showed that glucose functionalized nanoparticles target and reduce the CSC pool and suppress the tumor growth.

The condition of certain tumor cells such as acidified environment and secretion of certain enzymes at the tumor site provides an opportunity to design pH and enzyme responsive drug carriers by conjugating them with relevant stimuli-responsive materials. For instance, Xia and group [134] produced MSNs carrying anticancer drug doxorubicin (DOX) inside their pores, then the outer surface was conjugated by cellulose through an EDC/NHS (1-ethyl-3-(3-dimethylaminopropyl)carbodiimide/N-hydroxysuccinimide) coupling reaction. The cellulose modified surface of MSNs controlled the drug release because of its cationic characteristics. Therefore, the loaded anticancer drug DOX was released by cellular internalization responses using cellulase glycosidase enzyme and pH triggers. The surface-coated cellulose breaks into small glucose units or cello-dextrin units by cellulase enzyme. This process helps to open the sealed pores of MSNs while the ester linkage breaks by acid catalyzed hydrolysis and the anticancer drug (DOX) is released.

The conjugation of specific sugar molecules such as glucose to drug-loaded silica nanoparticles increases the solubility and target selectivity of the therapeutic drug. For instance, John et al. [135] conjugated glucose to MSNs as an affinity ligand to deliver an anticancer drug, celastrol to cancer cells. They have conjugated sugar with MSNs with two different anchor molecules and CDI as a linking agent. Hyperbranched poly (ethylene imine) (PEI) anchored MSNs increases the cellular uptake relative to APTES anchored MSNs. This is because of the overall positive surface charge of the PEI layer, which increases the reaction sites for sugar conjugation. The analysis of cell uptake in HeLa and A549 type cancer cells showed that glucose coated celastrol loaded MSNs showed high specificity to cancer cells and minimal off-target effects in healthy cells when compared to mouse embryonic fibroblast as a representative for healthy cells. Various carbohydrate

functionalized mesoporous silica nanoparticles and their biological applications can be found in Table 2.2.

Table 2.2: Carbohydrate functionalized silica nanoparticles and their respective bioapplications.

Sugar-coated	Sugar-Structure	Biological application	Ref
Glucose		Increases binding affinity and specificity of therapeutic molecule. Helped in study interactions with cell-surface receptors. Improved drug uptake into tumor cells.	[133],[135], [136],[137]
Galactose		To study carbohydrate lectin interactions, carbohydrate-carbohydrate interaction.	[138],[139], [140]
Fructose		To study glycan-lectin interactions	[141]
Lactose		Targeted drug delivery in prostate cancer	[132],[128]
Arabinose		Specifically targeted to mycobacterium	[130]
Mannose		To study carbohydrate-lectin interactions	[138, 140]
Trehalose		Targeted drug delivery to treat tuberculosis, which is caused by mycobacteria	[131]
Fucose		To study lectin-glycan interactions	[142]
GlcNAc and GalNAc		To study lectin-glycan interactions	[142]

From the literature, it is evident that glycan-protein interactions play a crucial role in disease development and progression. Therefore, a wide variety of glyconanoparticles are used to study these interactions as well as for targeted drug delivery as glycans can specifically interact with receptors of choice. However, research focused on the usage of glycan conjugated silica nanoparticles for biological applications is still developing. In this regard, conjugation of various types of carbohydrate molecules with silica nanoparticles and the study of their interaction in simple bacteria such as *E.Coli* and *B.Subtilis* has a lot of interest.

2.7 Conclusion

The study of multiple biological processes simultaneously is crucial in biomedicine. In this context, sugar-coated dye-doped MSNs have excellent potential. They are highly regarded tools in biological research because of their high biocompatibility and low-toxicity. Fluorescent probes encapsulated into the highly stable silica matrix, exhibit improved stability and sensitivity in physiological conditions and enhance the emission spectrum. Moreover, MSNs are optically transparent, highly hydrophilic, and size-tunable. In addition to this, the sugar coating on the surface of the MSNs can improve targeted delivery of the nanoparticle.

Even though MSNs have wide scope in imaging and targeted drug delivery, some limitations inhibit their applications in biomedicine. Firstly, dye leakage under physiological conditions could reduce their fluorescence intensity over time and increase the background signal. This requires further investigation. Secondly, the control over the non-specific binding during the targeted drug delivery is not yet fully attained. Thirdly, control over their functionality and hydrodynamic size are pivotal which needs standardization of synthesis procedures because the hydrodynamic size for physiological applications is ≤ 100 nm. Nanoparticles with theranostic properties are important, as they can image and treat the targeted site simultaneously. However, until now only one silica nanoparticle-based drug, Cornell dots (c-dots) have reached the clinical trials phase. This is a fluorescent mesoporous silica nanoparticle invented by Ulrich B. Wiesner in the late 1990s. Ultra-small c-dots (10 nm), can reach the tumor sites and illuminate them and weaken the tumor by releasing the therapeutic drug. This invention revealed that silica nanoparticles have significant potential in various clinical applications in the near future.

Chapter 3

Synthesis and characterization of dye-doped amine modified mesoporous silica nanoparticles

This chapter comprises the details of synthesis methods and methodologies of dye-doped AMSNs and discusses the results of dye-doped AMSNs as well as the effect of reagent concentrations on the surface properties of MB AMSNs.

3.1 Introduction

Mesoporous silica nanoparticles (MSNs) usually have high surface area (400-1000 m²/g), high thermal and chemical stability, hydrophilicity, and a surface enriched with silanol groups. These features make MSNs applicable for a wide range of applications such as catalysis, adsorption, adhesives, and in biomedicine [[143], [144], [145], [146]]. Studies have shown that MSNs are highly biocompatible and biodegradable. Further, silica is accepted in the “Generally Recognized As Safe” category by the US Food and Drug Administration (FDA). As a result, it is widely used in cosmetics, food, and drug industries [147]. Modification of surface silanol groups enhances its scope of application in biology.

Among various applications, bio-imaging using MSNs has received significant attention. So far, a wide variety of dye molecules including FITC (fluorescein isothiocyanate) and RITC (rhodamine isothiocyanate) have for encapsulated into the silica matrix. These dye molecules can form an adduct with APTES (3-aminopropyltriethoxy silane) through their chemically reactive isothiocyanate group. However, these fluorophores are quite expensive. Conventional dyes such as rhodamine B (RB), fluorescein, and methylene blue (MB) dyes show high fluorescence intensity, are widely available and relatively cheap. The structure and absorption spectra of each are shown in Fig 3.1. Therefore, these dyes were chosen for encapsulating into the silica matrix.

Conventionally, two chemical approaches were available for dye encapsulation into silica nanoparticles. The first approach consists of using covalent bonding of dye molecule with silica matrix and the second approach has been described as a non-covalent approach. It is obvious that the best method for the dye encapsulation is covalent approach, but it requires certain functional groups to react with silicate precursor which needs special preparation of dye molecules. Consequently, non-covalent approach is the promising way that can employ for any type of dye and exhibits a low-cost method. Therefore, a methodology was developed for simultaneous dye doping via non-covalent approach into MSNs and introducing amine functionality on the surface [149]. The dye molecules can trap inside the mesopores due to the interaction with negatively charged silanol groups of the silica matrix. Previously, rhodamine B has been doped into a silica matrix by a multi-step synthesis through covalent approach [148]. In this study, a synthesis approach was developed for the entrapment of RB into the silica matrix by covalent attachment in a one-pot synthesis. Furthermore, the more hazardous chloroform solvent typically used was replaced with less harmful alcohol for the dye-APTES adduct formation.

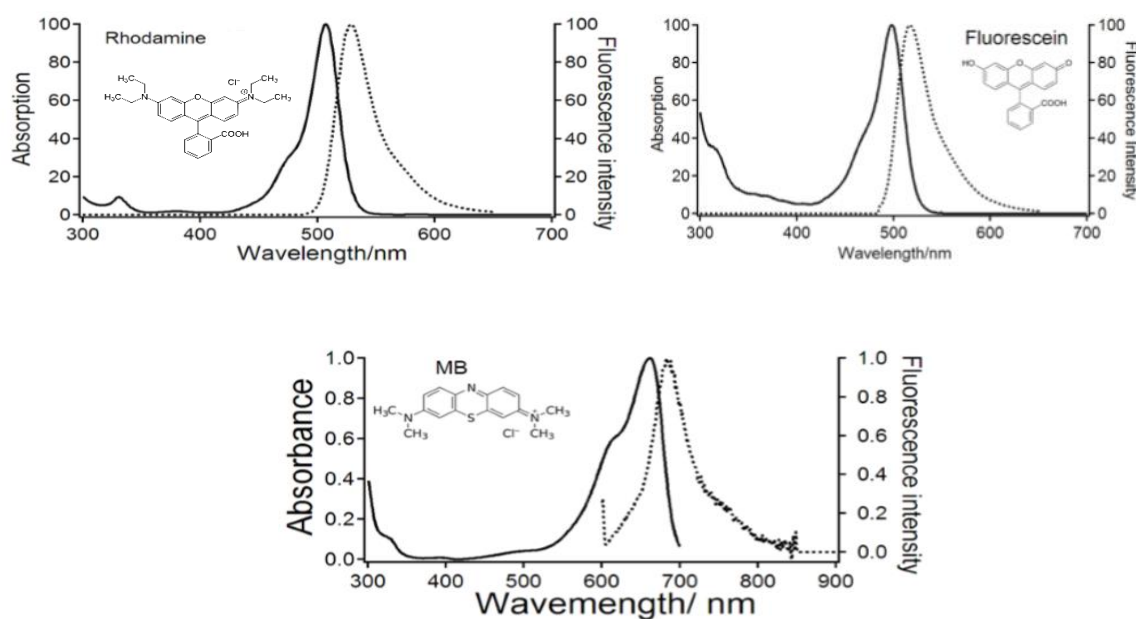


Figure 3.1: Structure and absorption (solid line) and fluorescence (dotted line) spectra of rhodamine B, fluorescein, and methylene blue, respectively (Reproduced from google images).

3.2 Experimental details

3.2.1 Details of the reagents

Tetraethyl orthosilicate (TEOS) (Sigma-Aldrich, 78-10-4, 98%), Cetrimonium bromide (CTAB) (Sigma-Aldrich, 57-09-0, $\geq 99\%$), 3-aminopropyl triethoxysilane (APTES) (Sigma-Aldrich, 919-30-2, $\geq 98\%$), Rhodamine B (RB) (Sigma-Aldrich, 81-88-9, $\geq 95\%$), Fluorescein (free acid) (Sigma-Aldrich, 2321-07-5, 95%), Methylene Blue (MB) (Sigma-Aldrich, 122965-43-9, $\geq 97\%$), and Ammonium Hydroxide (NH_4OH) 25% w/v were used as received. Absolute ethanol (Ajax Fine Chem, 99.5%) and Millipore filtered deionized water was used throughout the experimental work.

3.2.2 Characterization techniques

JEOL-JCM-6000 scanning electron microscopy (SEM) was used to measure particle size and shape. Nanoparticle surface area and porosity were measured with Micromeritics Tristar II Surface area and Porosity analyzer. X-ray diffraction (XRD) measurements were recorded with EMMA (Enhanced Multi Materials Analyser). Ninhydrin assay and PerkinElmer Attenuated Total Reflectance Fourier Transform Infrared (ATR-FTIR) was used for functional group analysis and characterization. PerkinElmer Lambda 650 UV-Vis spectrometer was utilized to measure the absorbance of the solid compounds. UV-lamp was used to check the fluorescence, and liquid-state ultraviolet-visible spectra were recorded on HP 8453 UV-Vis.

3.2.3 Experimental procedures

Mesoporous silica nanoparticles (MSNs)

Mesoporous silica nanoparticles were synthesized by slightly modifying the procedure developed by Venkatathri et al. [150]. In a typical process, 0.4 ml of NH_4OH (25% w/v) was added to 6.3 mM (0.27 g in 117 ml D. H_2O) CTAB solution. After 30 min, 1.1 ml of TEOS was added dropwise (0.3 ml/min) and maintained at 70 °C for two hours, with constant stirring at 700 rpm to produce the nanoparticles. The resulting synthesis mixture had a molar ratio of 1 TEOS: 0.15 CTAB: 1.1 NH_4OH : 1300 H_2O . The nanoparticles were separated from the reaction medium by centrifugation at 10000 rpm for 10 min, washed with deionized water then ethanol and dried under vacuum.

The structural directing agent CTAB was removed by dispersing the resultant nanoparticles into acidic ethanol (1 g / 10 ml) at 60 °C overnight.

Amine-modified mesoporous silica nanoparticles (AMSNs)

Amine-modified MSNs (AMSNs) were synthesized in a single step using the co-condensation technique according to the procedure reported by Jayawardhana et al. [130]. In brief, a mixture of 1 ml TEOS, and 0.26 ml APTES was added to an aqueous CTAB solution (6.4 mM, 0.246 g in 105.3 ml of D.H₂O) at R.T. Then 0.94 ml of NH₄OH (25% w/v) was added to initiate the hydrolysis and condensation reactions. The reaction mixture had a molar ratio of 1 TEOS: 0.25 APTES: 0.15 CTAB: 3 NH₄OH: 1300 D.H₂O. After maintaining stirring at 700 rpm for 5 hrs at R.T., the mixture was centrifuged (10000 rpm, 10 min) and the resultant nanoparticles washed with deionized water and then ethanol. The surfactant, CTAB was removed by extracting it into acidic ethanol for 12 hrs at 60 °C. The nanoparticles were dried under vacuum at 40 °C.

Synthesis of RB-APTES adduct

RB-APTES adduct was synthesized by employing the following method. In a typical procedure, one mmol of RB was dissolved in the 10 ml of ethanol. One mmol of APTES was added at 40 °C and stirred for 4 hrs. The molar ratio obtained was 1: 1 for RB and APTES respectively. The solvent was removed by rotavapor under vacuum at 60 °C. Bright red crystals were obtained.

MB-APTES and fluorescein-APTES adducts could not be formed since they have no reactive amine groups present.

Synthesis of the dye-doped amine grafted mesoporous silica nanoparticles (Dye-AMSN)

For producing the dye-doped amine grafted MSNs (dye-AMSNs), two types of protocols were used. One was dye incorporation into the silica matrix by covalent attachment, and the second was physical entrapment of dye molecules into the mesopores. Rhodamine B (RB) was encapsulated by employing both of these two protocols, but fluorescein and methylene blue were doped via physical entrapment only.

Encapsulation of dye into AMSNs by covalent attachment

Rhodamine B was employed for the covalent encapsulation because of the availability of the amine reactive carboxylic group.

RB-AMSNs were synthesized by slightly modifying the multi-stage procedure into a single step [148]. In a typical synthesis process, 0.3 ml APTES, was added to 0.1 mmol RB in 58.3 ml ethanol at 40 °C and maintained for 4 hrs. To this reaction mixture, was added 0.1 M aqueous CTAB (0.9 g in 25.2 ml D.H₂O). This was followed by the addition of 1.1 ml TEOS, and 0.75 ml NH₄OH (25% w/v). The molar ratio obtained was 1 TEOS: 0.25 APTES: 0.5 CTAB: 1 NH₄OH: 144 D.H₂O: 50 EtOH. The reaction was stirred at 800 rpm for 15 hrs. The mixture was then centrifuged and washed with copious deionized water and then ethanol. The pore-generating agent, CTAB, was removed by acidic ethanol treatment.

Non-covalent encapsulation of dye molecules into AMSNs

RB, fluorescein, and methylene blue (MB) were employed to synthesize dye-doped AMSNs through the non-covalent approach.

In a typical process, dye-doped MSNs were synthesized based on the protocol reported for preparing MSNs doped with inert dyes [151]. In general, 0.01 mmol dye was added to 30 ml of ethanol. After complete dissolution, CTAB aqueous solution (1.8 g in 25.2 ml of D.H₂O) was added. Then 0.75 ml of NH₄OH (25% w/v), 2.2 ml of TEOS were added and allowed to stir for 2 hrs. Then 0.592 ml of APTES was added and allowed for stirring at R.T for 18 hrs. The molar ratio of reagents obtained as 1 TEOS: 0.25 APTES: 0.5 CTAB: 1 NH₄OH: 144 H₂O: 50 EtOH. The obtained nanoparticles were centrifuged and washed several times with water and then ethanol for the complete removal of excess dye molecules. The surfactant was removed by extraction with acidic ethanol solution at 60 °C for 12 hrs.

Dye-leakage studies

The leakage of dye molecules from the dye-doped AMSNs was performed by dispersing the nanoparticles into an aqueous solution containing 10: 1 ratio of D.H₂O and ethanol.

In general, one milligram of each dye-doped AMSN sample was taken into a McCartney tube containing 2 ml of D.H₂O-ethanol mixture. Then the samples were incubated at 37 °C for 2 hrs

on an orbital shaker at 200 rpm. The nanoparticles were separated by centrifuging at 10000 rpm for 5 min. UV absorbance of supernatant was measured.

Ninhydrin assay for the determination of the degree of amine grafting

The ninhydrin assay was employed for the determination of the number of amine molecules grafted on to the surface of MSNs.

A stock solution, was prepared by dissolving the 0.1 ml of APTES in 10 ml of ethanol, making a 0.0426 M solution. From the stock solution, 0.1, 0.2, 0.4, 0.8, 1.6, and 3.2ml were taken to react with ninhydrin reagent. 10.4 mg of AMSN and 13 mg of MB-AMSN samples were taken for the determination of the number of amine groups coupled on the silica surface.

In a typical assay procedure, the amine-containing compounds were added to a test tube containing one ml of acetate buffer, pH 5.5, (0.77 g CH_3COONa , 0.178 g CH_3COOH in 100 ml $\text{D.H}_2\text{O}$) and 2 ml of 3% ninhydrin agent (3 g in 100 ml $\text{D.H}_2\text{O}$). The resulting mixture was heated for 15 min over a steam bath. The colour of the solution changed to blue-purple. Then the test tubes were cooled to R.T., in a cold-water bath. 7 ml of ethanol was added to each test tube, and the resultant solution was centrifuged at 7000 rpm for 7 min. The absorbance of the supernatant was measured at 570 nm on HP 8453 UV-Vis spectrometer. A standard curve was prepared from the absorbance values. The concentration of the amine compound in the samples was determined from the standard curve.

3.3 Results and discussion

Dye encapsulation into the amine modified mesoporous silica matrix can be employed via two mechanisms. Chemical binding through covalent attachment (Fig 3.2A) and physical adsorption by electrostatic interactions (Fig 3.2B) [[102], [152], [153], [154]]. However, in most cases, covalent attachment is preferred because it can reduce the dye leakage and hence increase the photostability of the dye molecule.

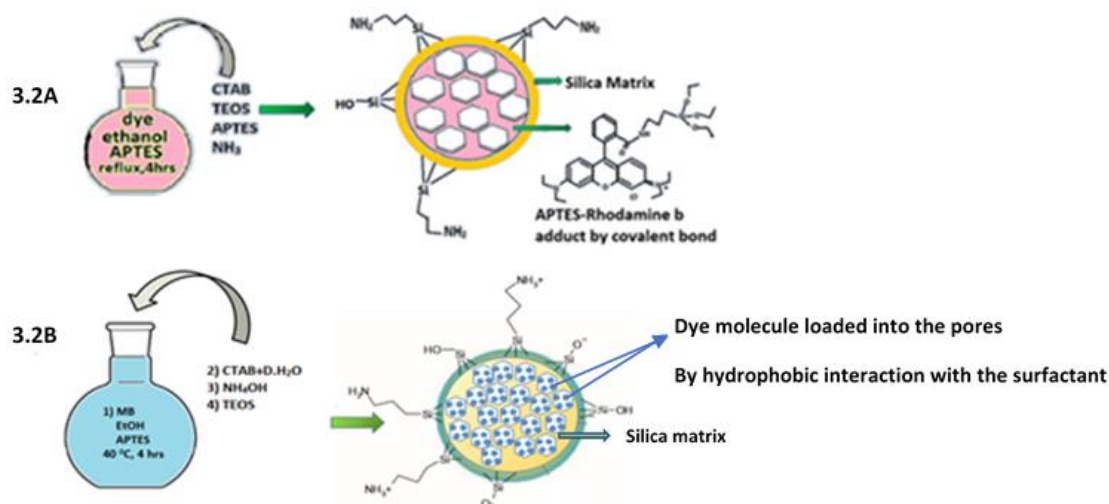
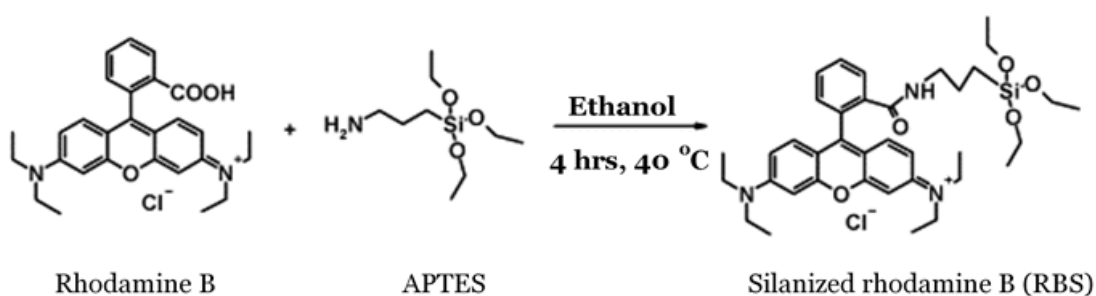


Figure 3.2: Diagrammatic illustration of (A) covalently attached RB and (B) physically entrapped MB.

Covalent attachment is achieved via synthesis of dye-APTES adducts using dyes with highly reactive groups such as isothiocyanates. For example, rhodamine isothiocyanate (RITC) has been used for making adduct with APTES. However, there is only one article [154] reporting the synthesis of RB-APTES adduct (RBS) with, in the presence of chloroform (CHCl₃) solvent. The reaction between the carboxylic acid group of rhodamine with amines has been mentioned in the literature [[155], [156]]. Therefore, we slightly modified the synthesis process of RBS by replacing the more hazardous CHCl₃ with ethanol (Scheme 3.1) and proceeded to the next stage (i.e., the formation of silica matrix) without isolation of RBS at this stage.



Scheme 3.1: Protocol for the synthesis of Rhodamine-APTES adduct (RBS)

The progress of the formation of RBS was monitored by TLC (Fig 3.3A). Usually, acid compounds show a tailing effect on silica gel TLC. This effect occurs because of hydrogen bond formation

between carboxylate and Si-OH of silica. The absence of this tail is due to the conversion of the carboxylic group to the amide. RBS formation was further confirmed by FT-IR (Fig 3.3B). The vibration of the C=O bond of RB was observed at 1680 cm^{-1} . After the condensation reaction with APTES, the C=O bond vibration shifted to 1758 cm^{-1} , which indicated the conversion of the carboxylic acid group in RB to an amide group in RBS. Peaks at 1007 cm^{-1} and 1106 cm^{-1} came from APTES, assigned to Si-OEt vibrations.

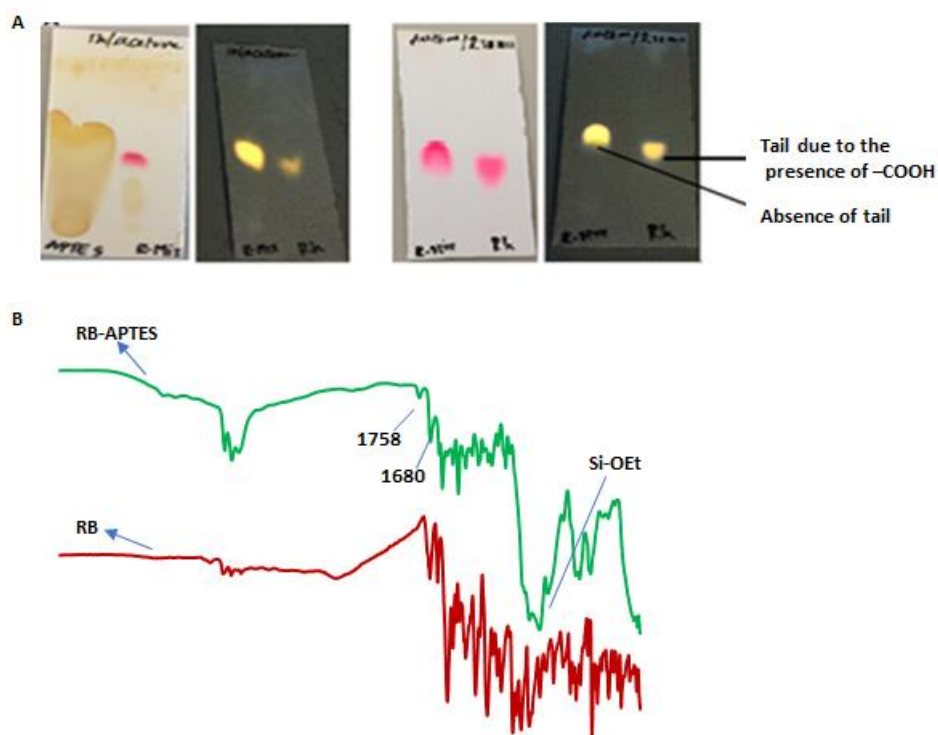


Figure 3.3: (A) Progress of reaction monitored by TLC after 1 hr and 2:30 hrs (under normal light and UV lamp), (B) FT-IR spectra of RB and RBS.

On the other hand, in the non-covalent approach, dye molecules were doped into the pores by electrostatic interaction with surfactant molecules. After the removal of surfactant, dye molecules reside inside the mesopores due to the interaction of the positively charged dye with negatively charged silanol groups which were present on the surface (Fig 3.2B).

The co-condensation method was modified slightly for simultaneous dye encapsulation and amine surface grafting. This technique is also termed direct synthesis or single-pot synthesis, in which

condensable organosilane of the type R-Si (OR')₃ is added to the reaction mixture during the formation of MSNs (Fig 3.4).

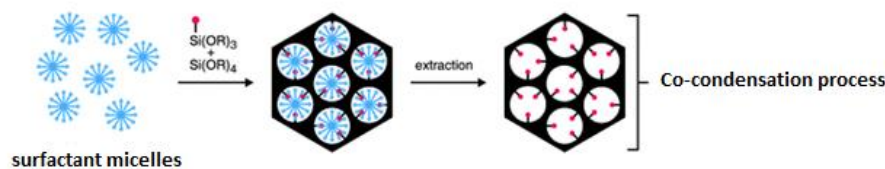
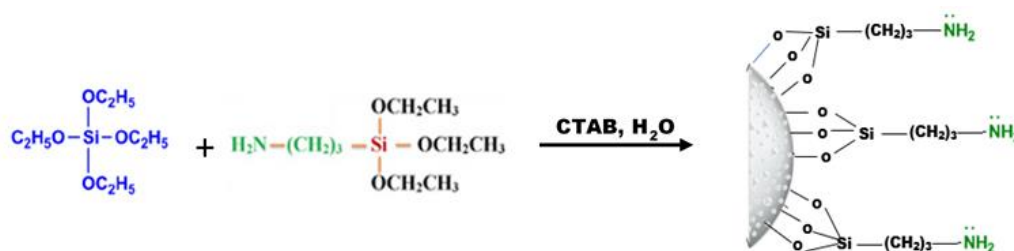


Figure 3.4: Diagrammatic representation of the co-condensation method (Reproduced from Bruhwiler et al., 2010) [157].

An organic alkoxy silane, 3-aminopropyltriethoxysilane (APTES) was used for amine surface grafting (Scheme 3.2). This reagent is generally used for amine modification of MSNs because it forms strong covalent linkages with the surface silanol groups. The amine functional group is highly desirable for further coupling of selected bioactive molecules.

However, the addition of organo-alkoxy silanes during the MSNs synthesis process has a significant effect on the particle morphology and pore ordering [[158], [159]]. The distribution of functional groups in the final product is mostly homogeneous, but the high functionalization degree may lead to disordered mesopores. The structural directing agent was removed by extraction as calcination may affect the porous morphology of the MSNs.



Scheme 3.2: Schematic illustration of the synthesis of amine-modified MSNs (AMSN) by co-condensation method.

3.3.1 Physicochemical characterization of MSNs and AMSNs

The morphological and surface characteristics of MSNs and amine-modified MSNs (AMSN) were investigated by JEOL-JCM-6000 SEM, which operated at 15 kV and the surface properties, N₂ sorption measurements were measured by Micromeritics Tristar II at liquid N₂ temperature (~ 77 K). The samples were weighed and degassed at 323 K for 18 hrs on a Micromeritics VacPrep 061 sample degas system.

Surface properties of MSNs and AMSN

The surface area and mesoporous nature of MSNs and AMSNs characterized by N₂ sorption analysis and XRD measurements. The sorption curves revealed type-IV adsorption-desorption isotherms, indicating the presence of mesopores according to the specifications of IUPAC nomenclature[160]. The isotherm curves showed the same behavior to $p/p_0 = 0.4$. From then onwards, there was a slight difference between the isotherms obtained with two different concentrations of CTAB. This indicated a difference in pore distributions. Both isotherms showed a bimodal pore distribution (Fig 3.5).

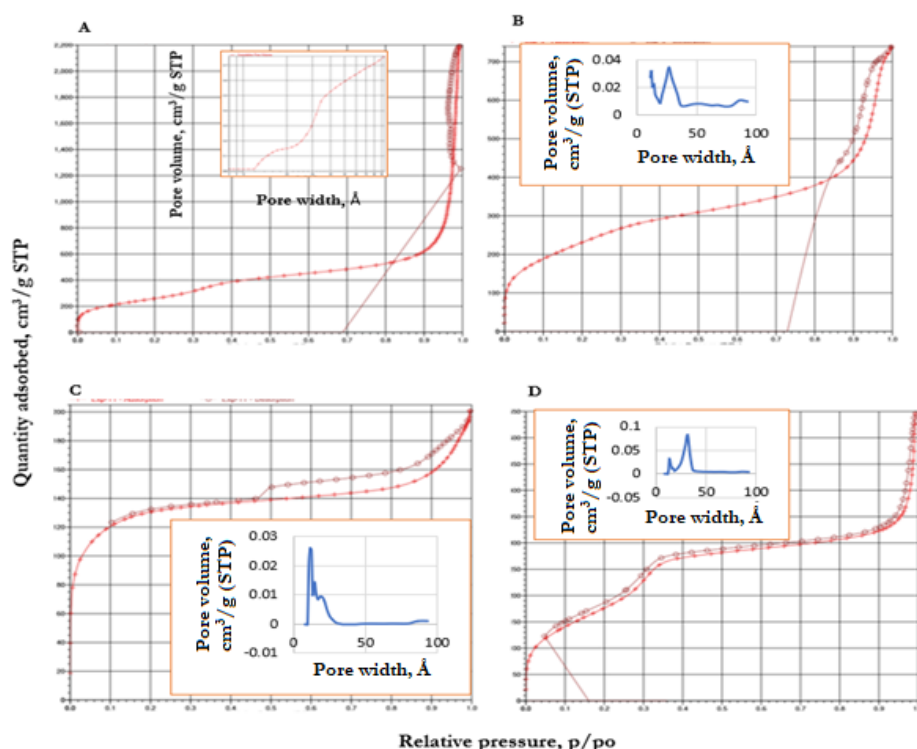


Figure 3.5: N₂ sorption isotherms and corresponding pore size distributions (inset) of MSNs synthesized at CTAB molar ratio of (A) 0.075, (B) 0.15, (C) 0.3, and (D) Amine modified MSN.

The BET surface analysis showed the particle surface area varied from 994 to 417 m²/g for MSNs according to the surfactant molar ratio. The effect of surface area at different CTAB molar ratios was studied during this analysis (Table 3.1). Results obtained for sample 2 & 3, showed good agreements with previously reported studies [161]. The surface area of the nanoparticle decreased with increase in the CTAB concentration because the nanoparticles might be agglomerated due to the variation in the hydrolysis and micellization of CTAB. In addition to this, the increased surfactant concentration resulted in increase in average particle size, disordered structure, pore size, and pore volume. There was a slight difference in the BET results for AMSNs from MSNs synthesized at same CTAB molar ratios. The decrease in the surface area of AMSNs may be due to the presence of amine functionality on the surface. These amine groups may form weak hydrogen bonding with adjacent silanol groups. On the other hand, CTAB concentration below CMC resulted the macro-porous material (Table 3.1 (Num 1)).

Table 3.1: Physical characteristics of MSNs and AMSNs synthesized at different CTAB concentrations.

Num	Type of Sample	CTAB/TEOS	Avg Size of NP from BET (nm)	Avg crystallite size from XRD (Å)	S _{BET} (m ² /g)	Total pore volume (cm ³ /g)	BJH Avg pore diameter (nm)
1	MSN	0.075: 1	6.03	-	994.3	2.1	69
2	MSN	0.15: 1	7.03	10.8	852.48	1.11	25.8
3	MSN	0.3: 1	14.38	-	417.2	0.31	6.5
4	AMSN	0.15: 1	8.21	10.6	730.2	0.98	4.6

XRD was performed on EMMA diffractometer. The typical wide-angle XRD diagram of the MSNs and AMSN showed a broad peak at $2\theta = 23.7$, is the characteristic peak for silica nanoparticles. The XRD pattern obtained confirmed the formation of silica nanoparticles when compared with existing data for MCM-41 material [162]. The broad pattern of the peak revealed

the amorphous nature of the nanoparticles (Fig 3.6). However, a narrow peak at $2\theta = 37.5$ resulted due to the minute crystalline nature of the sample. The average crystallite size was calculated by using the Debey-Scherrer equation (Eq 1).

$$D = K\lambda/(d \cos\theta) \quad (\text{Eq 1})$$

D is the crystallite size, λ is the wavelength which is 1.54060 \AA for Cu- $k\alpha$, K is the crystallite shape factor (~ 0.9), d is the full width at half maximum (FWHM) of the XRD peak, and θ is the angle (calculated from angle of diffraction, 2θ). FWHM is a crucial factor to measure the crystallite size. This value was measured by using OriginPro software. The obtained crystallite sizes are tabulated in Table 3.1.

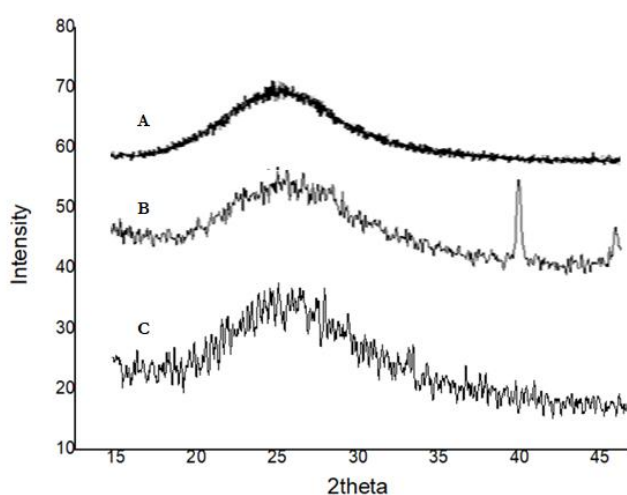


Figure 3.6: XRD diffractograms of (A) MCM-41 (reproduced from J.S.Beck et al., 1992), (B) MSN and (C) AMSNs

Chemical Characterization of MSNs and AMSNs

FT-IR spectral analysis studied were performed to identify the functional groups in the sample (Fig 3.7). The intense peak at 1051 cm^{-1} corresponds to the asymmetric stretching vibrations of Si-O-Si and the peak at 800 cm^{-1} is due to the symmetric stretching vibration of Si-O-Si. The broadband at $3300\text{-}3400 \text{ cm}^{-1}$ and $1620\text{-}1640 \text{ cm}^{-1}$ arise from stretching and bending vibrations of aliphatic amine (N-H) groups, respectively in the amine-modified MSNs.

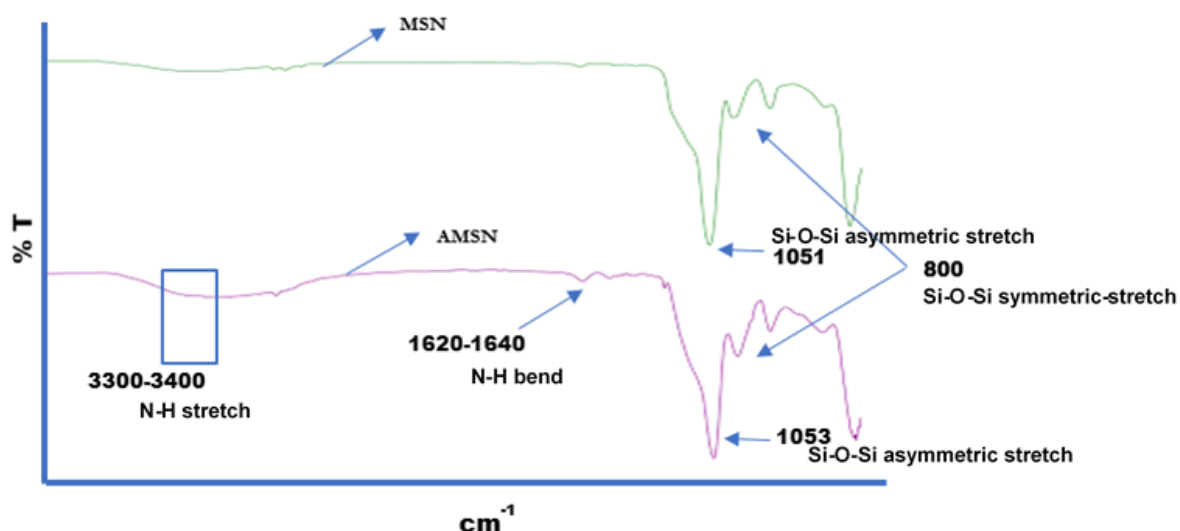
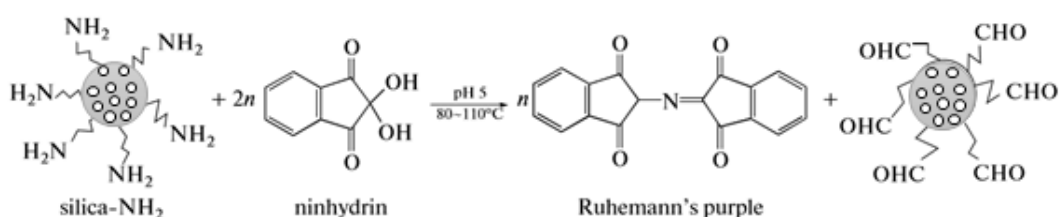


Figure 3.7: FT-IR spectral patterns of (A) MSN and (B) AMSN.

Determination of amine surface grafting by ninhydrin assay

The surface functionalized amines were quantified by ninhydrin assay. Ninhydrin is widely used for the detection of primary amine groups in biochemistry [163]. Therefore, ninhydrin reagent was used to determine the degree of amine grafting on MSNs as well as dye-doped MSNs [164]. ninhydrin reagent reacts with primary amine groups on the surface of AMSNs to form Ruhemann's purple (Scheme 3.3).



Scheme 3.3: Formation of Ruhemann's purple by the reaction of amine-modified MSN with ninhydrin reagent (Reproduced from Hsu et al., 2013).

The amount of APTES grafted on the surface of the AMSNs was calculated from Eq 2. A standard curve was drawn (Fig 3.8) to determine the unknown concentration. The number of moles of

amine grafting on AMSNs was calculated to be 2.91 mmol/g. The surface density of amine groups was calculated by Eq 3.

$$\text{Molar quantity of grafted amine} = M/W_s \text{ (mol/g)} \quad \text{Eq 2.}$$

$$\text{Number of molecules} = (\text{Eq 2}/S_{\text{BET}}) \times 6.023 \times 10^5 \text{ (molecule/nm}^2\text{)} \quad \text{Eq 3}$$

where M = The molarity obtained when compared with the standard curve

W_s = The amount of sample taken for analysis (g).

S_{BET} = The specific surface area (nm²/g).

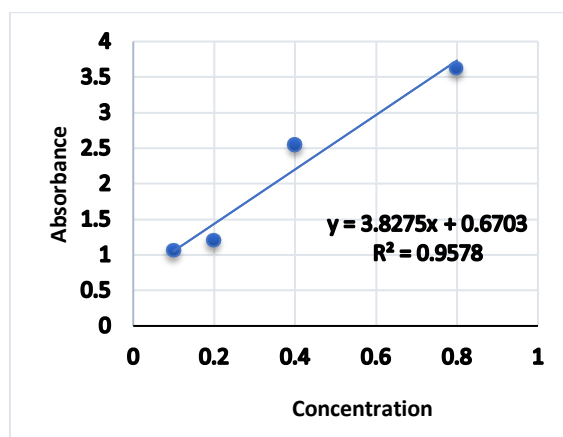


Figure 3.8: Ninhydrin assay standard curve

3.3.2 Physiochemical characterization of dye-doped AMSNs

The physical characteristics including size, morphology, and porosity were studied for all three types of dye-doped AMSNs and covalently incorporated RB-AMSNs.

Structure, size, and morphology of the particles characterized by SEM, BET, and XRD. JEOL-JCM-6000 Scanning electron microscopy (SEM) operated at 5 kV and 10 kV was used to measure the size and shape of the nanoparticle.

For SEM studies, a small amount of sample was dispersed on to the carbon tab, then covered with a 12 nm gold layer. The results showed that the nanoparticles were roughly spherical, smooth, and monodispersed (Fig 3.9). No significant change was observed in the size of the particles doped with different types of dyes. The average size of the particle ranged from 300-350 nm observed for MB and fluorescein doped AMSNs whereas, RB doped AMSNs were in the range of 350 – 400 nm. The exact size of the nanoparticle could not be determined.

In SEM, when the specimen was bombard with electrons (negatively charged particles), some of them get reflected (backscattered), some of them create secondary electrons, but some passed through the specimen and impart a negative charge. In silica nanoparticles, the surface silanol groups are negatively charged. Therefore, when the negatively charged electron beam reaches the negatively charged silica surface, they are repelled by each other and the beam of electrons change their trajectories resulting in blurred image.

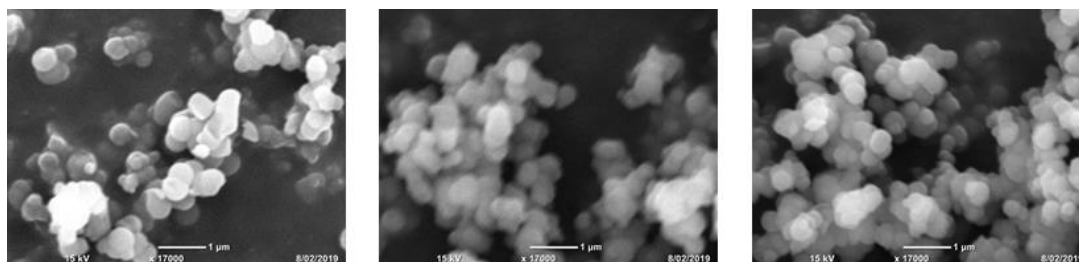


Figure 3.9: SEM images of RB, fluorescein, and MB doped AMSNs, respectively.

The surface area and porosity results revealed type IV isotherms for all three samples. This indicated that the obtained dye-doped AMSNs were mesoporous materials.

The XRD diffractograms for all three types of dye-doped AMSNs showed the same pattern with broad curves with 2θ at around 23.7, indicating the three samples have amorphous nature (Fig 3.10).

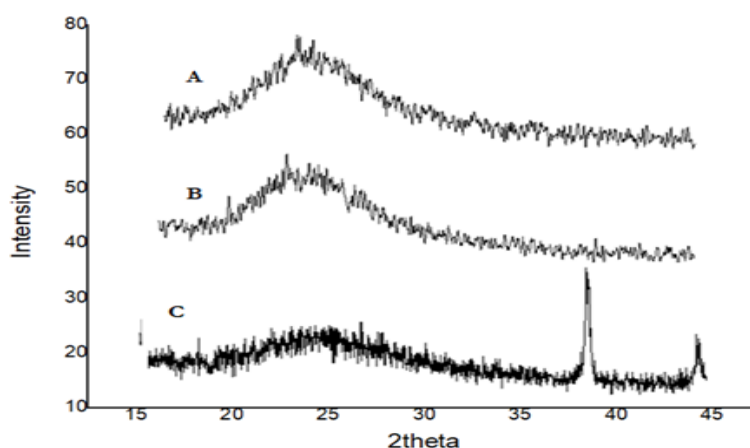


Figure 3.10: X-ray diffractograms of (A) RB- AMNS, (B) Fluorescein AMSN, and (C) MB-AMSN respectively

FT-IR was used to determine the amine functionality on the surface (Fig 3.11). The intense peaks observed at 110- 450 cm^{-1} are the characteristic peaks for the silica nanoparticles and the small peaks appeared at 1615-1620 cm^{-1} resulted from the N-H bending. Therefore, the FT-IR spectra confirms the presence of amine group on the surface.

The amine surface grafting was further confirmed by ninhydrin assay for MB-AMSN. This coloured reaction is the characteristic for reaction of primary amines with ninhydrin. The assay resulted in a blue-purple coloured solution after reaction with ninhydrin. The amount of amine grafted was measured by the previously mentioned equation (Sec 3.3.1). The result indicated the presence of one molecule on each square nanometer.

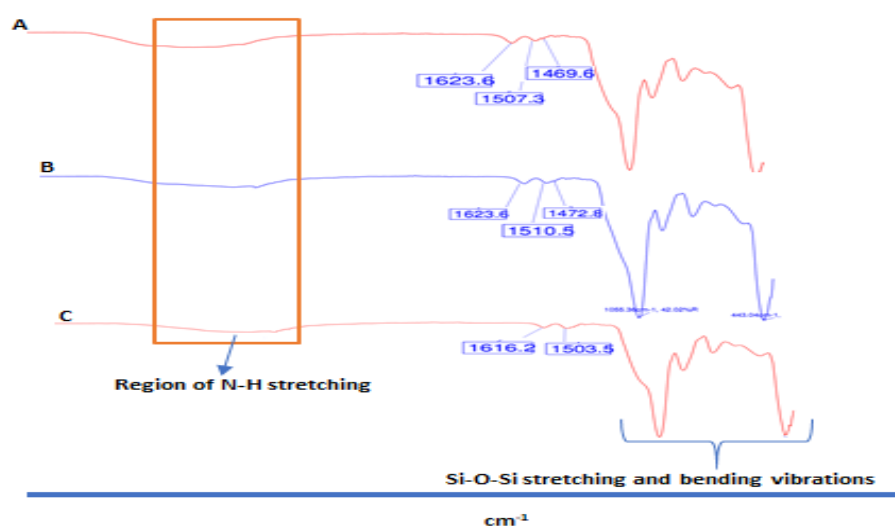


Figure 3.11: FT-IR spectra of (A) RB-AMSN, (B) Fluorescein AMSN, and (C) MB-AMSN

The fluorescence of the dye-doped nanoparticles was observed by illuminating the samples under UV light (fig 3.12 A). All three samples showed fluorescence in the presence of UV light. Similarly, the nanoparticles dispersed into ethanol solvent also resulted in bright fluorescence under UV light (Fig 3.12 B).

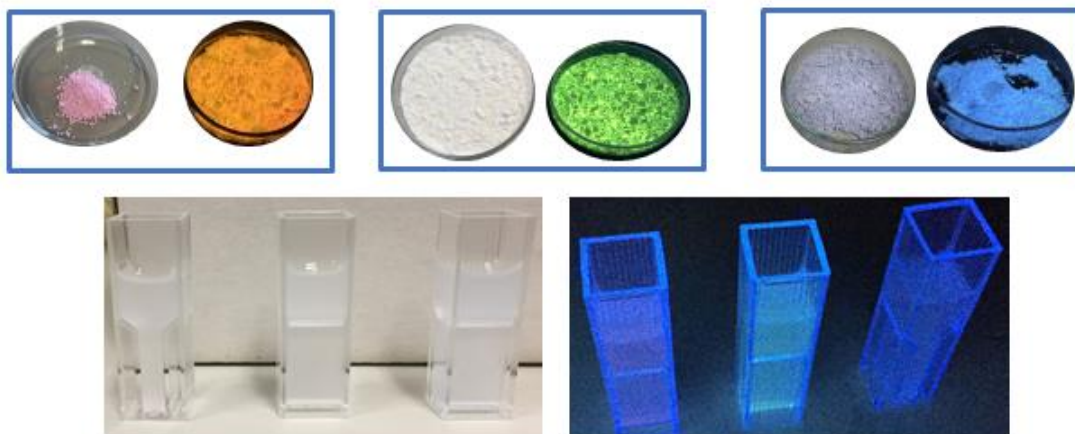


Figure 3.12: The fluorescence of the RB, fluorescein, and MB doped AMSNs under normal light and UV lamp in solid and dispersion state respectively.

The solid-state UV-Vis spectral studies revealed absorption values around 562 nm, 484 nm and 634 nm for RB-doped AMSNs, fluorescein doped AMSN and MB-doped AMSNs, respectively (Fig 3.13). These spectral values are equal to the absorption frequency values of the naked dyes which suggested the successful doping of dye molecules.

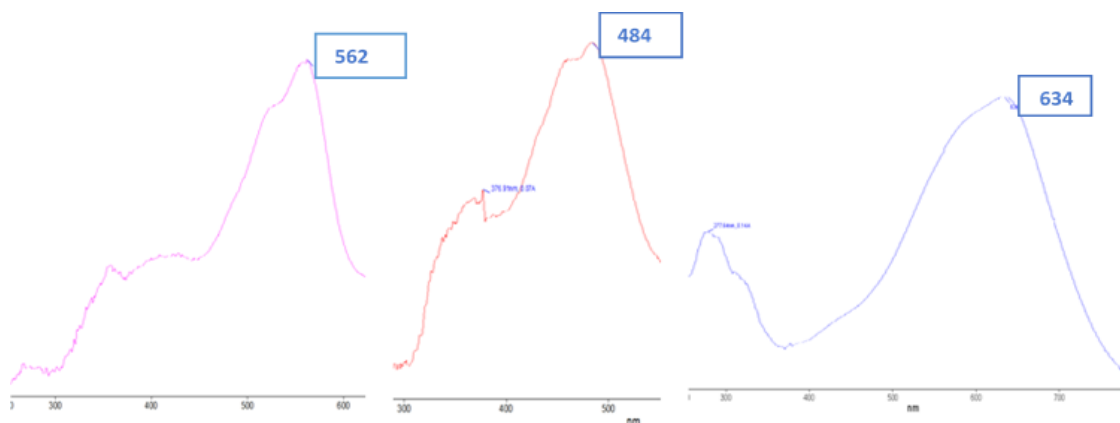


Figure 3.13: Solid-state UV-Vis spectra for RB, fluorescein, and MB doped AMSNs, respectively.

Dye-leakage studies

The leakage of dye molecules from the dye-doped MSNs in aqueous solution (9:1, D.H₂O and ethanol) was investigated by measuring the UV absorbance value. No significant amount of dye leakage was observed even after 30 min of nanoparticles dispersion in D.H₂O. Furthermore, the

dye-doped nanoparticles exhibited bright fluorescence under UV light. However, dye leakage studies under various pH conditions are still required to confirm the stability of the dye within the nanoparticle matrix.

Characteristic results of chemically bonded RB AMSNs and comparison with non-covalently doped RB AMSNs

Rhodamine B (RB) dye was entrapped into the MSN matrix by covalent attachment as well as via the non-covalent approach. Both approaches resulted in smooth spherical and monodispersed particles with ordered mesopores. The diameter of the nanoparticles was around 450 nm in SEM (Fig 3.14).

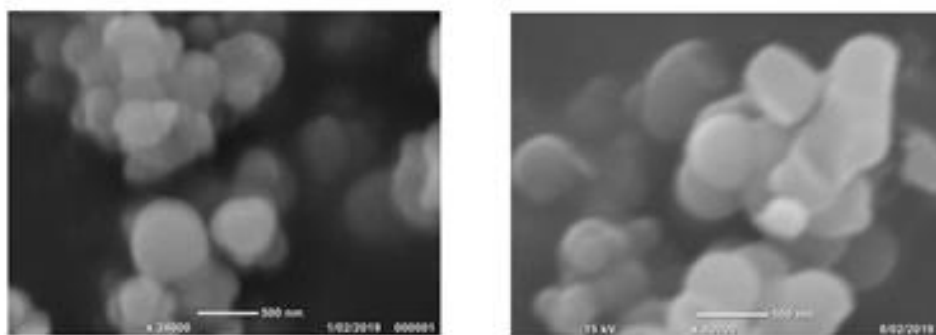


Figure 3.14: SEM of (left) covalently encapsulated RB doped AMSNs, (right) physical entrapped RB doped AMSNs.

However, a slight difference was observed in the FT-IR spectra (Fig 3.15A). Both spectra showed the peaks corresponding to Si-O-Si stretch and bending frequencies at 400-1050 cm^{-1} . The intensity of the broad peak at 3300-3500 was higher in RB MSNs prepared by the non-covalent approach. This might be due to the density of amine modification being higher via the non-covalent approach. Further, the crystal structure was compared with XRD measurements. The sharp peak appeared in covalently incorporated RB AMSNs suggested that compound has little crystalline nature, but the RB doped by non-covalent approach appeared in pure amorphous form. The XRD characteristic peak for both compounds obtained at $2\theta = 23.7^\circ$ and two sharp and narrow peaks at $2\theta = 37^\circ$ and 43° degrees were observed in covalently doped RB AMSN sample. The average

crystallite size measured by Scherrer equation as 10.8 and 13.6 Å in covalent and non-covalent approaches respectively.

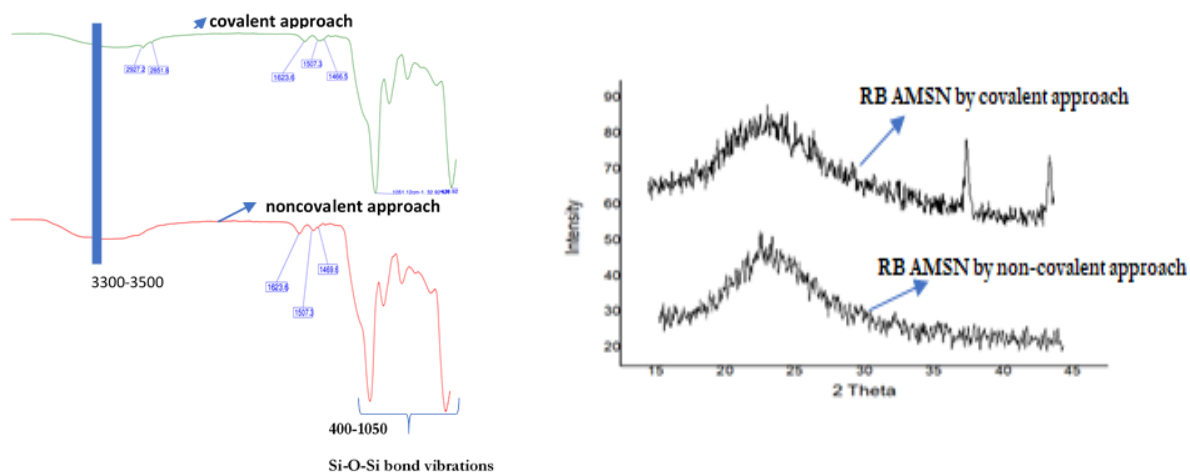


Figure 3.15: (A) FT-IR spectrum and (B) XRD comparison of RB-AMSNs synthesized by covalent and non-covalent approaches.

Conversely, the solid-state UV-Vis spectral studies showed higher UV absorption for physically entrapped dye molecules (Fig 3.16). Using the covalent approach, only a specific number of dye molecules can be entrapped inside the silica matrix whereas, in non-covalent approach, a large numbers of dye molecules are trapped inside the mesopores that might contribute to the high UV absorption values. Both compounds showed fluorescence under UV light.

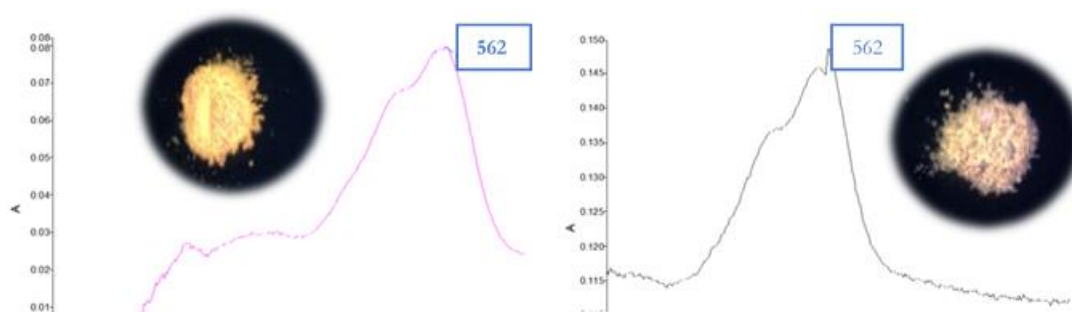


Figure 3.16: Solid-state UV-Vis absorption spectra for RB AMSN doped by covalent and non-covalent approaches respectively (inset- compounds under UV lamp)

3.3.3 Effect of synthesis parameters on MB doped AMSNs

The characteristic properties of MSNs such as particle size, morphology, and porosity are greatly affected by the reaction parameters[50]. This project investigated how various reagent concentrations affect the particle morphology and size distributions, using the SEM, and BET, measurements. MB doped AMSNs were chosen for these studies.

Results showed that the size of particles decreased with decrease in CTAB molar ratio from 0.5 to 0.15, whereas surface area increased. Further decreased CTAB ratio resulted the macro-porous material (pore size - 60 nm). The concentration of surfactant molecules plays a significant role in controlling the particle shape and morphology. Higher surfactant concentrations lead to a greater number of micelles in the aqueous solution. When the surfactant concentration reaches more than the CMC, this led to disordered pore structure. These results had good agreement with the reported literature [165].

Table 3.2: Effect of various reagent concentrations on the morphology of MB doped AMSNs

TEOS	APTES	CTAB	NH ₄ OH	H ₂ O	EtOH	S _{BET} (m ² /g)	BJH pore size (nm)	Pore volume (cm ³ /g)	SEM (~ nm)
1	0.25	0.5	1	144	50	6.83	19.4	0.03	400
1	0.25	0.15	0.2	144	50	149.15	3.9	0.1	350
1	0.25	0.1	0.5	800	50	175.57	14.9	0.4	200
1	0.25	0.1	1	144	50	149.14	4	0.13	300
1	0.25	0.1	0.2	144	50	11.24	60	0.06	450
1	0.25	0.1	0.2	800	50	227.9	3	0.2	-

The pH of the reaction medium controls both the hydrolysis of silane and condensation of siloxane. Therefore, the effect of base catalyst NH₄OH was also studied in this project. The results

observed as the surface area decreased drastically by decreasing the concentration of the base catalyst (Table 3.2). Usually, during the synthesis of MSNs, the reaction was performed at $\text{pH} > 10.86$, where silicate condensation reaches maximum, and they can possibly dissolve in aqueous solution. However, due to the strong interaction between CTAB and silicates, the formed composites were stable enough at higher pH ($\text{pH} = 12$) [166]. In addition to the concentration of NH_4OH , the amount of solvent also played crucial role in determining the particle morphology. It was observed that an increase in the quantity of water present resulted in the increase of surface area while the size of the nanoparticle decreased. The SEM results (Fig 3.17) also confirmed the same change in the particle size distributions.

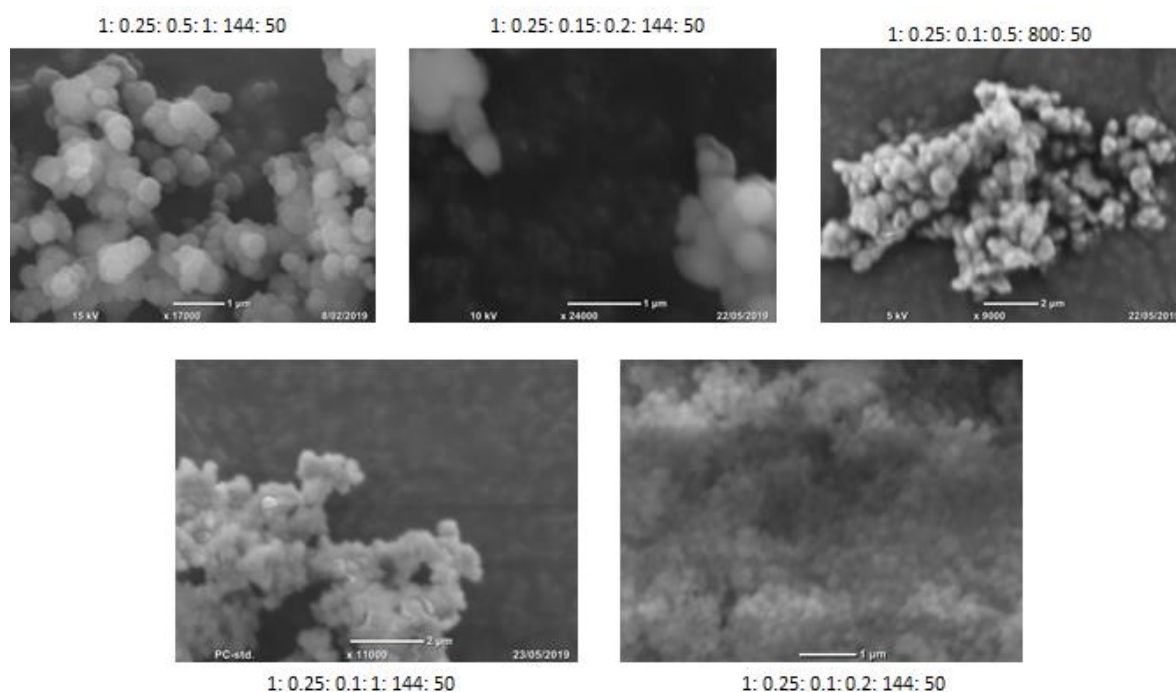


Figure 3.17: SEM images obtained for MB AMSN samples at various reaction parameters (molar ratios indicated as TEOS: APTES: CTAB: NH_4OH : H_2O : EtOH)

3.4 Conclusion

In summary, during this section of the project, the effect of various synthesis parameters on the surface properties of MSNs and MB doped AMSNs were studied. The size of the nanoparticle regulated between 150-400 nm by varying the concentrations of reagents, including CTAB, base, and solvent ratios. The obtained results showed a good correlation with literature values [97]. The

size of the nanoparticle increased while increasing the CTAB concentration, whereas the pore volume decreased. A single-step synthesis procedure was developed for the covalent encapsulation of RB into the MSNs matrix by modifying the existing methodology[148]. The physical and chemical characteristics for the RB, fluorescein, and MB doped mesoporous silica nanoparticles were investigated by various characterization techniques including SEM, BET, XRD, FT-IR, and UV.

Chapter 4

Synthesis and characterization of carbohydrate coated fluorescent MSNs

This chapter presents the synthesis methodology for coupling the carbohydrates with amine modified dye-doped MSNs and discusses the characteristic results.

4.1 Introduction

Lately, targeted drug delivery has received immense interdisciplinary attention from chemistry to medicine. Nanocarriers, which are highly biocompatible with the metabolic system and biodegradable, are the prime focus in this context [167]. The surface coating of nanoparticles with biomolecules such as carbohydrates, lipids, proteins, and nucleic acids has been the main focus. Glycol-nanoparticles (sugar-coated nanoparticles) have several advantages, including hydrophilicity, dispersibility, bio-availability, protein-repellent, and chemically well-defined structures [168],[169].

So far, carbohydrates have been used to couple with quantum dots [170](QDs), magnetic nanoparticles [171] (MNPs), inorganic nanoparticles [172],[173] (Cu, Au, carbon, etc.), and silica nanoparticles [174] for various biomedical applications. However, studies on glycans conjugated to mesoporous silica nanoparticles are relatively limited. Therefore, the present project focused on the development of various carbohydrate conjugated dye-doped mesoporous silica nanoparticles for investigation of their applicability in the field of bioimaging.

4.2 Experimental details

4.2.1 Details of Reagents

MB AMSNs, N, N'- carbonyl diimidazole (CDI) (Sigma-Aldrich, 530-62-1, $\geq 90\%$), D-(+)-Glucose monohydrate powder (Thermo Fisher Sci), D-(+)-Maltose monohydrate, D-(-)-Ribose (Sigma-Aldrich, 50-69-1, 98%), and D-(+)- raffinose pentahydrate (Sigma-Aldrich, 17629-30-0, $\geq 99\%$) were used as received without further purification. Millipore deionized water and ethanol were used throughout the project for washing the nanoparticles after centrifugation. A Vacuum oven was used for drying the synthesized nanoparticles.

N, N' - dimethylformamide (DMF) (99.5% Assay, 0.15% moisture) was dried with molecular sieves to ensure a moisture content $< 0.15\%$.

4.2.2 Characterization techniques

The phenol-sulfuric acid assay method was used to determine the degree of carbohydrate coupling. PerkinElmer ATR FT-IR is used to characterize the functional groups. Fluorescence of the samples observed through UV-lamp, whereas HP 8453 UV-Vis spectrometer was used to measure the absorbance of liquid samples. JEOL-JCM-6000 scanning electron microscope (SEM) was operated at 5 kV for measuring the size and shape of the sugar-coated nanoparticles. EMMA (Enhanced multi-materials analyzer) X-ray diffractometer (XRD) with Cu-K α ($\lambda=1.5418\text{\AA}$) at a scanning rate of 2° min^{-1} from 20° , $15^\circ - 45^\circ$ were used for characterizing the particle size and morphology. Micromeritics Tristar II Surface area and Porosity analyzer was used at liquid N₂ temperature ($\sim 77\text{K}$) to measure the surface area and porosity of the nanoparticles, and CHNS elemental analyzer was used for measuring total carbon and nitrogen percentages before and after sugar conjugation.

4.2.3 Experimental procedures

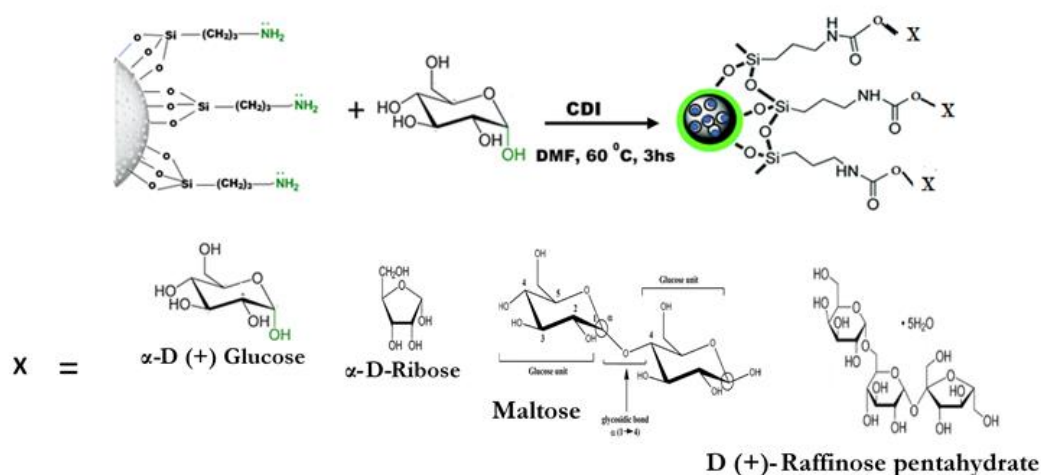
Sugar molecules were conjugated onto the surface of amine functionalized fluorescent MSNs with CDI as linking agent, according to the protocol mentioned in the literature [133],[175].

Methylene blue doped mesoporous silica nanoparticles were used for the functionalization with sugars including glucose, maltose, ribose, and raffinose pentahydrate. Glucose functionalized MSNs without dye-doping were also synthesized for measuring the degree of glucose functionalization by colorimetry and elemental analysis (EA).

Synthesis of carbohydrate coated methylene blue-doped mesoporous silica nanoparticles

In a typical synthesis, 5 ml CDI solution (10 mg/ml in DMF) was added to 11 ml carbohydrate solution (10 mg/ml in DMF) under an inert atmosphere (N_2) while maintaining the mole ratio of 1: 1 of CDI to carbohydrate. This mixture was allowed to stir for 3 hrs at 60 °C to achieve formation of the active imidazole intermediate. Then 5 ml MB AMSN solution (10 mg/ml in DMF) was added at R.T. and the reaction mixture allowed to stir overnight under inert atmosphere (N_2). After completion of the reaction, the particles were centrifuged and washed with a generous amount of D.H₂O and ethanol. The resultant particles were dried under vacuum at 30 °C overnight (Scheme 4.1).

The same method of synthesis was applied for the conjugation of glucose, maltose, ribose, and raffinose to the amine functionalized MB-doped silica (MB AMSN) surface.



Scheme 4.1: Schematic illustration of carbohydrate functionalization on dye-doped MSN.

Glu-MB MSN, Rib-MB MSN, Mal- MB MSN, and Raffi-MB MSN were synthesized during this project. (Glu- glucose, Rib- ribose, Mal- maltose, Raffi- raffinose, and MB- methylene blue).

Synthesis of glucose coated mesoporous silica nanoparticles

Glucose functionalized mesoporous silica nanoparticles were synthesized by taking amine functionalized MSNs without dye-doping.

In a typical process, 5.5 ml of a solution containing CDI (10 mg/ml DMF) and 62 mg of glucose monohydrate was stirred under inert atmosphere (N₂) for 3 hrs at 60 °C for the activation of glucose molecule. To the solution containing activated glucose, 50 mg of amine functionalized MSNs was added and stirred overnight at R.T., in an inert atmosphere. The resultant nanoparticles were separated by centrifugation and washed with D.H₂O then ethanol and dried under vacuum at 40 °C. The vacuum dried samples were used for the colorimetric analysis and elemental analysis.

Phenol-sulfuric acid method for measuring carbohydrate conjugation

The amount of glucose coupled to the amine grafted mesoporous silica nanoparticles was determined by the phenol-sulfuric acid method.

In a typical assay procedure, 1 mM stock solution of glucose was prepared by dissolving 18 mg of glucose monohydrate in 100 ml of D.H₂O. A standard curve was generated using glucose in concentrations of 20, 40, 80, 160, and 320 μM which were prepared by diluting 0.5, 1, 2, 4, and 8 ml stock solution to 25 ml with D.H₂O. For the detachment of α-D-glucose moiety from the glycol-MSNs, one ml of respective nanoparticle sample (10 mg/ 1ml) was treated with 200 μL of concentrated hydrochloric acid for 15 hrs. at 60 °C. After HCl treatment, the solution was centrifuged at 4000 rpm for 7 minutes (C-28A, Boeco centrifuge machine) and the supernatant was treated with one ml of 5 wt% phenol (5 g in 100 ml D.H₂O) and 5 ml of concentrated sulfuric acid. After vigorous mixing of the reaction mixture, it was incubated at room temperature for 30 min. The absorbance of the resulting mixture was measured at 490 nm on HP 8453 UV-Vis spectrometer. D.H₂O was used as a blank. The same procedure was repeated with standard solutions.

Elemental analysis

Elemental analysis was used to determine the percentage of carbon and nitrogen present in the sample, before and after the carbohydrate conjugation on the silica surface.

A CHN analyzer (carbon, hydrogen, nitrogen analyzer) was used to measure the elemental concentrations in a given sample. A known amount (micrograms) of the sample was weighed into a tin (Sn) container using a high precision balance. The percentage of elemental concentrations were calculated by flash combustion of the sample to cause instantaneous oxidation of the sample and detected with a thermal conductivity detector. The analysis was done by taking the glucose conjugated MSNs without dye doping and comparing the results with the precursor, amine modified MSNs. Each analysis was done in triplicate.

Dye leakage studies

To investigate any leakage of dye from the sugar-coated dye-doped MSNs, the samples were dispersed into the PBS (phosphate buffered saline, at pH 7.4) solution at 37 °C, stirred at 400 rpm for one hour. The solution centrifuged, and supernatant was taken to measure the UV absorbance measure at 634 nm. PBS was used as a blank.

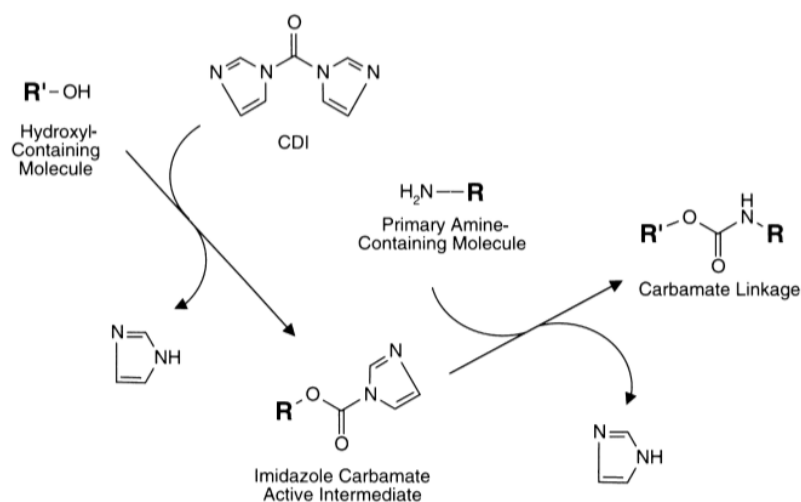
4.3 Results and discussion

Conjugation methodology

Various conjugation techniques are mentioned in the literature for reacting amine-modified surfaces of MSNs. EDC/NHS (1-ethyl-3(3-dimethylaminopropyl)carbodiimide/N-hydroxysuccinimide) coupling is the conventional way for coupling acids or alcohols with amines. This method is widely employed by many researchers for coupling silica nanoparticles with bioactive molecules[174]. Photocoupling chemistry based on click chemistry is also mentioned[130]. However, using CDI (N, N'-Carbonyl diimidazole) for coupling has advantages over other techniques. Firstly, the synthesis process involves a single step. This is not the case for the other techniques, which involve multiple stages for coating the sugars on the NPs surface. Multi-step synthesis required processing at each stage that consumes more chemicals and time. Therefore, the CDI method is eco-friendly and economical. Secondly, there is no need for special

synthesis conditions during the progress of the reaction. Finally, since only one solvent (DMF) is used during the entire synthesis protocol, it is possible to recover the solvent from water by azeotropic distillation after separating the nanoparticles from the reaction mixture.

CDI contains two acyl imidazole leaving groups and is a highly active carbonylating agent. CDI activates a hydroxyl group of the carbohydrate molecule for conjugation with an amine group, creating a one-carbon length N-alkyl carbamate linkage (Scheme 4.2). Paul and Anderson [176] first introduced this reaction to the synthesis of the peptides. However, CDI is highly sensitive to water and can decompose to two molecules of imidazole in the presence of water. Therefore, a polar aprotic solvent such as dimethylformamide (DMF) with moisture content less than 0.15 % has been used in this reaction.



Scheme 4.2: General schematic illustration of CDI mediated coupling reaction between hydroxyl containing molecule and primary amine-containing molecule (Reproduced from Bioconjugate techniques., 2013) [175].

Because of the 100 % reaction between CDI and carbohydrate molecules, regardless of yields the type of the carbohydrate used, a 1: 1 molar ratio was maintained for all sugars used in this study.

4.3.1 Physiochemical characterization of carbohydrate functionalized fluorescent MSNs

Estimation of the amount of glucose conjugated by phenol-sulfuric acid assay

The phenol-sulfuric acid assay can be used to estimate the number of carbohydrate molecules presented in a given sample [177],[178]. Therefore, this method was used for the determination of the degree of functionalization of the glycol-MSNs by making slight modifications to the reported procedure [179]. In this procedure, polysaccharides present in the sample are broken down to monosaccharides. Then pentose sugars (5-carbon compounds) dehydrate to furfural and hexoses (6-carbon compounds) to hydroxymethylfurfural. These compounds produce a yellow gold colour on reaction with phenol (Fig 4.1). Glucose is usually used to create a standard curve for the products that are high in hexose sugars. This method is accurate within $\pm 2\%$.

In the present study, this procedure was applied to glucose conjugated to the amine modified MSNs without dye doping. This is because the harsh conditions such as reaction with hydrochloric acid for the removal of the glucose moiety and addition of concentrated sulphuric acid during the assay process may also release the dye from the mesopores. This in turn may affect the UV absorbance value during the analysis.

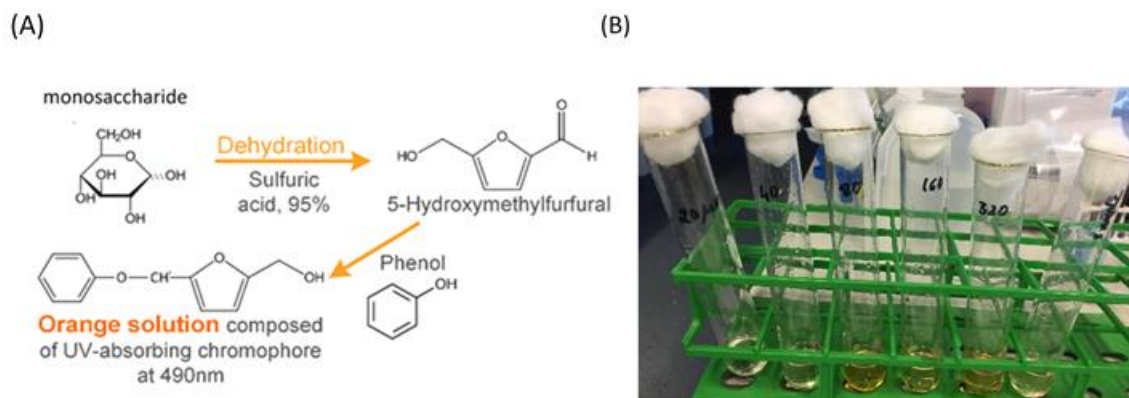


Figure 4.1: (A) Schematic illustration of the phenol-sulfuric acid method, (B) Coloured compounds obtained during colorimetric analysis.

The amount of surface-bound carbohydrate was computed by comparing the absorbance for the treated glucose conjugated MSNs with the calibration curve. From the corresponding calibration curve (Fig 4.2), the analysis revealed 0.23 glucose molecules/nm² grafted to the silica surface.

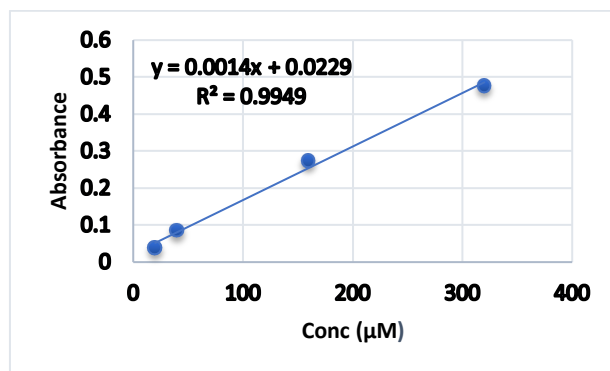


Figure 4.2: Standard curve for the phenol-sulfuric acid method

Elemental analysis (EA)

The coupling of glucose with AMSNs was further investigated by elemental analysis (EA). EA results for each of the samples tested are shown in Table 4.1 with calibration curve presented in Fig 4.3. The results are consistent with a ~ 2.5 % more carbon recorded in glucose bound MSNs compared with the AMSN.

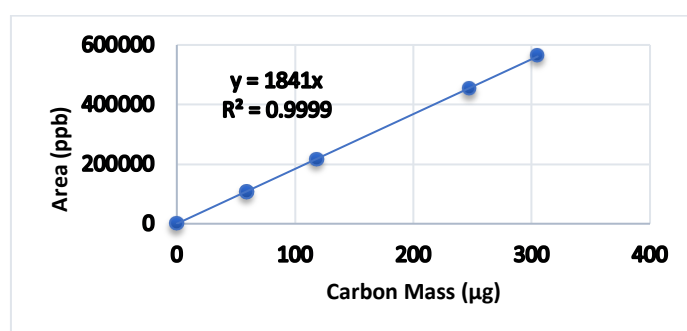


Figure 4.3: Carbon calibration curve using sulfanilamide as standard

Table 4.1: Elemental composition resulted from AMSN and Glu-AMSN

Sample	Mass(mg)	C Area (ppb)	C Area Blanked (ppb)	Response	% C	N Area (ppb)	N Area blanked (ppb)	Response	% N
Blank	0	1808	0			5301	0		
AMSN	0.976	124097	122289	127149	6.91	16818	11517	17232	2.78
Glu-AMSN	0.914	161722	159914	176939	9.61	18791	13490	20559	3.32
AMSN	3.060	406992	405184	133004	7.22	42728	37427	13963	2.25
Glu-AMSN	3.105	551557	549749	177635	9.65	56582	51281	18223	2.94
AMSN	2.034	266179	264371	130865	7.11	27102	21801	13324	2.15
Glu-AMSN	2.027	371929	369821	183339	9.96	35718	3.417	17621	2.84

Morphological characteristics of carbohydrate conjugated dye-doped MSNs

SEM images revealed that the obtained sugar-coated nanoparticles were roughly spherical and uniform in diameter, approximately 525 nm (Fig 4.4). These images suggested that the size of the nanoparticle was not affected by the type of the sugar used for the conjugation. However, a bigger size of nanoparticle was observed for Glu-RB MSNs (more than 550 nm) when compared with Glu-MB MSNs (~ 500 nm). The exact size of the nanoparticles could not be measured due to loss of resolution as the organic coating broke down under electron bombardment.

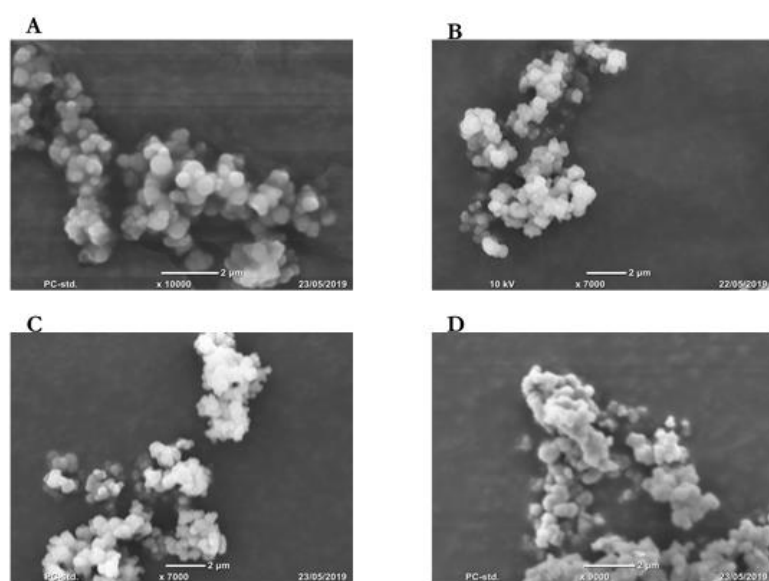


Figure 4.4: SEM images of (A) Glu-MB MSN, (B) Mal-MB MSNs, (C) Rib-MB MSN, and (D) Raffi- MB MSN.

Precise information regarding the structural characteristics of porous nano-materials was obtained for Glu- RB MSNs. It revealed type-IV isotherm of MCM-41 type. This suggests that the sample has uniform mesopores. It also suggested that the porous nature of the samples was not disturbed during the coupling reaction and that the glucose molecules coupled only with surface amine groups and were not absorbed into the pores. The BET surface area, pore size, and pore volume were calculated as 454.9 m²/g, 9.4 nm, and 0.75 cm³/g respectively. The BET analysis for other sugar-coated MSNs were not performed due to insufficient amount of compound.

The XRD diffraction pattern resulted in a broad peak at the 2θ value of 23.5°. The nature of the peak indicated the presence of amorphous silica nanoparticles (Fig 4.5). The average crystallite sizes calculated from Scherrer equation for glu, mal, rib, and raffi conjugated MBMSNs as 10.9, 11.9, 14.7, and 10.99 Å respectively.

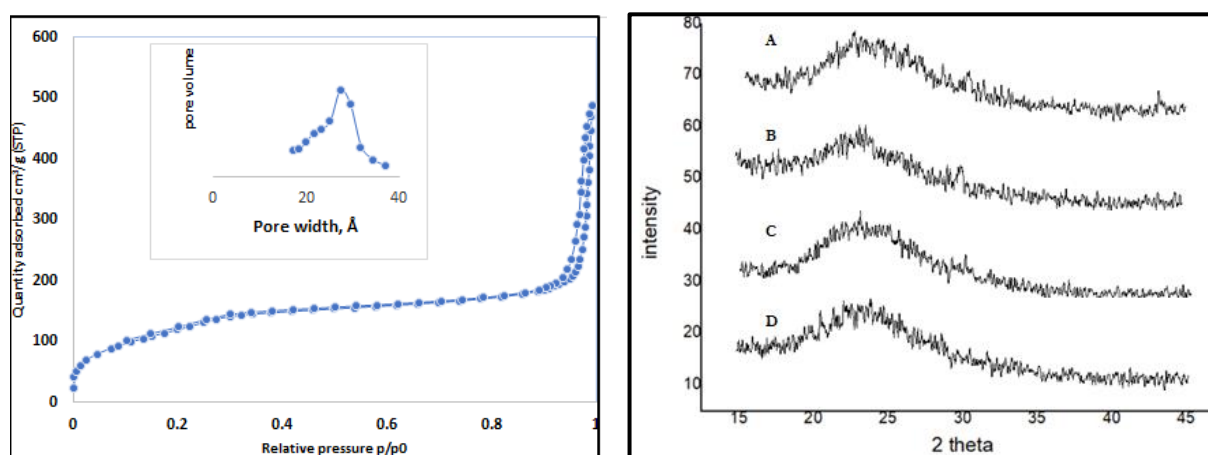


Figure 4.5: (left) N₂ sorption isotherms of glucose conjugated MB MNS (inset – pore size distribution), (right) XRD diffractograms of (A) Glu-MB MSN, (B) Mal-MB MSN, (C) Rib-MB MSN, and (D) Raffi-MB MSN, respectively

Nanoparticles were dispersed in ethanol for measurement of fluorescence properties. A bright fluorescence illumination of the nanoparticles was observed under the UV light (Fig 4.6), which suggested that the samples retained their fluorescence after conjugation with sugars.

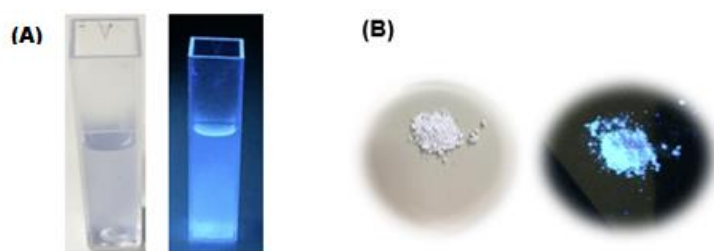


Figure 4.6: (A) Glu-MB MSN dispersed in ethanol under normal light and UV light and (B) powdered Glu-MB MSN under normal light and UV light.

Furthermore, dye leakage studies were investigated for carbohydrate functionalized MB doped MSNs. Nanoparticles were dispersed in PBS solution for investigating dye leakage because the interaction of nanoparticles with bacteria cells were studied in the presence of PBS. The low absorbance values of supernatant (Table 4.2) suggested that the dye leakage from the nanoparticles was negligible.

Table 4.2: Dye leakage studies on sugar-coated MB doped MSNs.

S.No	Sample Name	Absorbance (AU)
1	Glu-MB MSN	0.053029
2	Mal-MB MSN	0.089639
3	Rib-MB MSN	0.15030
4	Raffi-MB MSN	0.063903

Fourier-transform infrared (FT-IR) analysis was carried out to confirm the conjugation of the carbohydrate molecule with AMSNs (Fig 4.7). The broad spectral peak at around 3500 cm^{-1} corresponded to N-H stretching vibrations and the small peak at 1642 cm^{-1} corresponded to the amide carbonyl (C=O) stretch suggesting the formation of an amide bond between the carbohydrate molecule and AMSNs. The intense characteristic peaks in the region of $400\text{-}1100\text{ cm}^{-1}$ indicate the presence of silica in the sample.

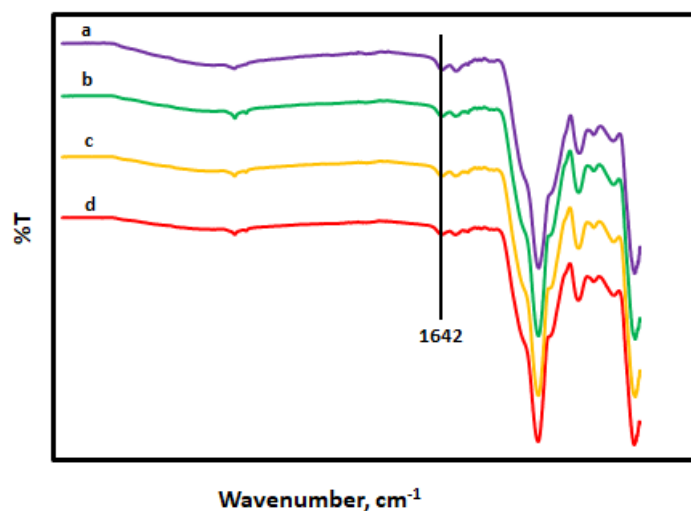


Figure 4.7: ATR FT-IR spectral studies for a) glucose, b) maltose, c) ribose, and d) raffinose conjugated MB MSNs, respectively.

4.4 Conclusion

In summary, during this stage of the project, carbohydrate conjugated fluorescent mesoporous silica nanoparticles have been developed for fluorescent labeling. MB doped AMSNs (MB AMSNs) were conjugated with four types of sugars, including glucose (Glu), maltose (Mal), ribose (Rib), and raffinose (Raffi). Morphological features such as SEM showed that there wasn't a significant difference in the size of the nanoparticles conjugated with different sugars. BET measurements showed that the surface area of the obtained sugar-coated nanoparticles was more than 450 m²/g, with mesoporous nature. Chemical characteristics including the glucose surface density were determined via phenol-sulfuric acid assay to be 0.23 glucose molecules/nm². The formation of the amide linkage between sugars and AMSNs, was confirmed by the presence of amide carbonyl stretching frequency in FT-IR spectra. Finally, the fluorescence properties of the samples were confirmed by the observation of bright illumination under a UV light and the dye leakage studies showed that there was negligible leakage of the fluorophore from sugar-coated samples.

Chapter 5

Investigations of Glu-MB MSN uptake by bacterial cells

This chapter presents the results obtained by the interaction of glucose conjugated fluorescent MSNs with *Escherichia Coli* (*E.Coli*) and *Bacillus Subtilis* (*B.Subtilis*) bacteria.

5.1 Introduction

Nanomaterials have been developed for delivering therapeutic agents to treat disease[180]. Due to their unique properties, mesoporous silica nanoparticles (MSNs) are the prime focus of this type of research. MSNs with appropriate surface modification, can reach the target and enter into pathological bacterial or cancerous cells, facilitating disease diagnosis and therapy [181]. Much of this research has been aimed at diseased mammalian cells. However, studies focused on bacterial interaction with nanoparticles are relatively few.

Bacteria are interesting and diverse. These tiny biological bodies make huge contributions to many systems and cycles. Their diversity and ubiquity make them model organisms for research.

This project investigated Glu-MB MSNs (glucose conjugated methylene blue doped mesoporous silica nanoparticles) interaction with *E.Coli* and *B.Subtilis* bacterial cells. These initial results may also indicate any cytotoxicity.

5.2 Experimental details

5.2.1 Materials used

E. Coli (Migula 1895) Castellani and Chalmers 1919) and *B.Subtilis* (BH 18 strain) bacterial strains were used for investigating the interaction with nanoparticles. Sterilized phosphate buffered saline (PBS) was used throughout the experiments with bacterial samples. Glycerol and p-phenylenediamine (PDA) were used in the preparation of mounting media. Sterilized Millipore deionized water was used for washing the samples throughout the experiments. 3.7% paraformaldehyde (1 ml 37% formaldehyde added to 9 ml of 1xPBS) was utilized for fixing the cells. All the glassware used were autoclaved at 121 °C for 15 min, before use. Glucose conjugated methylene blue doped mesoporous silica nanoparticles (Glu-MB MSN) were synthesized in the lab previously (Chapter 4). All bacterial samples were handled under Laminar flow hood to avoid contamination.

5.2.2 Instrumentation

Sigma 1-14 microfuge machine was used to centrifuge the samples. Hitachi UV spectrophotometer was used to measure the OD (optical density). Nikon (A1R MP) Confocal laser microscopy with 60x oil immersion object was used for observing the fluorescence of samples. JEOL-JCM-6000 Scanning Electron Microscopy (SEM) operated at 5-10 kV, and the samples were gold coated before imaging.

5.2.3 Experimental setup

Preparation of nutrient broth (NB)

200 ml nutrient broth (NB) was prepared by mixing, 2.6 g of Oxoid and 0.8 g yeast extract with 200 ml D.H₂O. The prepared NB was autoclaved at 121 °C for 15 min.

Preparing bacterial culture

Initial cultures were prepared of each bacterium by inoculating one full loop from cold-stored agar plates into 10 ml NB containing culture tubes. The culture tubes were grown overnight in a shaker incubator, 150 rpm at 37 °C. The OD of each was measured after approximately 16 hours.

Measuring the concentration of bacteria

Bacterial growth rate measurement is a fundamental microbiological technique and widely used in basic research. The concentration of the bacteria in experiments was determined in two ways, one direct (CFU/ml) and one indirect (OD method).

The growth of the bacteria is affected by both physical factors including pH, osmotic pressure, temperature, and moisture content in the medium as well as nutritional factors, including the amount of carbon, sulphur, and other trace elements supplied by the growth medium. The reproduction in bacterial samples occurs via binary fission. During this process, when a cell attains full growth, it divides into two. The amount of time needed for cell division is known as the mean generation time (MGT) or doubling time. This process continues in a geometric manner (Fig 5.1). During the MGT, the bacteria known to be in the actively growing phase.

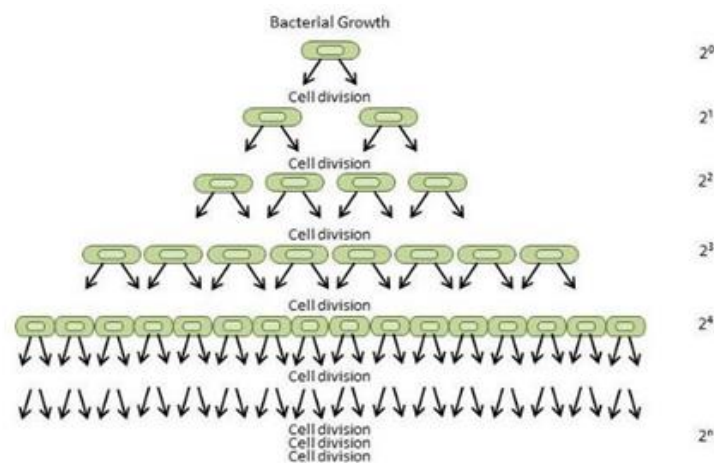


Figure 5.1: Exponential cell division (cell number increase explosively after n divisions resulted in 2^n cells) (Reproduced from Google images)

The growth curves of *E.Coli* and *B.Subtilis* bacteria are measured under optimal conditions, at 37 °C, and neutral pH. The effect of other physical and nutritional factors was not studied as part of this project. When a culture medium supplies all required nutrients and optimal conditions for

growth, then the number of viable bacteria can be measured as a function of time to attain a growth curve.

In a typical process for the determination of growth curve, the overnight *E.Coli* and *B.Subtilis* cultures were each re-inoculated into fresh 50 ml NB such that OD_{600} of the culture < 0.1 . The volume to achieve this was typically 1 ml. The cultures were well mixed and incubated at 150 rpm and 37 °C. Regular sampling commenced immediately for measurements of OD_{600} for five hours. Fresh NB was used for blank reading. A final OD_{600} reading was taken for each overnight bacterial suspension. From the obtained values, a logarithmic growth curve was plotted to determine the various growth phase lengths for each bacterium. OD_{600} plotted against time typically yields a sigmoidal growth curve. The $\log OD_{600}$ can also be plotted for ease of MGT determination.

A typical growth curve contains three important components lag, log, and stationary phases (Fig 5.2). The lag phase occurs when the organisms introduced to the fresh NB medium. During this phase, cellular metabolism is accelerated, and the size of each bacteria growing. However, the bacteria are not able to replicate, which means no increase in the cellular mass. The length of the lag phase depends upon the type of bacteria and the culture conditions. The growth curve is showing that the lag phase of the *E.Coli* was shorter than for *B.Subtilis*. *E.Coli* appeared to adapt to the new environment more quickly than *B.Subtilis*.

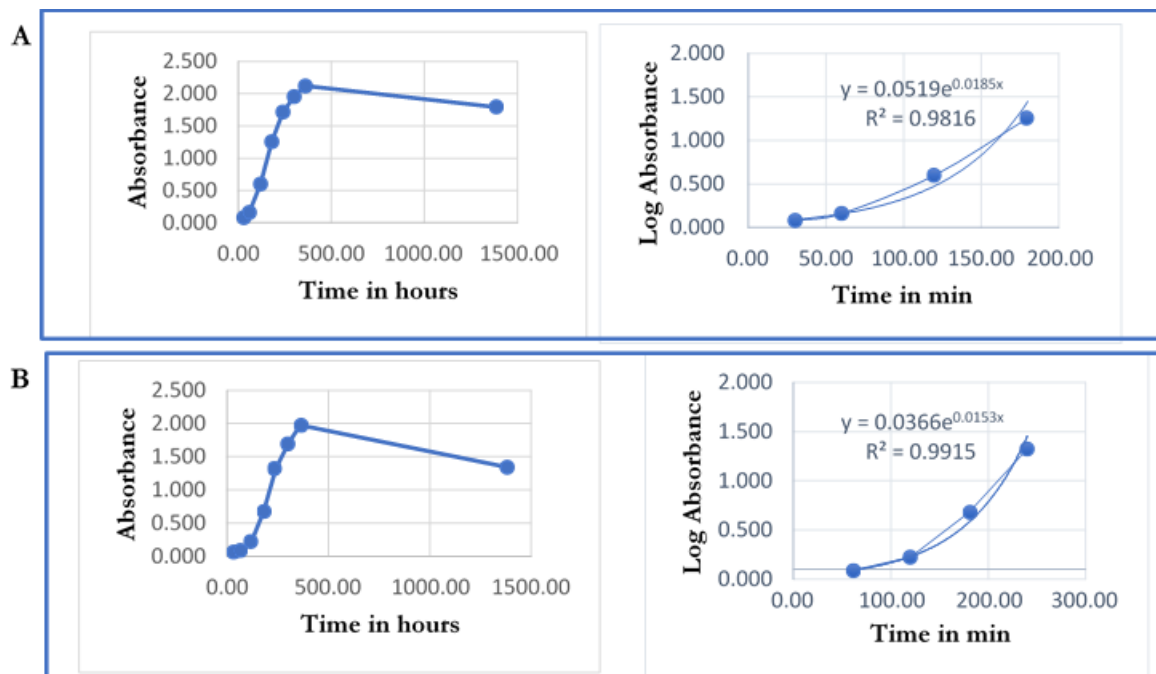


Figure 5.2: bacteria growth curve and mean generation time (MGT) curve respectively for (A) *E.Coli* and (B) *B. Subtilis*.

The doubling time or MGT is different for each organism. MGT is calculated from the growth curve. The logarithmic absorbance values of log phase were taken, and the points were extrapolated to meet the respective time axis. MGT was calculated from the following equation (Eq 5.1), by substituting the values obtained from the MGT curve.

$$T_d = \ln 2 / \mu \quad (\text{Eq 5.1})$$

where T_d is the doubling time or MGT and the value of μ obtained from the MGT graph (Fig 5.2). *E.Coli* doubled in 37 min, whereas *B.Subtilis* has taken 45 min to double.

After the log phase, once all the nutrients are largely consumed by the bacteria, a slower cell production rate is observed, and the number of cells produced is equal to the number of cells that die is known as stationary phase. Finally, the bacteria stop growing, and this phase is known as the death phase.

During the exponential or logarithmic (log) phase, the bacteria multiply rapidly. It is during the growth phase that cultures should be used for studying interactions with nanoparticles as their metabolic system is active and healthy.

The Miles and Misra method was employed for direct estimation of the number of viable *E.Coli* and *B.Subtilis* bacteria in each of the samples during the growth phase. In brief, the method requires serial dilutions of the bacterial suspension followed by the culture of aliquots on suitable agar media. Because each single cell grows to form a colony on the agar plates, the method is called the colony forming unit (CFU) determination. Ten-fold stepwise dilutions were employed in this project.

Two sets of nine dilution blanks were set up by pipetting 900 μL of autoclaved $\text{D.H}_2\text{O}$ into Eppendorf tubes 100 μL each of bacterial suspension during logarithmic growth phase (sampled at OD_{600} 0.462 for *E.Coli* and 0.427 for *B.Subtilis*), were pipetted into the first tube in each set, i.e., one in 10 dilution. After vortexing to mix, 100 μL of the prepared diluted culture was added to the second tube in each set to create a 1 in 100 dilution of each culture. The process was repeated up to 1 in 10^8 , dilutions.

All diluted samples were vortexed, and from each dilution, 25 μL of *E.Coli* and 20 μL of *B.Subtilis* were dropped onto the respective nutrient agar plate (supporting information (SI):1) and spread with a sterile glass spreader. The nutrient agar plates were allowed to dry under laminar flow for 20 min before inversion and incubation overnight at 37 $^\circ\text{C}$. The next day, the number of colonies

that had grown were counted in order to calculate the number of CFU/ml in the original suspension for each culture and compared to the OD₆₀₀ (Fig 5.3).

Plates with high bacterial concentrations resulted in a large number of merged colonies. Therefore, the colonies were counted where the highest number of discrete colonies can be seen (10⁵ dilutions). The number of CFU/ml present in the original aliquot is calculated Eq 5.2. There are several advantages of this method compared to OD method that includes non-hazardous, and fewer bacteria contamination at the workplace.

At OD₆₀₀ 0.45, *E.Coli* and *B.Subtilis* equated to 4 x 10⁸ and 1.6 x 10⁷ CFU/ml respectively.

CFU/ml = (Number of colonies x dilution factor)/volume of aliquot plated (Eq 5.2)

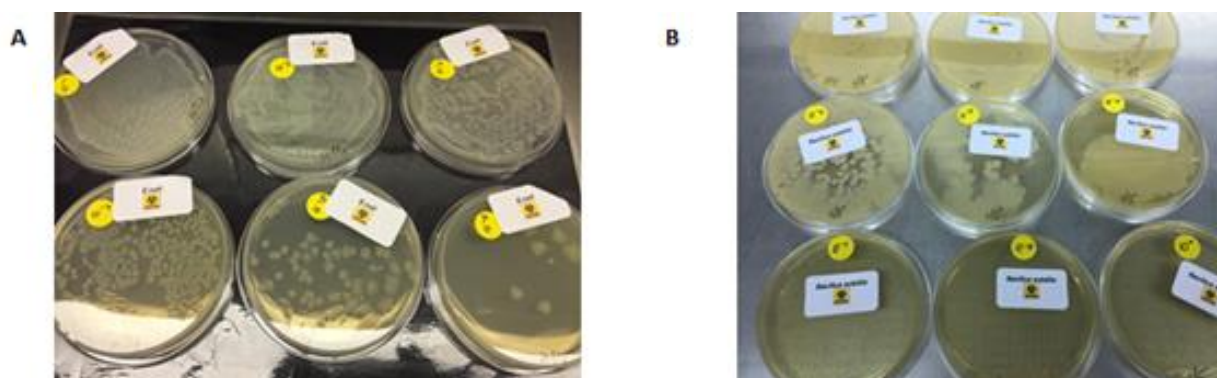


Figure 5.3: Serial dilutions of (A) *E.Coli* and (B) *B.Subtilis*

Incubating the bacterial cultures with nanoparticles

Glu-MB MSN, were used for investigating the nanoparticle interaction with *E.Coli* (Migula 1895) and *B. Subtilis* (BH18) bacterial strains.

In a typical experiment, one milliliter each of the *E.Coli*, (approximately 4x10⁸ CFU/ml) or *B.Subtilis* (approximately 2.4x10⁷ CFU/ml) bacterial cultures were transferred into 1.5 ml-Eppendorf tubes and centrifuged at 10000 rpm for 10 min to make a pellet. The supernatant was discarded, and the bacterial pellets were dispersed in one ml each of 1xPBS (SI:2) by vortexing. From these suspensions, 500 μL each of *E.Coli* and *B.Subtilis* were transferred into sterile McCartney tubes containing one milligram each of Glu-MB MSN in 5 ml of 1xPBS solution. The resultant bacterial suspensions were incubated at 37 °C, for 3hr on a shaker at 200 rpm.

Fixing the cells

The bacterial samples needed to be fixed to observe them microscopically. Paraformaldehyde was used to fix the samples. A volume of 3.7% paraformaldehyde equal to the volume of bacterial suspension was added directly to the suspension and allowed to settle for 20 min at R.T.

One ml each of bacterial suspension was then centrifuged for one min at 2000 rpm. The supernatants were decanted, and the pellets were each resuspended into one ml of D.H₂O for washing off free nanoparticles and again spun down for one min at 2000 rpm. The supernatants were discarded, and the resultant pellet dispersed into 50 µl of D.H₂O.

Slide preparation

The following procedure was performed in triplicate to prepare the samples to observe under confocal microscopy. First, glass slides were washed with 70% ethanol and dried. 50 µL each of the fixed and washed bacterial suspensions were dropped onto the slides for each bacterial sample and dried under vacuum at 40 °C.

A drop of mountant 90 % glycerol mountant (preparation, SI:3) was added to each of the vacuum dried slide. Then 22x22 mm disposable coverslips were mounted on to the slides. The mountant dispersed without assistance between the slide and coverslip. Since the mountant does not dry, the excess mountant was removed by absorbing it with Kim wipes. Finally, the sides of the coverslips were secured with colourless nail polish. Slides prepared in this way can be stored at 4 °C up to 3 months.

5.3 Results and discussion

Basic cell wall structure of E.Coli and B.Subtilis

Bacteria are prokaryotes and they do not possess a nuclear membrane. Bacteria can be classified as gram-positive or gram-negative. The cell wall structure is the major difference between the gram-positive and gram-negative bacteria. Gram-positive bacteria such as *E.Coli* possess an inner and outer cytoplasm membrane, and the periplasmic space between the membranes contains one or two layers of peptidoglycan (Fig 5.4).

On the other hand, *B. Subtilis*, a gram-positive bacteria, does not have an outer membrane. Instead, it has 10-20 layers of peptidoglycan [182]. The structure of peptidoglycans is almost the same in *E. Coli* and *B. Subtilis* [183]. Peptidoglycan is a polysaccharide. It is made of alternated chains of glucose derivatives, N-acetylglucosamine, and N-acetylmuramic acid.

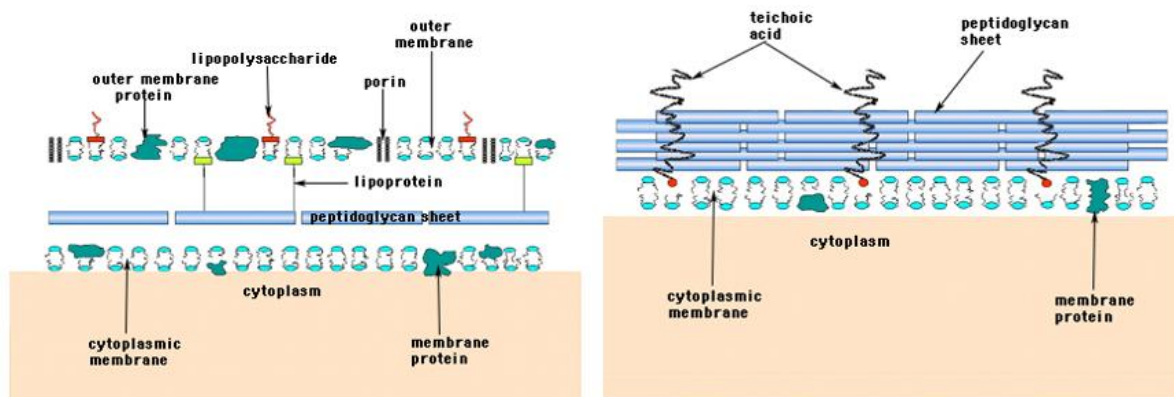


Figure 5.4: Cell wall structures of a gram negative and gram positive bacteria, respectively (Reproduced from Online textbook of bacteriology).

Bacteria-nanoparticle conjugation is not well explored and could be a new tool for diagnosis and treatment for a disease like cancer. The bacteria carrying the nanoparticles containing the therapeutic molecule can reach the targeted site effectively, which is difficult for conventional chemotherapeutic drugs. In this scenario, it is essential to study the interaction and toxicity of nanoparticles with both types of bacteria as the interaction might be different with a different outer structure.

Interaction with and toxicity of nanoparticles to bacteria were investigated in JEOL-JCM-6000 scanning electron microscopy (SEM) which was operated at 5 kV. Glu-MB MSNs incubated with each of *E. Coli* (4×10^8 CFU/ml) and *B. subtilis* (1.6×10^7 CFU/ml) for 3 hrs, were used for this investigation.

SEM images showed that bacteria formed aggregates in the presence of the nanoparticles (Fig 5.5). In addition, an increased bacterial density was observed after its incubation with nanoparticles. The bacteria might be using the conjugated glucose component from the Glu-MB MSNs as a source of food for binary fission. Note that NB was removed from the culture media before incubation with nanoparticles and therefore the only carbon source present was that on the nanoparticle

surface. This observation was supported by a previous study [184] where *B.Subtilis* aggregation was also observed in the presence of glucose in a mineral salt medium.

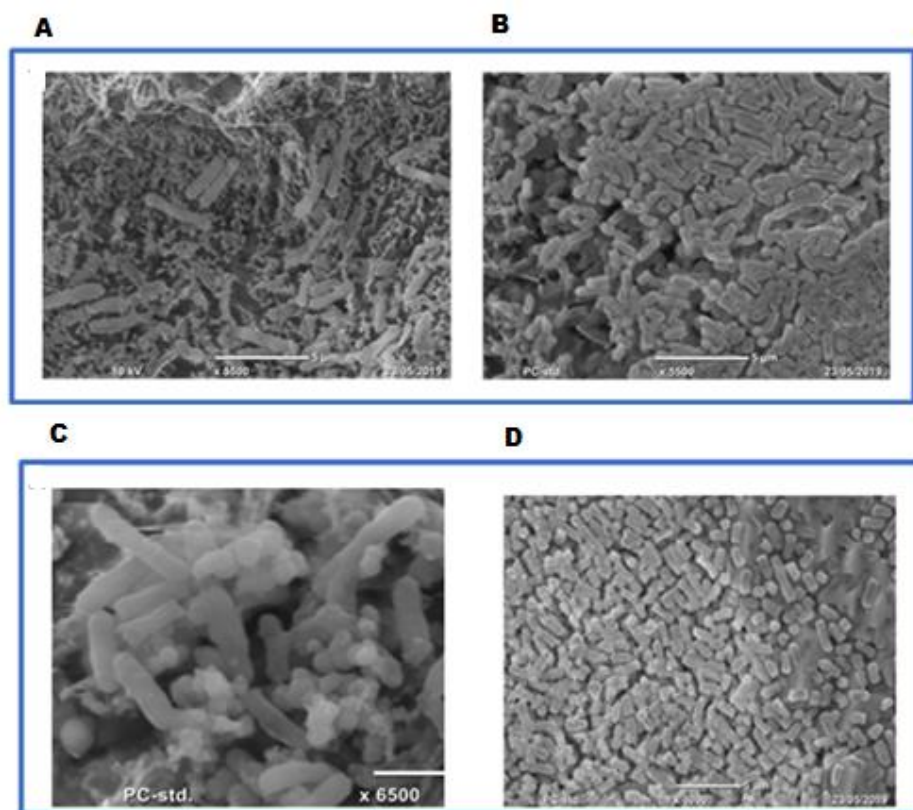


Figure 5.5: (A) and (B), SEM images of pure *B.Subtilis* *E.Coli* respectively. (C) and (D) *B.Subtilis* and *E.Coli* cultures after 3 hrs incubation with Glu-MB MSNs.

An initial indication of toxicity of the Glu-MB MSNs nanoparticles towards bacteria was observed by comparing the outer cell structure of the bacteria before and after the bacterial incubation with nanoparticles. SEM images revealed that the outer cell wall structure did not appear to be damaged in either culture after 3 hrs of incubation. This suggests that the Glu-MB MSNs were not toxic. Some researchers reported toxicity of APTES modified silica nanoparticles towards the *E.Coli* and observed changes to cell structure as a result [185],[186]. These studies reported that the bacteria outer cell membrane was damaged due to the contact with amine-functionalized silica nanoparticles. They also mentioned that the lipid bilayer structures of the bacteria interact with amine functionalities, which led to the death of cells. Studies based on the interaction of glucose conjugated nanoparticles with either *E.Coli* or *B.Subtilis* were not found in the literature. Therefore, to confirm the toxicity of the Glu-MB MSN on *E.Coli* and *B.Subtilis*, more studies with different incubation periods and CFU/ml measurements with and without nanoparticles as well as with

varying nanoparticle concentration need to be done to confirm the lack of toxicity suggested by the SEM results.

Fluorescence studies

The interaction of Glu-MB MSNs with *E.Coli* and *B.Subtilis* was further assessed based on the laser confocal microscopy. As for the SEM, aggregated bacterial cells were observed under confocal microscopy for *B.Subtilis* after 3 hrs of incubation with nanoparticles but not for *E.Coli* (Fig 5.6).

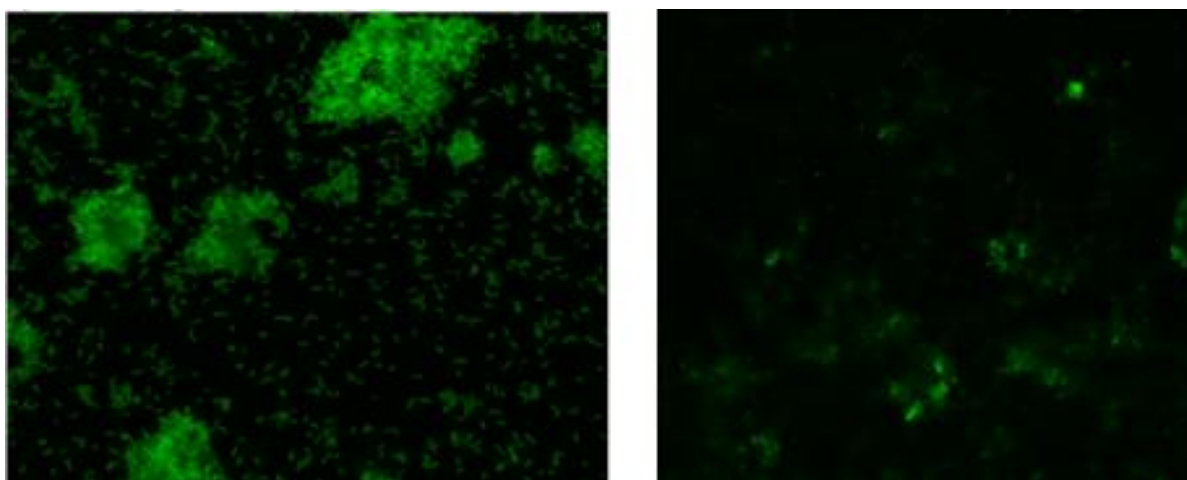
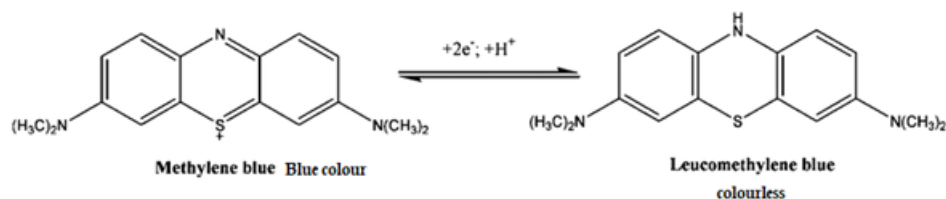


Figure 5.6: Confocal microscopy images of *B.subtilis* and *E.coli*, respectively (after incubation with Glu-MB MSNs for 3 hrs).

Confocal microscopy is a non-invasive optical imaging technique with minimal sample preparation. It works on a principle of point excitation in the specimen and detection of resultant fluorescence signal. Therefore, biological samples are often stained with fluorescent dyes to make them visible in confocal imaging. However, in this study bacterial samples incubated with nanoparticles were not stained for confocal imaging because the nanoparticles themselves have a fluorophore. The bright illumination for the bacterial samples interacted with nanoparticles comes from the MB which was doped inside the mesopores, not from the bacteria. The fluorescence observed here is of a characteristic shape and size (approximately 3 μm and rod-shaped) of bacterial cells. Samples of bacteria that had not been incubated with nanoparticles exhibited no fluorescence. To confirm that the fluorescent nanoparticles indeed associated with bacteria a bacterial specific counterstain is required. There was insufficient time to perform this.

Further supporting on interaction of the bacteria with nanoparticles, note the chemistry of methylene blue (MB) dye in biological systems. Usually, the cationic biocompatible redox indicator (Scheme 5.1), MB reacts immediately with biological components such as DNA, which is negatively charged. Once this occurs, MB becomes nonfluorescent. Therefore, the fluorescence observed in the confocal microscopy is not due to the leakage of MB.



Scheme 5.1: MB redox reaction

At this point, it cannot be confirmed whether the nanoparticles are intra or extracellular. More characterization is required for further confirmation of Glu-MB MSNs uptake into *E. Coli* and *B. Subtilis* bacterial cells. Fluorescence imaging is an important tool in biological research. Fluorescent probes with good solubility, high stability, and a proper emission spectrum are highly desirable for bio-imaging applications. These early results indicate that imaging is a possible application of these Glu-MB MSNs.

5.4 Conclusion

The as-synthesized Glu-MB MSNs were investigated for interactions with the microorganisms, *E. Coli* and *B. Subtilis* via SEM and confocal microscopy. The studies revealed that the nanoparticles showed good interaction with *B. Subtilis* and suggested no toxicity for either bacteria. Confocal microscopy results on bacterial samples revealed that the nanoparticles might be used for bioimaging. To support these results, more toxicity and viability studies need to be performed.

Supporting information

1. Preparation of nutrient agar plates

For preparing 20 nutrient agar plates, 11.2 g nutrient agar, 1.6 g agar, and 0.8 g yeast extract were dissolved in 400 ml of D.H₂O and mixed vigorously to dissolve. The resulting solution is sterilized at 121 °C for 15 min and transferred into a petri dish and allowed to cool in a laminar flow hood.

2. Preparation of phosphate buffered saline (PBS)

One liter of 10xPBS was prepared by dissolving 80 g sodium chloride (NaCl), 2 g potassium chloride (KCl), 14.4 g of disodium phosphate (Na₂HPO₄), and 2.4 g KH₂PO₄ in 1 liter of D.H₂O. The pH adjusted to 7.4 with 1 N sodium hydroxide (NaOH). The resultant solution sterilized in an autoclave at 121 °C for 15 min.

1xPBS solution was prepared by adding 90 ml of D.H₂O to 10 ml of 10xPBS solution and sterilized at 121 °C for 15 min.

3. Preparation of Mountant

90 % glycerol mounting media prepared by adding one ml of 1xPBS to 9 ml of glycerol and vortexed for mixing. To this solution, 10 mg of p-phenylenediamine (PDA) is added as an anti-fading agent. The obtained solution is stored at 4 °C in the dark.

Chapter 6

Summary and Future outlook

6.1 Summary

Mesoporous silica nanoparticles (MSNs) have gathered considerable attention in the field of nanomedicine due to their distinctive features such as physiochemical stability, easy surface functionalization, and biocompatibility. Dye-encapsulated fluorescent MSNs emerge with great potential for theranostics. Fluorescent MSNs doped with organic dyes exhibit many advantages such as high hydrophilicity and low toxicity. Therefore, organic dyes such as rhodamine B (RB), fluorescein, and methylene blue (MB) fluorophores were used to encapsulate in the amine modified MSNs by covalent and non-covalent approaches with the modified co-condensation sol-gel technique.

RB entrapped into the silica matrix by both covalent and non-covalent approaches, whereas fluorescein and methylene blue were doped via the non-covalent approach. The existing multi-step process was modified into a single-step for the synthesis of RB doped AMSNs. Also, the effect of reagent concentration on the particle size, surface area, and porosity was investigated in the case of MB doped AMSNs and compared with literature findings. It was observed that the particle size decreased with decreasing surfactant concentration up to the critical micelle concentration.

Conversely, the particle size increased when the concentration of base catalyst (NH_4OH) decreased because ammonia protects the newly formed silica particles from aggregation. In addition to this, comparative studies of RB doped AMSNs synthesized via covalent and non-covalent approaches showed no significant difference in their characteristic SEM, UV-Vis, and XRD results. However, further characterization such as fluorescence spectra is needed to compare the fluorescent intensity of the dye-doped nanoparticles via these approaches because

In the next stage, four different types of carbohydrate molecules (glucose, maltose, ribose, and raffinose) were used to couple with MB doped AMSNs (MB AMSNs) by employing N, N'-carbonyl diimidazole (CDI) as a coupling agent. The obtained particles were characterized by FT-

IR, SEM, XRD, and UV-Vis. The degree of carbohydrate conjugation was determined by calorimetry and elemental analysis showed that the coupling reaction was successful between sugar and MB AMSN.

The potential uptake of glucose derivatized MB AMSNs by cells of *E.Coli* and *B.Subtilis* was then investigated. The SEM results suggested that there was a significant interaction of nanoparticles with *B.Subtilis* compared with *E.Coli*. In addition to this, no visible cell-wall structure damage was observed in SEM images. The laser confocal microscopy images showed bright fluorescent bacteria-like shapes, indicating that the nanoparticles may be useful as imaging agents — however, more characterization is needed for evaluating the actual interaction of bacteria with Glu-MB MSNs.

6.2 Future outlook

The findings of this project suggest that the organic fluorophores without reactive groups can also be employed for dye doping in MSNs and used for bio-imaging with suitable surface functionalization.

In the future, we plan to

- Investigate more regarding the bacteria interaction with nanoparticles in particular, whether the nanoparticles are intra or extracellular and confirm the apparent lack of toxicity.
- Synthesis of MB doped MSNs loaded with therapeutic molecules for simultaneous bioimaging and targeted delivery in mammalian cells.

Bibliography

1. **J Lei, L.W., J Zhang;** Superbright Multifluorescent Core–Shell Mesoporous Nanospheres as Trackable Transport Carrier for Drug : *ACS Nano*, 2011. **5**: p. 3447.
2. **L Wang, K.W., S Santra, X Zhao;** Watching Silica Nanoparticles Glow in the Biological World: *Anal. Chem*, 2006. **78**: p. 646.
3. **Y Chen, K.A., J Liu, G Sun;** Multifunctional envelope-type mesoporous silica nanoparticles for pH-responsive drug delivery and magnetic resonance imaging : *Biomater*, 2015. **60**: p. 111.
4. **Cai W, C.X.;** Nanoplatforms for targeted molecular imaging in living subjects: *Small*, 2007. **3**: p. 1840.
5. **W Tan, M.-C.E., Meghan B, X Chen;** Highly fluorescent dye-doped silica nanoparticles increases flow-cytometry sensitivity for cancer cell monitoring: *Nano. Res*, 2009. **2**: p. 448.
6. **N Thepwiwatjit, A.T., Pichert L,J;** *J. Nanomater*, 2014. **851905**: p. 6.
7. **S Santra, P.Z., K Wang;** Conjugation of biomolecules with luminophore-doped silica nanoparticles for photostable biomarkers: *Anal. Chem*, 2001. **73**: p. 4988.
8. **W H Zhang, X.X.H., X B Zhang;** Dye-doped fluorescent silica nanoparticles for live-cell and *in vivo* bioimaging: *Nanomater*, 2016. **6**: p. 81.
9. **Tavernaro I, C.C., Peuschel H;** Bright fluorescent silica-nanoparticle probes for high-resolution STED and confocal microscopy: *B. J. Nanotech*, 2017. **8**: p. 1283.
10. **M-C M, L.D., Colilla M;** Lectin conjugated pH responsive mesoporous silica nanoparticles for targeted bone cancer treatment: *Acta. Biomater*, 2018. **65**: p. 393.
11. **C C Lin, Y.C.Y., C Y Yang, C L Chen;** Slective binding of mannose encapsulated gold nanoparticles to type 1 pili in *E.Coli*: *J. Am. Chem. Soc*, 2002. **124**: p. 3508.
12. **Y J Chen, S.H.C., Y Y Chein, Y W Chang;** Carbohydrate encapsulated gold nanoparticles for rapid target protein identification and binding epitope mapping: *ChemBioChem*, 2005. **6**: p. 1169.
13. **Bertozzi C R, K.L.L;** Chemical-Glycobiology: *Science*, 2001. **291**: p. 2357.
14. **Rabinovich G A, T.M.A;** Turning ‘sweet’ on immunity: galectin-glycan interactions in immune tolerance and inflammation:*Nat. Rev. Immunol*, 2009. **9**: p. 338.

15. **van Kasteren SI, C.S., Serres S, Anthony DC, Sibson NR, Davis BG;** Glyconanoparticles allow pre-symptomatic in vivo imaging of brain disease: *Proc. Natl. Acad. Sci. U S A*, 2009. **106**: p. 18.
16. **Reynolds AJ, H.A., Russell DA;** Gold glyconanoparticles for mimics and measurement of metal ion-mediated carbohydrate-carbohydrate interactions: *Langmuir*, 2006. **22**: p. 1156.
17. **Malgras, V., H. Atae-Esfahani, and Wang;** Nanoarchitectures for mesoporous metals: *Adv. Mater.*, 2015. **28**(6): p. 993.
18. **Michał Moritz, M.G.-M.;** Mesoporous materials as multifunctional tools in biosciences: Principles and applications: *Mater. Sci. and Eng: C*, 2015. **49**: p. 114.
19. **Lu Wang, W.D., Yubiao Sun;** The preparation and application of mesoporous materials for energy storage: *Mater. Res. Bull*, 2016. **83**: p. 230.
20. **J.S. Beck, J.C.V., W.J. Roth, M.E. Leonowicz;** A new family of mesoporous molecular sieves prepared with liquid crystal templates: *J. Am. Chem. Soc.*, 1992. **114**: p. 10834.
21. **Q.S. Huo, D.I.M., U. Ciesla, P.Y. Feng, T.E. Gier;** Generalized synthesis of periodic surfactant/inorganic composite materials: *Nature*, 1994. **368**: p. 317.
22. **Y.F. Shi, Y.W., R.L. Liu, B. Tu, D.Y. Zhao;** Synthesis of Highly Ordered Mesoporous Crystalline WS₂ and MoS₂ via a High-Temperature Reductive Sulfuration Route: *J. Am. Chem. Soc.*, 2007, **129**: p. 9522.
23. **T. Yu, Y.H.D., L. Wang;** ordered mesoporous nanocrystalline titanium-carbide/carbon composites from in situ carbothermal reduction: *Adv. Mater.*, 2007. **19**: p. 2301.
24. **S.M. Holmes, B.E.G., P. Foran;** A novel porous carbon based on diatomaceous earth: *Chem. Commun.*, 2006. **25**: p. 2662.
25. **Hoffmann, F., Cornelius, M., Morell, J., & Fröba, M;** Silica based mesoporous organic-inorganic hybrid materials: *Angew. Chem. Inter. Ed*, 2006. **45**: p. 3216.
26. **V. Chiola, J.E.R., C.D. Vanderpool;** Process for producing low-bulk density silica: US Patent 3 556 725, 1971.
27. **D Zhao, Q.H., J Feng, B F Chmelka;** Nonionic triblock and star diblock copolymer and oligomeric surfactant syntheses of highly ordered, hydrothermally, mesoporous silica structures: *J. Am. Chem. Soc*, 1998. **120**: p. 6024.
28. **Ghodsi Mohammadi Ziarani, V.F.V., Alireza B;** The role of SBA-15 in drug delivery: *RSC Adv*, 2015. **5**: p. 91686.
29. **S. Inagaki, Y., Fukushima, K. Kuroda;** Synthesis of highly ordered mesoporous materials from a layered polysilicate: *J. Chem. Sot. , Chem. Commun*, 1993. **680**.

30. **J.C. Jansen, Z.S., L. Marchese, W. Zhou, N. van der Puil;** A new templating method for three-dimensional mesopore networks: *Chem. Commun*, 2001. **136**: p. 713.
31. **T Yokoi, Y.S., O Terasaki, Y Kubota;** Periodic arrangement of silica nanospheres assisted by amino acids: *J. Am. Chem. Soc*, 2006. **128**: p. 13664.
32. **F. Kleitz, D.L., G.M. Anilkumar, I.-S. Park;** Large cage face-centered-cubic Fm3m mesoporous silica: synthesis and structure: *J. Phys. Chem. B*, 2003. **107**: p. 14296.
33. **C Yu, Y.Y., D Zhao;** Highly ordered large caged cubic mesoporous silica structures templated by triblock PEO-PBO-PEO copolymer: *Chem. Commun*, 2000. **0**: p. 575.
34. **Kumar D, S.K., von Hohenesche;** MCM-41, MCM-48 and related mesoporous adsorbents: their synthesis and characterisation: *Collid. Surf. A Phys. Eng. Asp*, 2001. **187-188**: p. 109.
35. **S, W.,** *Micro. Meso. Mater*, 2009. **117**: p. 1.
36. **Wang S, L.H;** Structure directed reversible adsorption of organic dye on mesoporous silica in aqueous solution: *Micro. Meso. Mater*, 2006. **97**: p. 21.
37. **Ukmar T, P.O;** Ordered mesoporous silicates as matrices for controlled release of drugs: *Acta. Pharm*, 2010. **60**: p. 373.
38. **Ge S, G.W., He X, Zhou B;** Effect of framework structure, pore size and surface modification on the adsorption performance of methylene blue and Cu²⁺ in mesoporous silica: *Colloid. Surf A Physiochem. Eng Asp*, 2018. **539**: p. 154.
39. **Gema G, Amaya.S, Tamara Z;** Influence of Microstructure in Drug Release Behavior of Silica Nanocapsules: *J. Drug. Delivery*, 2013. **2013**: p. 8.
40. **Rehman F, Volpe.PL, Arioldi C;** The applicability of ordered mesoporous SBA-15 and its hydrophobic glutaraldehyde-bridge derivative to improve ibuprofen-loading in releasing system: *Colloid. Surf. B. Biointer*, 2014. **119**: p. 82.
41. **S N Azizi, S.Ghasemi, H Y Sheldarrei;** Synthesis of mesoporous silica (SBA-16) nanoparticles using silica extracted from stem cane ash and its application in electrocatalytic oxidation of methanol: *Inter. J. Hydr. Ener*, 2013. **38**: p. 12774.
42. **Asma T Shah, S.A., M Kashif;** In situ synthesis of copper nanoparticles on SBA-16 silica spheres: *Chem, Arab. J.*, 2016. **9**: p. 537.
43. **Y Tozuka, A.W., K Kimura;** Effect of Pore Size of FSM-16 on the Entrapment of Flurbiprofen in Mesoporous Structures: *Chem. Pharm. Bull*, 2005. **53**: p. 974.
44. **Kato M, Hitoshi T, Abe N, Tomida T;** Adsorption Selectivity of FSM-16 for Several Organic Compounds: *J. Colloid Inter. Sci*, 2001. **242**: p. 294.

45. **Kai T, Q.M., Noritatsu T**; Molybdenum containing cage like mesoporous KIT-5 for enhanced catalytic conversion of 1-butene and ethylene to propene: *J. Molec Catal. A: Chem*, 2016. **416**: p. 39.
46. **M G Colmenares, U.Simon, S Arndt**; Oxidative coupling of methane on the Na₂WO₄-Mn_xO_y catalyst: COK-12 as an inexpensive alternative to SBA-15: *Cataly. Commun*, 2016. **85**: p. 75.
47. **Xilong W, P.D., Kebin C, Aijun D**; Synthesis of NiMo catalysts supported on mesoporous silica FDU-12 with different morphologies and their catalytic performance of DBT HDS: *Catalysis Today*, 2017. **291**: p. 146.
48. **Sunil Kumar, M.M.Malik, Rajesh Purohit**; Synthesis Methods of Mesoporous Silica Materials: *Mater. Today: Proceed*, 2017. **4**: p. 350.
49. **Naiara I V, Zoilo G, Begona Ferrari, Yolanda C**; Synthesis of mesoporous silica nanoparticles by sol-gel as nanocontainer for future drug delivery applications: *Boletín de la Sociedad Española de Cerámica y Vidrio*, 2017. **56**: p. 139.
50. **R Narayan, Usha Y Nayak, Ashok M R**; Mesoporous Silica Nanoparticles: A Comprehensive Review on Synthesis and Recent Advances: *Pharmaceutics*, 2018. **10**: p. 118.
51. **Saher R, J.-O.D., C Charnay.**, *Sol. Sta. Sci*, 2017. **68**: p. 25.
52. **Y Xie, Duyug K, C Chen, Yasar K**; Review of Research on Template Methods in Preparation of Nanomaterials: *J. Nano. Mater*, 2016. **2016**: p. 10.
53. **Y Yao, M Zhang, J Shi, M Gong**; Encapsulation of fluorescein into MCM-41 mesoporous molecular sieve by a sol-gel method: *Mater. Letters*, 2001. **48**: p. 44.
54. **Newalkar B L, J Olanrewaju, Komarneni S**; Microwave-hydrothermal synthesis and characterization of zirconium substituted SBA-15 mesoporous silica: *J. Phy. Chem B*, 2001. **105**: p. 8356.
55. **EB Celer, M Jaroniec**; Temperature-programmed microwave-assisted synthesis of SBA-15 ordered mesoporous silica: *J. Amer. Chem. Soc*, 2006. **128**: p. 14408.
56. **Y Chen, H-R Chen, J-L Shi**; Construction of homogenous/heterogeneous hollow mesoporous silica nanostructures by silica-etching chemistry: principles, synthesis, and applications: *Acc. Chem. Res*, 2014. **47**: p. 125.
57. **H Xu, H Zhang, D Wang, L Wu, X Liu, Z Jiao**; A facile route for rapid synthesis of hollow mesoporous silica nanoparticles as pH-responsive delivery carrier: *J. Colloid. Inter. Sci*, 2015. **451**: p. 101.
58. **Stober W, F.A., Bohn E**; Controlled growth of monodisperse silica spheres in the micron size range: *J. Colloid. Inter. Sci*, 1968. **26**: p. 62.

59. **Danks A E, SR Hall, Schnepf Z;** The evolution of 'sol-gel'chemistry as a technique for materials synthesis: *Mater. Horiz*, 2016. **3**: p. 91.
60. **Y Liu , J Goebel, Y Yin;** Templated synthesis of nanostructured materials: *Chem. Soc. Rev*, 2013. **42**: p. 2610.
61. **Barbara B, Serena E, Francesca S F,** *Mesoporous Titania: Synthesis, Properties and Comparison with Non-Porous Titania.*
62. **Y Wan, Y Shi, D Zhao;** Designed synthesis of mesoporous solids via nonionic-surfactant-templating approach: *Chem. Commun*, 2007. **38**: p. 897.
63. **Y Lu;** Surfactant-Templated Mesoporous Materials: From Inorganic to Hybrid to Organic: *Angew. Chem—Inter. Ed*, 2006. **45**: p. 7664.
64. **YK Hwang, JS Chang, YU Kwon, SE Park;** Microwave synthesis of cubic mesoporous silica SBA-16: *Micro. Meso. Mater*, 2004. **68**: p. 21.
65. **Nur H N K, AA Jalil, Sugeng T, Sharifah NT;** Microwave-assisted synthesis of mesoporous silica nanoparticles as a drug delivery vehicle: *Mal. J. Anal. Sci*, 2016. **20**: p. 1382.
66. **S Bian, K Gao, H Shen, X Jiang, Y Chen;** Organic/inorganic hybrid mesoporous silica membrane rapidly synthesized by a microwave-assisted method and its application in enzyme adsorption and electrocatalysis: *J. Mater. chem B*, 2013. **1**: p. 3267.
67. **Shan Li, F Wang, Hong Dai;** Self-assembly of silica nanoparticles into hollow spheres via a microwave-assisted aerosol process: *Mater. Res. Bull*, 2016. **74**: p. 459.
68. **G Ambrozic, ZC Orel, M Zigon;** Microwave-assisted non-aqueous synthesis of ZnO nanoparticles: *Mater technol*, 2011. **45**: p. 173.
69. **X Liu, Z.Jiao, T Song, M Wub, H Zhang;** Surfactant-assisted selective etching strategy for generation of rattle-like mesoporous silica nanoparticles: *J. Collid. Interf. Sci*, 2017. **490**: p. 497.
70. **M Wu, Y.Chen, L Zhang, X Li, X Cai;** A salt-assisted acid etching strategy for hollow mesoporous silica/organosilica for pH-responsive drug and gene co-delivery: *J. Mater. Chem. B*, 2015. **3**: p. 766.
71. **Jing Xu, X Wang, Z Teng, G Lu, N He, Z Wang;** Multifunctional Yolk-Shell Mesoporous Silica Obtained via Selectively Etching the Shell: A Therapeutic Nanoplatfrom for Cancer Therapy: *ACS Appl. Mater. Interfaces*, 2018. **10**: p. 24440.
72. **X Fang, C Chen, Z Liu, P Liu, N Zheng;** A cationic surfactant assisted selective etching strategy to hollow mesoporous silica spheres: *Nanoscale*, 2011. **3**: p. 1632.

73. **J Tao, M.Dang, Q Hao, X Su, J Zhang;** Facile synthesis of yolk–shell structured monodisperse mesoporous organosilica nanoparticles by a mild alkaline etching approach: *J. Colloid. Inter. Sci*, 2018. **527**: p. 33.
74. **M Gautam, R.K.T., Bijay K P, Hima B R,** Aerosol technique based carbon-encapsulated HMSNs for synergistic chemo-photothermal therapy. *Act. Biomater*, 2019. **In Press**.
75. **Grün M, I Lauer, Unger K.K;** The synthesis of micrometer-and submicrometer-size spheres of ordered mesoporous oxide MCM-41: *Adv. Mater*, 1997. **9**: p. 254.
76. **C Gao, H.Qiu, W Zeng, Y Sakamoto, O Terasak;** Formation mechanism of anionic surfactant-templated mesoporous silica: *Chem. Mater*, 2006. **18**: p. 3904.
77. **Blin JL, M Imperor-Clerc;** Mechanism of self-assembly in the synthesis of silica mesoporous materials: in situ studies by X-ray and neutron scattering: *Chem. Soc. Rev*, 2013. **42**: p. 4071.
78. **Attard G.S, JC Glyde, CG Göltner;** Liquid-crystalline phases as templates for the synthesis of mesoporous silica: *Nature*, 1995. **378**: p. 366.
79. **KJ Edler;** Current understanding of formation mechanisms in surfactant-templated materials: *Aust. J. Chem*, 2005. **58**: p. 627.
80. **Hollamby MJ, D Borisova, Brown P, Eastoe J;** Growth of mesoporous silica nanoparticles monitored by time-resolved small-angle neutron scattering: *Langmuir*, 2012. **28**: p. 4425.
81. **Zhi Yi, LF Dumeé, CJ Garvey, C Feng, F She;** A new insight into growth mechanism and kinetics of mesoporous silica nanoparticles by in situ small angle X-ray scattering: *Langmuir*, 2015. **31**: p. 8478.
82. **JC Vartuli, KD Schmitt, CT Kresge, WJ Roth;** Development of a formation mechanism for M41S materials: *Stud. Surf. Sci. Catal*, 1994. **84**: p. 53.
83. **LP Singh, SK Bhattacheryya, G Mishra;** Functional role of cationic surfactant to control the nano size of silica powder: *Applied nanoscience*, 2011. **1**: p. 117.
84. **Yang B, Chen Y, Shi J;** Exogenous/Endogenous-Triggered Mesoporous silica cancer nanomedicine: *Adv. Health. Mater*, 2018. **7**: p. 1800268.
85. **VN Bharadwaj, DT Nguyen, VD Kodibagkar, SE Stabenfeldt;** Nanoparticle-based therapeutics for brain injury: *Adv. Health. Mater*, 2018. **7**: p. 1700668.
86. **L Ernawati, R Balgis, T Ogi, K Okuyama;** Tunable synthesis of mesoporous silica particles with unique radially oriented pore structures from tetramethyl orthosilicate via oil–water emulsion process: *Langmuir* 2017. **33**: p. 783.

87. **Zainal N A, RK Singh, Shukor A, Azwana H, Wab A, Razak KA;** Study on the effect of synthesis parameters of silica nanoparticles entrapped with rifampicin: *Chem. Eng. Trans*, 2013, **32** p. 2245.
88. **Christian C-G, Ana Laura P-U, Perla Elvia G-C;** Synthesis of Controlled-Size Silica Nanoparticles from Sodium Metasilicate and the Effect of the Addition of PEG in the Size Distribution: *Materials (Basel)*, 2018 **11**: p. 510.
89. **N Rameli, K Jumbri, RA Wahab;** Synthesis and characterization of mesoporous silica nanoparticles using ionic liquids as a template: *J. Phy: Conf. Series* 2018. **1123**: p. 012068.
90. **Asmaa M, Khachani M, Adnane El H;** The synthesis and characterization of low-cost mesoporous silica SiO₂ from local pumice rock: *Nanomater and Nanotech*, 2015. **5**: p. 35.
91. **AA Pisal, AV Rao;** Comparative studies on the physical properties of TEOS, TMOS and Na₂SiO₃ based silica aerogels by ambient pressure drying method: *J. Porous Mater*, 2016. **23**: p. 1547.
92. **F Lu, SH Wu, Y Hung, CY Mou;** Size effect on cell uptake in well-suspended, uniform mesoporous silica nanoparticles: *Small*, 2009. **5**: p. 1408.
93. **He Q, Z Zhang, Yu Gao, Shi J, Y Li;** Intracellular localization and cytotoxicity of spherical mesoporous silica nano- and microparticles: *Small*, 2009. **5**: p. 2722.
94. **Xun Lv, L Zhang, F Xing, H Lin;** Controlled synthesis of monodispersed mesoporous silica nanoparticles: Particle size tuning and formation mechanism investigation: *Micro. Meso. Mater*, 2016. **225**: p. 238.
95. **K Moller, J Kobler, T Bein;** Colloidal suspensions of nanometer-sized mesoporous silica: *Adv. Func. Mater*, 2007. **17**: p. 605.
96. **Ma Kai, W-Z Ulrike, J Zwanziger J, Wiesner U;** Controlling Growth of Ultrasmall Sub-10 nm Fluorescent Mesoporous Silica Nanoparticles: *Chem. Mater*. 2013, **25**, 677–691, 2013. **25**: p. 677.
97. **Ya-Dong Chiang, H-Y Lian, S-Y Leo, S-G Wang, Kevin C;** Controlling particle size and structural properties of mesoporous silica nanoparticles using the Taguchi method: *J. Phy. Chem: C*, 2011. **115**: p. 13158.
98. **M Bouchoucha, MF Cote, RC Gaudreault;** Size-controlled functionalized mesoporous silica nanoparticles for tunable drug release and enhanced anti-tumoral activity: *Chem. Mater*, 2016 **28**: p. 4243.
99. **J Gu, K Huang, X Zhu, Y Lia, J Wei, W Zhao, C Liu;** Sub-150 nm mesoporous silica nanoparticles with tunable pore sizes and well-ordered mesostructure for protein encapsulation: *J. Colloid. Inter. Sci*, 2013. **407**: p. 236.

100. **Asefa T, Z Tao;** Biocompatibility of mesoporous silica nanoparticles: *Chem. Res. Toxicol.*, 2012. **25**: p. 2265.
101. **R Ricco, E Penna, S Nizzero, A Meneghello;** Ultra-small dye-doped silica nanoparticles via modified sol-gel technique: *J. Nanopart. Res.*, 2018. **20**: p. 117.
102. **A Van Blaaderen, A Vrij;** Synthesis and characterization of colloidal dispersions of fluorescent, monodisperse silica spheres: *Langmuir*, 1992. **8**: p. 2921.
103. **L. Novotny, NV Hulst;** Antennas for light: *Nat. Photonics*, 2011. **5**: p. 83.
104. **Dragan AI, Bishop ES, JR Casas-Finet, Robert JS, McGivney J, Schenerman MA, Geddes CD;** Distance dependence of metal-enhanced fluorescence: *Plasmonics*, 2012. **7**: p. 739.
105. **Luigi Tarpani, L Latterini;** Plasmonic effects of gold colloids on the fluorescence behavior of dye-doped SiO₂ nanoparticles: *J. Luminescence*, 2017. **185**: p. 192.
106. **Cai K, Dai L, Zhang Q, Li J, Shen X;** Dendrimerlike mesoporous silica nanoparticles as pH-responsive nanocontainers for targeted drug delivery and bioimaging: *ACS Appl. Mater. Interfaces*, 2015. **7**: p. 7357.
107. **Sudimack J, RJ Lee;** Targeted drug delivery via the folate receptor: *J Adv. Drug Del. Rev.*, 2000. **41**: p. 147.
108. **AZ Wang, OC Farokhzad;** Current progress of aptamer-based molecular imaging: *J. Nucl. Med.*, 2014. **55**: p. 353.
109. **Hunho Jo, J Her, Changill Ban;** Dual aptamer-functionalized silica nanoparticles for the highly sensitive detection of breast cancer: *Bio sensor. Bio electron.*, 2015. **71**: p. 129.
110. **S C March, I Parikh, P Cuatrecasas;** A simplified method for cyanogen bromide activation of agarose for affinity chromatography: *Anal. Biochem.*, 1974. **60**: p. 149.
111. **DB Tada, LLR Vono, EL Duarte, R Itri, MS Baptista;** Methylene blue-containing silica-coated magnetic particles: a potential magnetic carrier for photodynamic therapy: *Langmuir*, 2007. **23**: p. 8194.
112. **TY Ohulchansky, I Roy, LN Goswami, Y Chen, RK Pandey;** Organically modified silica nanoparticles with covalently incorporated photosensitizer for photodynamic therapy of cancer: *Nano. Lett.*, 2007. **7**: p. 2835.
113. **SJ Lee, K Park, YK Oh, SH Kwon, S Her, IS Kim;** Tumor specificity and therapeutic efficacy of photosensitizer-encapsulated glycol chitosan-based nanoparticles in tumor-bearing mice: *Biomater.*, 2009. **30**: p. 2929.

114. **Y H Chen, A Gryshuk, S Achilefu, T Ohulchansky, W Potter, T X Zhong;** A novel approach to a bifunctional photosensitizer for tumor imaging and phototherapy: *Bioconju. Chem*, 2005. **16**: p. 1264.
115. **K Wang, X.H., X Wu, B Shi, L Hai;** Methylene blue-encapsulated phosphonate-terminated silica nanoparticles for simultaneous in vivo imaging and photodynamic therapy: *Biomater*, 2009. **30**: p. 5601.
116. **C Li, W Wang, L Yang, H Sun, Z Yang, Q Du;** Enhanced photodynamic efficiency of methylene blue with controlled aggregation state in silica-methylene blue-acetate@ tannic acid-iron (III) ions complexes: *Dyes. Pigments*, 2019. **160**: p. 663.
117. **He X, Wu X, Wang K, Shi B, Hai L;** Methylene blue-encapsulated phosphonate-terminated silica nanoparticles for simultaneous in vivo imaging and photodynamic therapy: *Biomater*, 2009. **30**: p. 5601.
118. **Penadés S, JM de la Fuente, Fernández A, Africa GB;** Gold glyconanoparticles as water-soluble polyvalent models to study carbohydrate interactions: *Angew Chem. Int Ed.*, 2001. **40**: p. 2257.
119. **JP Kamerling, KM Halkes, AC de Souza, C Elizabeth, GJ Gerwig;** A facile method for the preparation of gold glyconanoparticles from free oligosaccharides and their applicability in carbohydrate-protein interaction studies: *Eur. J. Org. Chem*, 2005, **2005**: p. 3650.
120. **David A. Russell, P.G. Calavia, Isabelle C, Michael J Cook, Alan H Haines;** Targeted photodynamic therapy of breast cancer cells using lactose-phthalocyanine functionalized gold nanoparticles: *J. Colloid. Inter. Sci*, 2018. **512**: p. 249.
121. **Dmitry Yu. Murzin, LS Correia, Henrik G, Johan W, Tapio S;** Catalytic oxidation kinetics of arabinose on supported gold nanoparticles: *Chem. Eng. Jour*, 2019. **370**: p. 952.
122. **Fengrui Song, G.Cheng, J Xing, Z Pi, Shu Liu;** α -Glucosidase immobilization on functionalized Fe₃O₄ magnetic nanoparticles for screening of enzyme inhibitors: *Chinese Chemical Letters*, 2019. **30**: p. 656.
123. **A Fontes, CRA Cunha., ADPR Oliveira, TVC Firmino;** Biomedical applications of glyconanoparticles based on quantum dots: *Biochim. Biophys Acta (BBA) - General Subjects*, 2018. **1862**: p. 427.
124. **Brevet D, Gary-Bobo M, Raehm L, Richeter S;** Mannose-targeted mesoporous silica nanoparticles for photodynamic therapy: *Chem Commun (Camb)*, 2009. **12**: p. 1475.

125. **Fang IJ, II Slowing, Wu KCW, Lin VS, Trewyn BG;** Ligand Conformation Dictates Membrane and Endosomal Trafficking of Arginine-Glycine-Aspartate (RGD)-Functionalized Mesoporous Silica Nanoparticles: *Chemistry*, 2012. **18:** p. 7787.
126. **Ma M, H Chen, Chen Y, Zhang K, Wang X;** Hyaluronic acid-conjugated mesoporous silica nanoparticles: excellent colloidal dispersity in physiological fluids and targeting efficacy: *J Mater Chem*, 2012. **22:** p. 5615.
127. **Luo Z, C.K., Hu Y, Zhao L, Liu P, Duan L;** Mesoporous silica nanoparticles end-capped with collagen: Redox-responsive nanoreservoirs for targeted drug delivery: *Angew Chem Int Ed*, 2011. **50:** p. 640.
128. **Chuanbin Wu, B.C;** Lactosaminated mesoporous silica nanoparticles for asialoglycoprotein receptor targeted anticancer drug delivery: *J. of Nanobiotech*, 2015. **13:** p. 7.
129. **Kamhi, J., Dordick J;** Glycosaminoglycans in infectious disease: *J. Biol. Rev. Camb. Philos. Soc* 2013. **88:** p. 928.
130. **Kalana W. Jayawardana, S.A., Mingdi Yan;** Aggregation based detection of *M. smegmatis* using d-arabinose-functionalized fluorescent silica nanoparticles: *Chem. Commun*, 2015. **51:** p. 15964.
131. **Kalana W. Jayawardana, N.K., Yansong Ren;** Trehalose-conjugated photofunctionalized mesoporous silica mesoporous silica nanoparticles for efficient delivery of isoniazid into mycobacteris: *ACS Biomater. Sci. Eng*, 2015. **1:** p. 1250.
132. **Mingdi Yan, K.J., Xin Wang;** Carbohydrate-conjugated fluorescent silica nanoprobe for selective detection of galectin-1 and prostate cancer cells: *Sci Lett J*, 2015. **4:** p. 132.
133. **Veronika Mamaeva, R.N., Michaela Beck;** Inhibiting notch activity in breast cancer stem cells by glucose functionalized nanoparticles carrying γ -secretase inhibitors: *Molecular therapy*, 2016. **24:** p. 926.
134. **Fan Xia, A.H;** Cellulose conjugated FITC labelled mesoporous silica nanoparticles: intracellular accumulation and stimuli responsive doxorubicin release: *Nanoscale*, 2016. **8:** p. 5089.
135. **John E E, J.M.R., Erik N;** Sugar-decorated mesoporous silica nanoparticles as delivery vehicles for the poorly soluble drug celastrol enables targeted induction of apoptosis in cancer cells: *Euro. J. Pharma. Biopharma*, 2015. **96:** p. 11.
136. **Pedram E, A.S.T., Amir H;** Sugar conjugated dendritic mesoporous silica nanoparticles as pH-responsive nanocarriers for tumor targeting and controlled release of deferasirox: *Mater. Sci. Engineer: C*, 2019. **98:** p. 358.

137. **Ravin Narain, Y.K., Y Zhang, M Ahmed, M Ebara;** Fabrication of FITC doped silica nanoparticles and study of their cellular uptake in the presence of lectins: *J. Biomed Mater. Res: A*, 2013. **101A**: p. 2090.
138. **Mingdi Yan, X.W;** Dye-doped silica nanoparticles as efficient labels for glycans: *Chem. Commun*, 2011. **47**: p. 4261.
139. **Amit Basu, J.M.B., Hyun-Joo Park;** Carbohydrate-coated fluorescent silica nanoparticles as probes for the galactose/3-sulfogalactose carbohydrate-carbohydrate interaction using model system and cellular binding studies: *Bioconjugate Chem*, 2012. **23**: p. 1166.
140. **Mingdi Yan, X.W;** Dynamic light scattering as an efficient tool to study glyconanoparticle-lectin interactions: *The Analyst*, 2011. **136**: p. 4174.
141. **Mingdi Yan, H.W., Xin Wang;** Fabrication of glyconanoparticle microarrays: *Anal. Chem*, 2012. **84**: p. 3049.
142. **Wang X, M.E., Deng L, Koharudin L, Gronenborn AM;** Sensing lectin-glycan interactions using lectin super-microarrays and glycans labeled with dye-doped silica nanoparticles: *Biosens Bioelectron*, 2013. **15**: p. 258.
143. **Li Z, B.J.C., Bosoy A;** Mesoporous silica nanoparticles in biomedical applications: *Chem. Soc. Rev*, 2012. **41**: p. 2590.
144. **Kim M Y, K.J;** *ACS Bio-mater. Science & Engineer*, 2017. **3**: p. 572.
145. **Kwon D, C.B.G., Cho Y, Min J, Park E B, Kang S J, Kim.J;** Extra-large pore mesoporous silica nanoparticles for directing in vivo M2 macrophage polarization by delivering IL-4: *Nano Letters*, 2017. **17**: p. 2747.
146. **Tang F, L.L., Chen D;** Mesoporous silica nanoparticles: synthesis, biocompatibility, and drug delivery: *Advance. Mater*, 2012. **24**: p. 1504.
147. **Pölloth, C.F;** The safety of nanostructured synthetic amorphous silica (SAS) as a food additive (E551): *Archives. toxicol*, 2016. **90**: p. 2885.
148. **Jiang He, X.G., Li Deng;** Synthesis and characterization of functionalized rhodamine B-doped silica nanoparticles: *Optical Mater*, 2009. **31**: p. 1715.
149. **Zhao Bing, M.X., Wu ChuanLiu,** *Chinese. Sci. Bull*, 2011. **56**: p. 3242.
150. **K, V;** Synthesis of silica nanosphere from homogeneous and heterogeneous system: *Bull. Mater. Sci*, 2007. **30**: p. 615.
151. **Zhao Y Bing, M.X., LI Chong;** *Chinese Sci Bull*, 2011. **56**: p. 3242.

152. **Hans H G, A.H.c.e;** Electrophoretic characterization and purification of silica coated photon upconverting nanoparticles and their bioconjugates: *ACS Appl. Mater. Interfaces*, 2014. **6**: p. 6930.
153. **Ow, H;** Bright and stable core-shell fluorescent silica nanoparticles: *Nano Lett*, 2005. **5**: p. 113.
154. **T Nedelčev, D.R., I Krupa;** Preparation and characterization of a new derivative of rhodamine B with an alkoxy-silane moiety: *Dyes and Pigments*, 2008. **76**: p. 550.
155. **B C Roy, R.P., S Mallik;** Synthesis and fluorescence properties of new fluorescent, polymerizable, metal-chelating lipids: *J Org Chem*, 2000. **65**: p. 3644.
156. **T. Ohishi;** An ethoxy-silane rhodamine B derivative and its application to surface coatings on display devices: *J Non-cryst Solids*, 2003. **332**: p. 80.
157. **Bruhwiller, D;** Postsynthetic functionalization of mesoporous silica: *Nanoscale*, 2010. **2**: p. 887.
158. **F O M Gaslain, C.D., A Walcarius;** One step preparation of thiol modified mesoporous silica spheres with various functionalization levels and different pore structures: *J. Sol-Gel Sci. Technol*, 2009. **49**: p. 112.
159. **Y Moussaouib, S.K., N Mnasria, E Elalouiac;** Tuning particle morphology of mesoporous silica nanoparticles for adsorption of dyes from aqueous solution: *J. Saudi Chem. Soc*, 2018. **22**: p. 405.
160. *IUPAC. Reporting Physisorption Data for Gas/Solid Systems* Pure Appl. Chem. , 1957. **87**: p. 603
161. **Vazquez N I, B.F., Z Gonzalez;** Synthesis of mesoporous silica nanoparticles by sol-gel as nanocontainer for future drug delivery applications: *Bol. Soc. Esp. Ceram. Vidr*, 2017. **56**: p. 139.
162. **Nandanwar, R., Amer;** *Chem Sci. J*, 2015. **5**: p. 1.
163. **Martin S.E, a.P.B.R;** A colorimetric enzyme-linked on bead assay for identification of synthetic substrates of protein tyrosine kinases: *J. Pept. Sci*, 2002. **8**: p. 227.
164. **Lu, H.-T;** Synthesis and characterization of amino functionalized silica nanoparticles: *Colloid. Journal*, 2013. **75**: p. 311.
165. **Bhattacharyya, S;** Effect of surfactant concentration on the morphology and texture of MCM-41 materials: *J Phy Chem: C*, 2008. **112**: p. 10674.
166. **H-P Lin, C.-Y.M;** Synthesis of mesoporous silica nanoparticles: *Chem. Soc Rev*, 2013. **42**: p. 3862.

167. **K Strebhardt, A.U;** Paul Ehrlich's magic bullet concept: 100 years of progress: *Nat Rev Cancer*, 2008, 8: p. 473.
168. **D Edinger, M.N., R Klaeger;** The effect of molar mass and degree of hydroxyethylation on the controlled shielding and deshielding of hydroxyethyl starch coated polyplexes: *Biomater*, 2013. **34**: p. 2530.
169. **M Noga, D.E;** Controlled shielding and deshielding of gene delivery polyplexes using hydroxyethyl starch (HES) and alpha amylase: *J Control Release*, 2012. **159**: p. 92.
170. **Christopher E, N.R.J., Nandan E;** Synthesis of carbohydrate conjugated nanoparticles and quantum dots: *Langmuir*, 2008. **24**: p. 6215.
171. **Changfen Bi, Y.L., L Chen;** Maltose functionalized hydrophilic magnetic nanoparticles with polymer brushes for highly selective enrichment of N-linked glycopeptides: *ACS Omega*, 2018. **3**: p. 1572.
172. **A G Barrientos, J.M.d.l.F., J Canada;** Modulating glycosidase degradation and lectin recognition of gold glyconanoparticles: *Carbohydrate Res*, 2009. **344**: p. 1474.
173. **Q Tong, X.W., H Wang;** Fabrication of glyconanoparticle microarrays: *Anal Chem*, 2012. **84**: p. 3049.
174. **Hakeem Abdul, Z.F., Duan Ruixue;** Cellulose conjugated FITC-labelled mesoporous silica nanoparticles: intracellular accumulation and stimuli responsive doxorubicin release: *Nanoscale*, 2016. **8**: p. 5089.
175. **Hermanson, G.T.,** *Bioconjugate techniques*. 2013.
176. **Paul Rolf, A.G.W;** N,N'-carbonyldiimidazole, a new peptide forming reagent: *J. Am. Chem. Soc*, 1960. **82**: p. 4596.
177. **M Dubois, K.A.G., J K Hamilton, F Smith;** Colorimetric method for determination of sugars and related substances: *Anal. Chem*, 1956. **28**: p. 350.
178. **M Monsigny, C.P., A C Roche;** Colorimetric determination of neutral sugars by a resorcinol sulfuric acid micromethod: *Anal Biochem*, 1988. **175**: p. 525.
179. **Matthias Karg, Laura.H;** Presenting precision glycomacromolecules on gold nanoparticles for increased lectin binding: *Polymers*, 2017. **9**: p. 716.
180. **M.Elsabahy, K.L.W.;** Design of polymeric nanoparticles for biomedical delivery applications: *Chem Soc Rev*, 2012. **41**: p. 2545.
181. **L Ding, H.J.;** Biofunctionalization of nanoparticles for cytosensing and cell surface carbohydrate assay: *J Mater Chem*, 2011. **21**: p. 18154.
182. **Vollmer W, B.D;** Peptidoglycan structure and architecture: *FEMS Microbiol Rev*, 2008. **32**: p. 149.

183. **U, V.W.a.B.;** Murein (peptidoglycan) structure, architecture and biosynthesis in *E.Coli*: *Biochim Biophys Acta-Biomembrane*, 2008. **1778**: p. 1714.
184. **Baschnagel-DePamphilis, J;** Relationship between glucose utilization and growth rate in *Bacillus Subtilis*: *J Bacteriology*, 1969. **98**: p. 222.
185. **Chitra, a;** Fluorescent silica nanoparticles in the detection and control of the growth of pathogens: *J Nanotech*, 2013. **2013**: p. 7.
186. **J Song, H.k., J Jang;** Bacterial adhesion inhibition of the quaternary ammonium functionalized silica nanoparticles: *Colloid Surface B*, 2011. **82**: p. 651.